Impact of Chemical and Morphological Changes on the Phase Stability of Magnetic Materials

Submitted by

Connor Skelland

to the University of Exeter
as a thesis for the degree of
Doctor of Philosophy in Engineering
In December 2021

This thesis is available for Library use on the understanding that it is copyright material and that no quotation from the thesis may be published without proper acknowledgement.

I certify that all material in this thesis which is not my own work has been identified and that no material has previously been submitted and approved for the award of a degree by this or any other University.

Signature: CSkelland .....

Acknowledgments

I couldn't have completed this work without the support and guidance of my supervisor Gino Hrkac. He supported me throughout all my research endeavours, helped me to think clearly, clarified any issues, and helped me solve any problem I approached him with. Thank you Gino for everything you've done over the course of my PhD.

I would also like to thank to my second supervisor Rob Hicken for his guidance and input and the opportunity to work alongside him on some interesting projects.

To my parents, thank you for your never ending support, I told you I would finish it one day! To the friends I've made in Exeter, thanks so much for all the great times and may they continue!

Lastly and most importantly to Jessica, who supported me throughout the final write up and made my life so much easier. I love you and I'll never stop being grateful to you for everything you did to help. You're an incredible person.

Abstract

Permanent magnetic materials are of fundamental importance to the modern world, utilised in fields as broad as computers, cars, and MRI machines. Their importance is set to increase as the world move towards sustainable energy and away from fossil fuels. A seamless switch requires an increase in magnet production, and an improvement in performance. Rare-earth reduced permanent magnets are considered a solution to these two problems.

This thesis investigates the impact of chemical and morphological changes on the phase stability of rare-earth reduced hard permanent magnets. New methodologies for investigating the position preference of atomic substitutions and dopants have been applied to the RT_{12} (R = Rare-Earth, T = Transition metal) phase group. This work demonstrates that substitution of the transition metal for titanium in $NdFe_{12}$, $SmFe_{12}$, and $SmCo_{12}$, decreases the cohesive energy, and therefore increases the stability of the structure up to 8Ti at.%. Through analysis of substitution positions it is demonstrated this is tied to a structural effect, derived from a switch in the symmetry of preferential substitution positions.

To gauge the manufacturing feasibility of one of these phases, computational investigations of the melting temperature of $NdFe_{12}$ at various pressures were performed using a Solid Liquid coexistence methodology applied in Molecular Dynamics. Pair potentials used for this work were generated by a genetic algorithm potential fitting methodology, which has application beyond the RT_{12} phase group.

Finally, a new methodology for understanding grain morphology is presented, which takes into consideration the shape, surfaces, and interfaces of cyrstalline grain structures. This methodology is tested on the FePt $L1_0$ structure, which is able to produce stable magnetic grains at nanometer sizes, due to it's magnetic anisotropy of H_a = 6-10 MJ/m^3. This work shows that at grain sizes between 3-9nm, the morphology of the grains is dominated by surface energy, and will result in structures with $\{111\}$ planes as their primary faces. This result has implications for the design of next generation hard drives.

Contents

List of Figures

List of Tables

Declaration

The majority of this work is based on three publications for which I am the first author[1, 2, 3]. The work from these papers covers Chapters 3 and 4 and is my own unless otherwise stated in the text.

The remaining work in Chapter 5 has been submitted to the MMM/Intermag 2022 joint conference as an oral submission and will be used in the future as the basis of a paper for which I will be first author. Unless otherwise stated in the text, this work is my own also.

1 Introduction

1.1 Aims and Motivation

The aim of this work is to investigate the impact of chemical and morphological changes on the phase stability of magnetic materials, beginning with rare-earth reduced permanent magnets and ending with high anisotropy magnets for magnetic hard drives. Molecular Dynamics was used to investigate the impact of chemical changes on RT_{12} systems by calculating each system's cohesive energy as a function of the number of elemental substitutions in the lattice. Morphological changes such as lattice expansion and melting are described using Molecular Dynamics and Genetic Algorithm derived pair potentials. Both these methodologies produced guidelines on how to fabricate rare-earth reduced stable magnetic crystal structures.

The preceding work fed into the development of a grain growth model, which uses calculated surface energies to explain grain morphology as a function of the number of atoms in the crystal phase. The model itself is completely generalised and could be used on any crystal structure, but here is tested on FePt $L1_0$.

This work was motivated by the pressing needs[4] of industry and government that are together driving a rapid shift to a renewable energy economy. A shift that cannot occur without access to high performance permanent magnets. Undertaken with and funded by our industrial partners: Toyota and the MagHEM[5] consortium, this research is focused on permanent magnets with fewer critical elements, lower costs, and improved performance. Solving these three issues is critical, if manufacturers are to avoid costly supply chain bottlenecks and continue producing high performance magnetic materials at the pace demanded by industry.

From a scientific perspective, this work was motivated by a drive to understand materials and their behaviour so completely that it becomes possible to design, test, and setup manufacturing protocols for a brand new material without leaving the confines of a silicon chip. To reach that end, this thesis contains a number of newly developed

general methods for modelling and solving material science problems. The collection of which form the basis of Python package which will be the beginning of a decades long open source project devoted to understanding and modelling solid state materials.

1.2 Introduction Layout

In case the reader requires it, the thesis begins with an overview of the coarse classification of magnetic materials, followed by an in depth classification of permanent magnetic materials, which are of primary interest in this work. This is followed by an abridged history of the development of permanent magnetic materials, which clarifies the reasoning behind investigating chemical and morphological changes. The history focuses primarily on the major advances in chemical and morphological investigation that led to practices such as substitution, and grain boundary engineering, that are considered common today. A final section is included on the development of atomistic simulations, again, highlighting the most important steps in the methodology, which have allowed it to be used so extensively in this work.

1.3 Classification of Magnetic Materials

Every material contains electrons, the fundamental particle which is the primary cause of magnetic behaviour[6], and are therefore magnetic to some degree. Electrons create magnetic fields in two ways: orbital motion around their parent nucleus, and magnetic spin. Orbital motion is analogous to a charge in motion around a circuit, and magnetic spin is an intrinsic property of an electron. The magnetic fields allow electrons to magnetically interact with one another, and it is their interaction which governs the magnetic properties of a material. The resulting differences between the macroscopic magnetic properties of materials is what allows us to characterise them.

There are two measures generally used for characterising magnetic materials: magnetic susceptibility χ, and saturation magnetisation $\boldsymbol{M}_s$. Magnetic susceptibility is the

ratio of a materials magnetisation, $\boldsymbol{M}$, to the external field being applied to it $\boldsymbol{H}$, and is given by $\chi = \boldsymbol{M}/\boldsymbol{H}$. Magnetic susceptibility measures how susceptible a material is to becoming magnetised in the presence of an external field. The saturation magnetisation of a material, $\boldsymbol{M}_s$, is a measure of the maximum magnetic field a material is capable of producing. It is defined as the point at which all the magnetic dipoles of a material are aligned with some applied field $\boldsymbol{H}$, such that further increases in the applied field cannot produce a significant increase in the magnetic moment per unit volume of the structure.

These two values are used because they are independent of the size or shape of the magnetic material being investigated. The result being a horse shoe magnet made of some material *A* will have the same magnetic susceptibility and magnetic saturation as a tiny grain of *A* on the order of a few micrometers. These values will be used to introduce the various types of magnetism and how they are characterised. A final section will discuss the further characterisation of Ferro and Ferrimagnetism, the forms of magnetism most interesting for the development of permanent magnetic materials.

1.3.1 Types of Magnetism

There are five main types of magnetism: Diamagnetism, Paramagnetism, Ferromagnetism, Antiferromagnetism, and Ferrimagnetism. The first three were discovered first, and can be clearly demarcated by susceptibility, the latter two were discovered later as their effects are slightly more subtle and can be confused for one of the first three. A brief explanation of each phenomena along with the method of characterisation is given below. For reference Figure 1 shows the characteristic spin alignment for each type of magnetism.

Diamagnetism

Diamagnetism is the result of all the electrons in a material aligning so that neighbouring electrons have their spins aligned anti-parallel to one another. For an atom, this

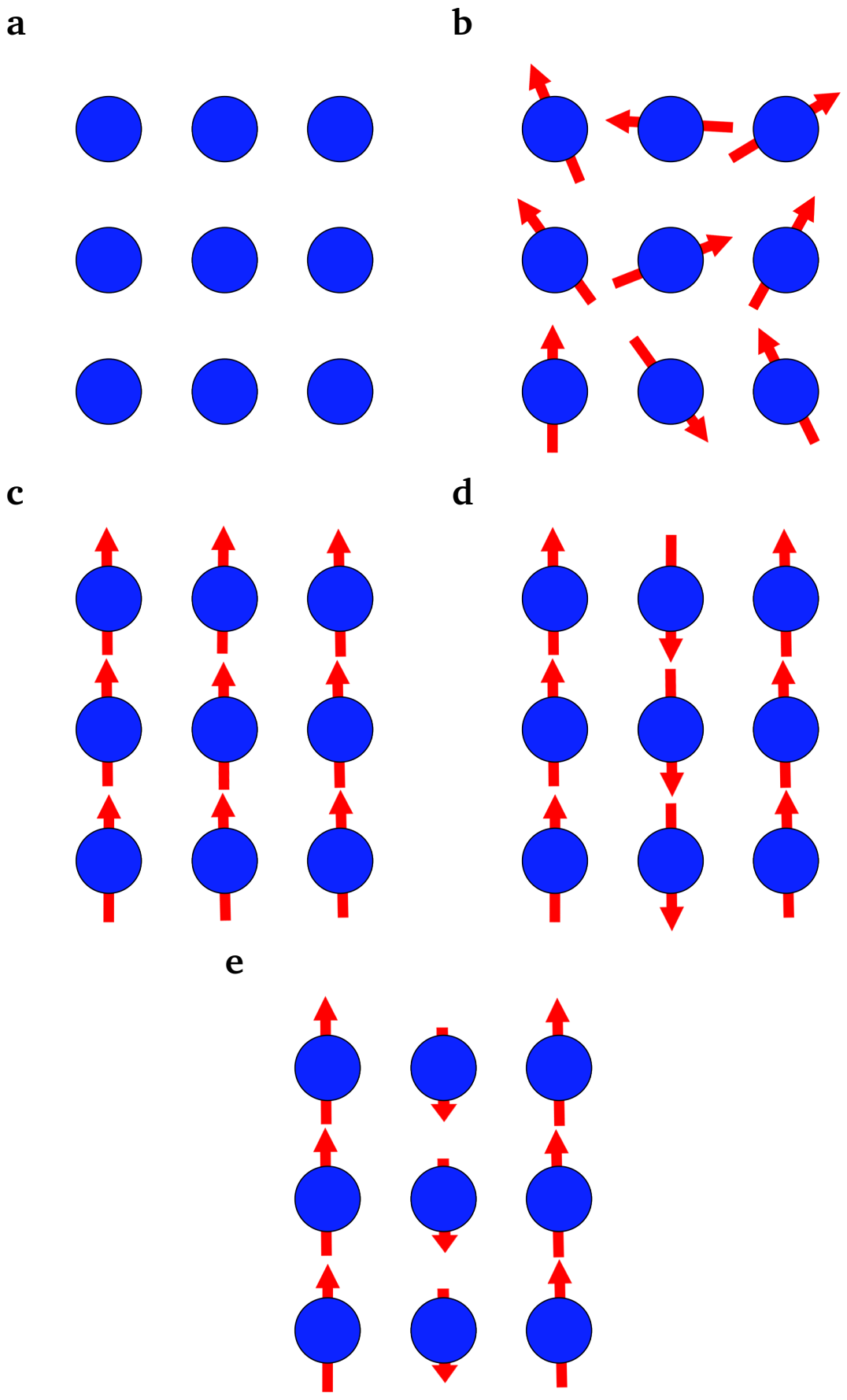

Figure 1: Characteristic atomic spin alignment for a) Diamagnetism, b) Paramagnetism, c) Ferromagnetism, d) Antiferromagnetism, and e) Ferrimagnetism. Where the blue circles represent atoms and the red arrows represent the atom's total magnetic moment.

equates to all the electron orbitals having paired shells, making inert gases like neon and argon diamagnetic. This pairing cancels out the magnetic moment of every electron due to spin and effectively renders the material un-magnetic. The susceptibilities of diamagnetic materials are typically on the order of $\chi \approx -10^{-5}$[7]. The negative sign indicates that diamagnets produce a small magnetic field ,$\boldsymbol{M}$, in the opposite direction to any applied field $\boldsymbol{H}$. All materials have a diamagnetic effect, however in a large number of materials this is masked by dominant effects of paramagnetism or ferromagnetism.

Paramagnetism

Paramagnetism arises from atoms in a material having unpaired electrons in their outer orbitals, resulting in uncancelled spin and orbital magnetic moment contributions. This means that under an applied field $\boldsymbol{H}$ there is tendency for these moments to align along the direction of $\boldsymbol{H}$. In pure paramagnetism the moments in the material are completely isolated from one another, and without any interaction between the electrons the applied field $\boldsymbol{H}$ has a minimal effect on the overall magnetisation of the material. The minimal effect of the field is caused by random thermal fluctuations constantly misaligning magnetic moments, so that at any one time only a fraction of the total moments are aligned in the field direction. In reality most paramagnetic materials do have some interaction between neighbouring magnetic moments, but these are small enough or random enough that they have little effect on the magnetic behaviour of the material. The result of this is that paramagnetic materials generally have susceptibilities of the order $\chi \approx 10^{-5}$ to 10^{-3}[7].

Ferromagnetism

Ferromagnetism similarly to paramagnetism requires unpaired electrons, but unlike paramagnetism has none neglible neighbour interactions which reinforce the effect of the applied field $\boldsymbol{H}$. In ferromagnets it is energetically preferable that spins align in the same direction. Thus re-alignment of any single spin into the direction of the applied magnetic field has a knock on effect on its surrounding spins, quickly causing all the

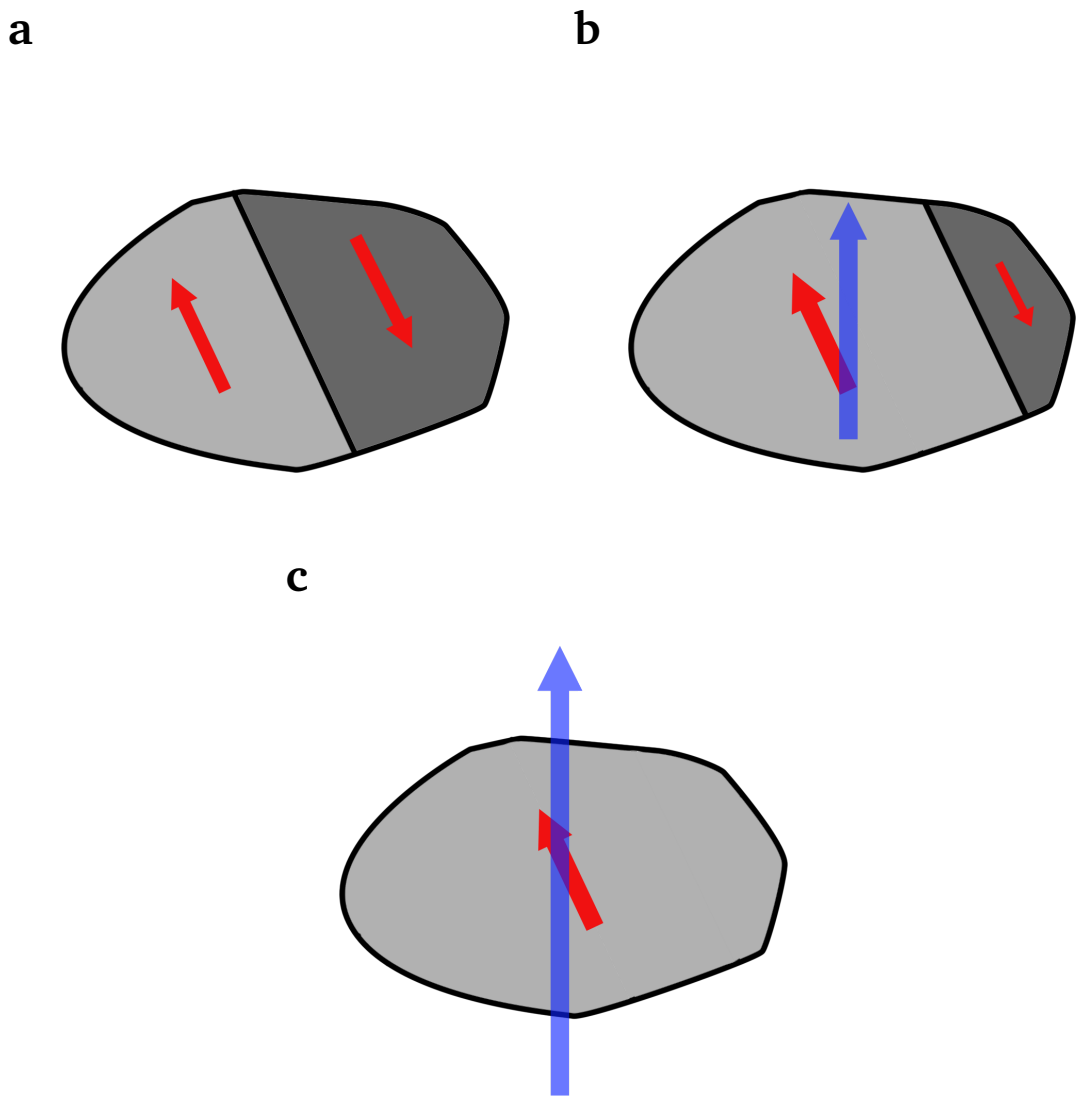

Figure 2: Movement of a domain wall through a grain with applied field, showing the magnetic states of the grain when a) There is no field applied, b) A small field applied (direction shown by blue arrow), and c) A large field applied (direction shown by blue arrow). The different greys in each grain represent separate magnetic domains and the red arrows represent the magnetisation direction of those domains.

spins in the material to magnetically align along the applied field direction to lower their energy. Ferromagnetic materials spontaneously form magnetic domains, separate regions within their volume which have locally aligned magnetic moments. An applied field can quickly magnetise the entire structure by growing the size of domains close to its applied direction, and causing the remaining domains to shrink as their spins join the growing domains[8]. An example of this is shown in Figure 2 This gives ferromagnetic materials a large susceptibility on the order of $\chi \approx 50$ to $10,000$[7].

Antiferromagnetism

Antiferromagnetism is similar to ferromagnetism in that it requires unpaired electrons and none trivial neighbour interactions. The major difference is that for antiferromagnets it is energetically preferable for spins in neighbouring atoms to align anti-parallel to one another[9]. This effectively cancels out the spins and makes antiferromagnets appear none magnetic. In this sense they appear similar to diamagnets, however in reality they can be thought of as two sublattices of ferromagnetic spins perfectly aligned up to magnetic saturation in their opposite directions. Above their Néel temperature they exhibit paramagnetic behaviour, below this temperature they spontaneously order into the alternating antiferromagnetic domains explained above. They have small positive susceptibilities at all temperatures, but the change in their magnetic susceptibility differs above and below this characteristic temperature. In the paramagentic region their susceptibility is small and increases with decreasing temperature. This trend of increasing susceptibility peaks at the Néel temperature and decreases again as the magnetic moments align anti-parallel, analysis of a susceptibility graph is often used to characterise antiferromagnetic materials.

Ferrimagnetism

Ferrimagnetism is similar to both ferromagnetism and antiferromagnetism. Outwardly ferrimagnetic materials appear ferromagnetic, and display the same qualities of spontaneous magnetisation and domain formation, however on an atomic level their spins align antiparallel similarly to those in antiferromagnetic materials[10]. The difference between antiferromagnetic and ferrimagnetic materials is the size of the magnetic moments on the spins of the alternate layers. In antiferromagnetic materials they're exactly the same resulting in a total moment of zero, but in ferrimagnetic materials one spin is larger than the other, resulting in a net magnetic moment in one of the directions. The difference between ferromagnetic and ferrimagnetic materials is noticed by calculating a material's expected saturation magnetisation, based on its constituent elements, and comparing that to experimental results. If the experimental value is significantly

below the theoretical maximum then it's safe to assume some of the moments are not all aligned parallel, and the material is ferrimagnetic not ferromagnetic.

1.3.2 Characterising Ferromagnets and Ferrimagnets

Ferromagnets and Ferrimagnets are the most practically relevant classes of magnetic material, and have received significant research attention. This has led to them being split further into two major categories: magnetically soft, and magnetically hard. The names arose from the large number of experiments performed on iron and carbon steels that occurred in the late 19th and early 20th century, which found a correlation between a material's magnetic properties and its mechanical hardness[11, 12, 13]. Through use, these terms became part of the lexicon of the field, and are used to separate permanent magnetic materials into magnetically soft or hard. To understand the separation between these two it's necessary to understand the development of the idea of magnetic hysteresis. In the later part of the 19th century Alfred Ewing coined the term magnetic hysteresis, giving a name to the phenomena of changes in the magnetic field of a material lagging behind external changes in an applied field. The word hysteresis is derived from Greek and means to "lag behind" or "come second". The hysteresis behaviour of a magnetic material gives rise to several properties which are used to define soft and hard magnetic materials.

Investigations of hysteresis have the following methodology, apply a known magnetic field $\boldsymbol{H}$ to a material and take measurement of the resulting flux density $\boldsymbol{B}$. Repeat these measurements over a range of positive and negative values for the field $\boldsymbol{H}$ and plot the result on a graph. A typical example of such a graph is shown in Figure 3, all such graphs are known as hysteresis loops. Points on the graph are marked to indicate the key values used for characterisation. Magnetic saturation, discussed previously, occurs at the point when further increases in the applied field $\boldsymbol{H}$ have a negligible effect on the measured flux density $\boldsymbol{B}$. The remaining constants are the magnetic remenance M_r, the maximum Energy Product BH_{max}, and the coercivity H_c. Magnetic remenance is the magnetisation $\boldsymbol{M}$ of a material that remains when the applied field $\boldsymbol{H}$ is removed, the

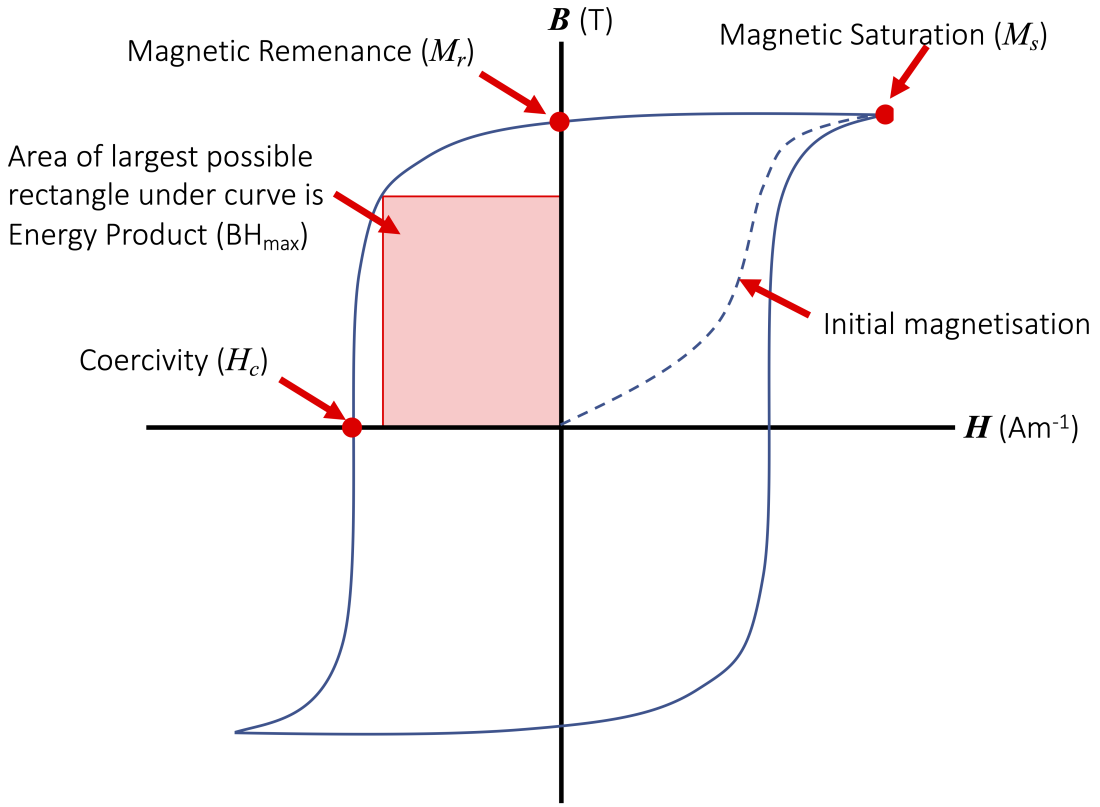

Figure 3: Hysteresis Loop with all the parts of interest indicated on the figure. The y axis is Flux Density ($\boldsymbol{B}$), and the x axis is applied magnetic field strength ($\boldsymbol{H}$)

graph shows that it is the point on the hysteresis curve that passes through the y-axis. Coercivity is the magnitude of applied field $\boldsymbol{H}$ that is required to take a magnetised material to a magnetisation of zero, as the graph shows this is the point at which the hysteresis curve passes through the x-axis. The maximum Energy Product is a measure of the maximum amount of magnetic energy that can be stored in a unit volume of the material of interest, and is represented by the area of the largest rectangle that can be drawn within the hysteresis line in the second quadrant.

Magnetically soft and magnetically hard materials can be split by their coercivities: soft magnetic materials have coercivities $< 1\text{kAm}^{-1}$, and hard magnetic materials have coercivities $> 10\text{kAm}^{-1}$[14]. Therefore, larger magnetic fields are required to demagnetise hard magnetic materials. A further property that is worth considering is magnetic permeability μ, a similar term to the susceptibility χ, which measures the magnetisation a material obtains in response to a field $\boldsymbol{H}$. Below is a brief overview of how these five terms are used to judge the performance of soft and hard magnetic materials.

Soft Magnetic Materials

Soft magnetic materials have applications in DC and AC circuits, in which they are used to enhance the magnetic field $\boldsymbol{H}$ generated by an electric current. Hence, in both scenarios, having a high permeability μ is a desirable property[15]. DC applications cover shielding and electromagnets both of which require high permeability over all properties, and in the case of electromagnets a high magnetic saturation. AC applications cover electric transformers, generators and motors[16], for which a high flux density and a low core loss are essential for keeping weight down and energy losses low. Materials of this kind are often selected not just for their permeability, but also for their low coercivity, with the ideal material having a coercivity of zero. Although these are not the primary interest of this thesis, it is likely the techniques developed in this work will be applied to them in the future.

Hard Magnetic Materials

Hard magnetic materials are typically known as permanent magnets, and have applications in electric motors, speaker systems, and data storage. As their name implies they generate a permanent magnetic field, which makes them indispensable for small scale electromechanical devices that require a magnetic field but are too small to practically produce one with electric current.

For electric motors and other forms of power/ motion related applications the most important property is their maximum Energy Product, the total amount of magnetic energy they're capable of storing per unit volume. A high BH_{max} translates into a high level of power transfer. For other applications, such as data storage, a finer balance must be struck between a high coercivity for data stability and integrity and the capability of hard drive write head to reliably flip bits from one to zero using a finite field $\boldsymbol{H}$.

For both of these applications a further parameter: the curie temperature T_c must be taken into consideration. The Curie temperature is similar to the Néel temperature, and is the point above which a ferromagnetic or ferrimagnetic material becomes paramagentic

due to the disorder induced by random thermal fluctuations. Materials with a high curie temperature and BH_{max} are sort after in high energy applications, such as electric motors, where the production of heat is unavoidable and degradation of magnetic properties due to an increase in temperature must be minimised to save performance.

The final property to consider is closely tied to coercivity and is known as magnetic anisotropy, or the preference for the magnetic moment of a material to lie in one direction over another. A high magnetic anisotropy is not just associated with a high coercivity, it is also associated with what's known as the squareness of the hysteresis loop. In an ideal hard permanent magnet the loop would be completely rectangular, indicating that in order to flip the magnetisation direction of the material, it's necessary to overcome all its stabilising magnetic energy in one step. This never happens as there are other modes of magnetic reversal, such as domain wall movement, which require significantly less energy, however the higher the anisotropy of the material, the closer it gets to this ideal scenario.

1.4 Development of Permanent Magnets

The development of permanent magnets is one of the most significant endeavours in science. The effect this single field has had on the development of humanity is incalculable, and it's not an exaggeration to say that without the permanent magnetic materials we have today, the world as we know it would not exist. From computers, to electrical motors, to MRI machines, the applicability of these materials is only growing with time.

In the current day, there is an extremely wide array of capabilities for investigating magnetic materials and a number of tried and tested techniques for improving magnetic properties. However, this wasn't always the case, and to build motivation for the morphological and chemical investigations undertaken for this thesis the key developments in permanent magnetic materials, which led to the current set of methodologies, will be highlighted below. The development is split into two sections, pre-rare-earth magnets, and rare-earth magnets, the latter of which are of chief interest to this thesis.

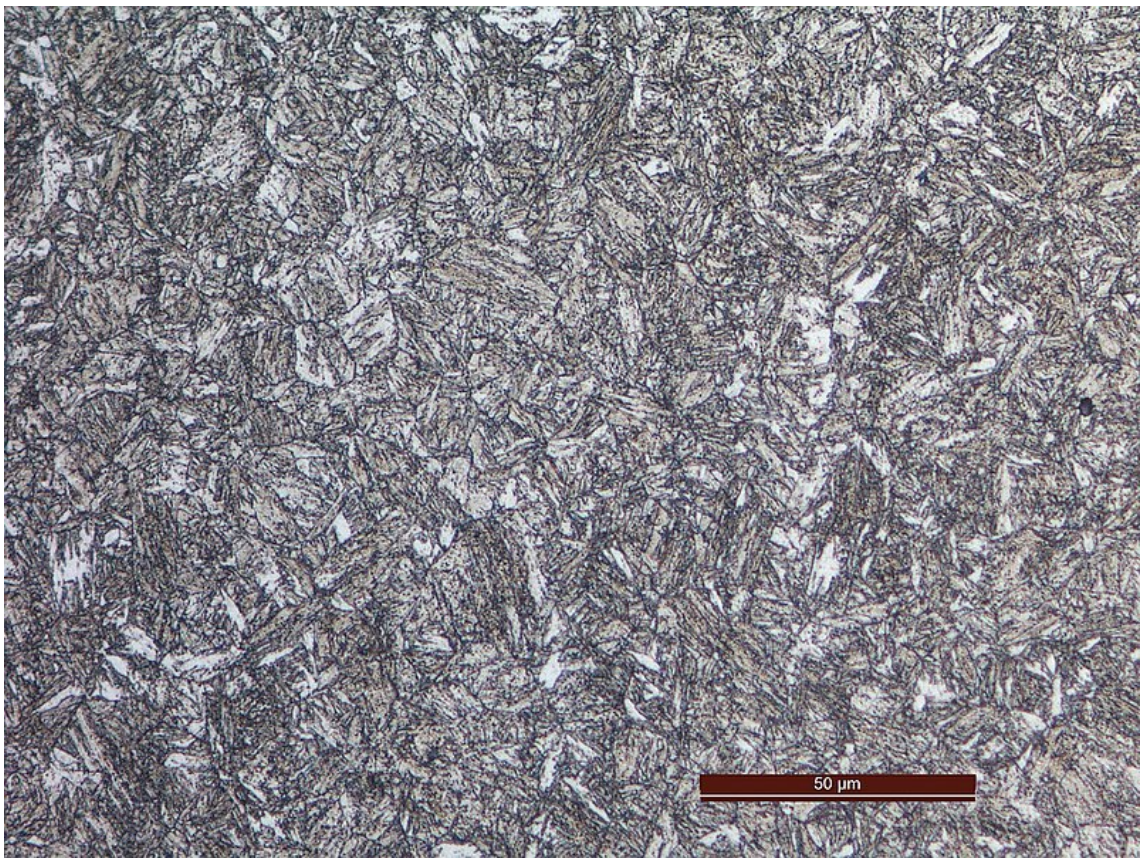

Figure 4: Microscope image of Martensite showing the thin crystals within pre-existing austenite grain boundaries. Credit: Melancholia-itwiki, under license https://creativecommons.org/licenses/by-sa/4.0/deed.en

1.4.1 Pre Rare-Earth

Carbon Steels

In the pre-modern era there were only two types of permanent magnet: lodestone and carbon steels, both of which had a single practical use in compasses. Lodestones are natural Magnetite, found in the region of Magnesia in Greece, and whilst they sparked the initial curiosity in magnetism, they were not deliberately manufactured so will not be treated here.

Carbon steels were the first magnets to be mass produced by smelting iron with small amounts of carbon to produce a mechanically hard steel. The magnetic properties of these steels are derived from their martenistic microstructure[17] which can be seen in Figure 4. Martensite is formed via heating and quenching austenite which causes the nucleation of many thin martensite crystals via a diffusionless shear transformation[18].

Because the transformation is diffusionless the martensite crystals inherit the carbon atom positions from the austenite, along with the granular boundaries of the original structure. As Figure 4 shows, the result is a highly heterogeneous microstructure, with a non-uniform distribution of grain shape, size, and orientation accompanied by a non-uniform distribution of interstitial carbon atoms. This combination gives rise to many domain wall pinning sites which impede domain wall movement, the main mode of magnetic reversal. This gives them a coercivity of $H_c = 4kAm^{-1}$ resulting in a $BH_{max} = 2kJm^{-3}$. The addition of carbon to iron is the world's first example of a manufacturing technique which controls magnetic properties by changing a material's microstructure through the addition of an interstitial element. However, as the addition of carbon in the pre-modern era was primarily focused on improving the mechanical properties of iron, its magnetic significance went unnoticed.

Tungsten and KS Steels

Carbon steels were improved empirically over time, first with the introduction of Tungsten steels in the mid 19th century, which improved the properties of carbon steels via the addition of 5-6% tungsten. The addition increases the heterogeneity of the structure by preventing some of the base austenite grains from following the martensite formation process. The added heterogeneity increases the coercivity of the microstructure to about $H_c = 5.2kA/m$[19] (converted to SI), which leads to a BH_{max} of $2.4kJm^{-3}$, a modest but significant increase of 20%. Tungsten steels represent a highly significant step forward in the development of permanent magnets, as they were the first material which had their magnetic properties controlled by microstructural changes induced by a tertiary element, highlighting the unnoticed effect carbon had previously.

This step forward led to various groups around the world attempting further elemental additions, leading to the discovery of KS steel by Honda and Saito in 1920[20]. They showed that alloying together: carbon 0.4-0.8%, cobalt 30-40%, tungsten 5-9%, and chromium 1.5-3%, with an iron base, produced a steel with a coercivity of $H_c = 10 - 20kA/m$[21]. This was three times that which had been achieved from the very best

Tungsten steels, giving a $BH_{max} = 8kJm^{-3}$. This is attributed to the addition of cobalt, which allowed for greater differences in the localised magnetic saturation, increasing magnetic heterogeneity. Making KS steel the first magnetic material to control magnetic properties by the addition of an element for its intrinsic properties alone. A technique carried forward into modern day rare-earth magnets.

Alnico

Two further steels followed on from this MK Steel in 1930, and NKS Steel in 1934 with $BH_{max} = 9.6kJm^{-3}$ and $16kJm^{-3}$ respectively[22]. Both of these magnets are alloys containing mainly Fe, Al, Ni, Co, Cu, and Ti[23].

The manufacturing process required these materials to be heated to 1520K at which point a homogenous BCC lattice of the constituent elements would form. Cooling this phase down at a rate of 30K/s and then tempering at 920K, results in what's known as a spinodal decomposition, a spontaneous separation of a previously homogenous material into two separate phases. For a general example of the end result of this process please see Figure 5, which is a diagram of a previously homogenous phase separated into different phases given by the blue and red parts of the image. Work by Bradley et al.[24] showed that this decomposition results in two phases a magnetic Fe-Co rich, and an unmagnetic Ni-Al rich phase, with both phases forming grain elongated in one of the $\langle 100 \rangle$ directions. The resulting structure in Alnico alloys is magnetic Fe-Co grains embedded in an unmagnetic Ni-Al matrix.

This structure increases coercivity by impeding domain wall movement through the separation of magnetic grains with regions of unmagnetic, or less magnetic material. Significantly, it was the first example of controlling the separation of the magnetic grains to improve a materials magnetic properties. A combination of shape anisotropy, and the magnetic heterogeneity described above gave MK steel a coercive field of $H_c \approx 40kA/m$, and NKS steel $H_c \approx 70kA/m$[25].

MK steels were developed into the Alnico series of permanent magnets[25], which

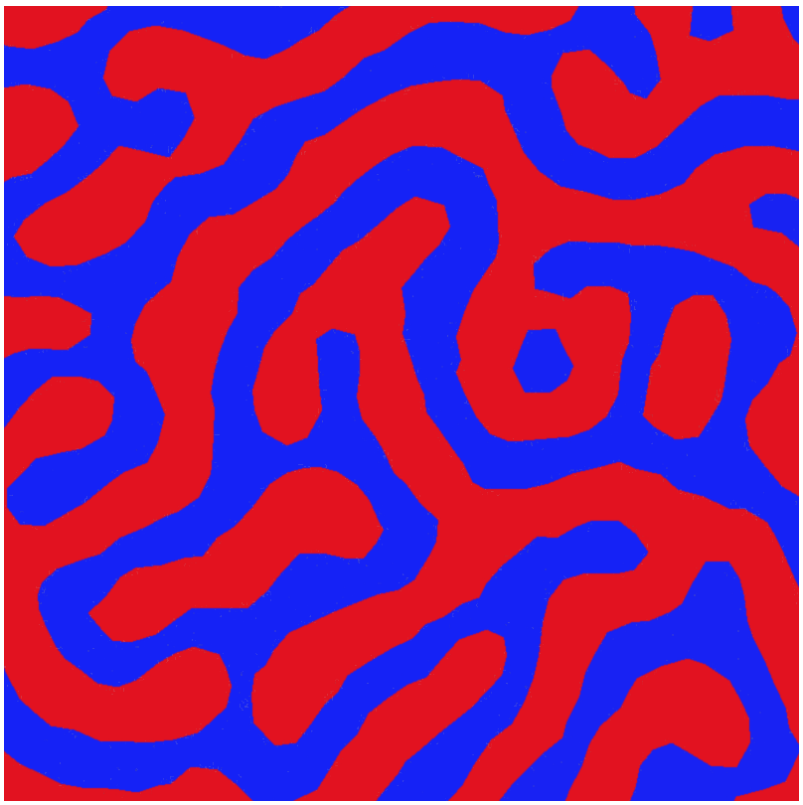

Figure 5: Diagram of a material which has gone through spinodal decomposition. Red and blue represent the two distinct phases. (Note: this does not represent Alnico)

were the first series of magnetic materials to be separated into the groups: isotropic, and anisotropic. Isotropic magnets have no preferred magnetic orientation. In the case of Alnico the best magnetic properties achieved by this kind of magnet were found in Alnico 2, with $H_c = 60 - 70kA/m$, and BH_{max} = 14-16kJm^{-3}[26].

In contrast, anisotropic magnets do have a preferred magnetic orientation. The distinction was first reported in work by Oliver and Shedden in 1938[27], which showed that the application of a magnetic field during the initial cooling phase of Alnico significantly improved the magnetic properties. It was later found that a field applied along one of the $\langle 100 \rangle$ directions caused preferential grain growth and increased grain elongation in the direction of the field. The resulting grains are columnar, and on average 30nm in diameter and 600nm long[28], giving them a very significant shape anisotropy and a low enough volume to be considered single domain. The result of these microstructural improvements, plus the forced alignment of each grain's magnetic moment during cooling, led to Alnico 5 which has a H_c = 46-52kAm^{-1} and BH_{max} = 40-44kJm^{-3}[29].

This method was extended into the directed grain method, a pre-manufacturing step that aligned grains in the as cast alloy using a magnetic field, so that the alloy's grains shared an axis[30]. Magnetising the material along this shared axis produced a strong anisotropic magnet Alnico 8DG (Directed Grain), with the properties H_c = 110-140kAm^{-1} and BH_{max} = 60-75kJm^{-3}.

The application of a magnetic field during cooling and pre-manufacturing was a significant step forward in the field's development as it demonstrated clearly the importance of grain morphology and crystal structure. In the first case demonstrating the importance grain shape and size could have on overall magnetic properties, and in the second case demonstrating crystal alignment produced aligned and therefore increased magnetic fields.

Ferrites

Ferrites began to recieve major research attention in the 1950s when it was found their cost per unit of magnetic energy stored was an improvement on Alnico[31]. Significantly, these were the first magnetic materials to have their properties controlled by deliberate substitutions for atoms in their crystal.

Ferrites form in the spinel and inverse spinel crystal structures, shown in Figure 6, both of which have anti parallel magnetic sublattices holding atoms of different oxidation states giving them ferrimagnetic properties. The sublattice positions can be separated by their local coordinations. One sublattice has tetrahedral symmetry, whilst the other has octahedral symmetry. For an example of how this works, take the ferrite Fe_3O_4, for which all the tetrahedral positions are occupied by $Fe^{(III)}$ atoms which form one of the ferromagnetic sublattices, the remaining octahedral positions are filled by half $Fe^{(III)}$ atoms and half $Fe^{(II)}$ atoms, which form the second sublattice[32]. There are 8 atoms total in the tetrahedral sites, and 16 total in the octahedral[33]. The resulting mis-balance in magnetic moment results in ferrimagnetic behaviour.

Substitution of some of the iron atoms with an element M = Mn, Fe, Co, Ni, Cu,

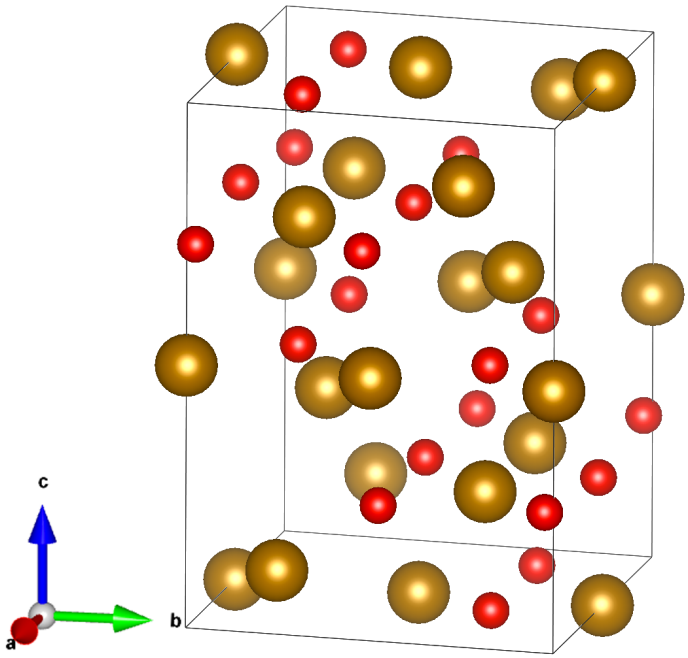

Figure 6: Spinel crystal structure of Fe_3O_4, with iron atoms in gold/yellow, and oxygen atoms in red. The arrows in the picture indicate the crystal's lattice directions a, b, and c.

Zn, Mg, or Cd, allowed researchers to control the total magnetic moment on each of the sublattices. By studying the site preference of the elements in the crystal structure it became possible to tailor material properties on the level of the crystalline unit cell and predict from first principles the expected magnetic behaviour. The site preference of various substiutional elements or interstitial dopants has only increased in significance, as will be shown throughout this thesis.

1.4.2 Rare-Earth Magnets

Samarium Cobalt based magnets

The first indication of the impressive magnetic properties of Rare-Earth alloys was a short publication by Droina and Janus in 1935[34], in which they reported a neodymium-iron alloy with 7% iron had a coercivity $H_c = 340$ kAm^{-3}, and remanence ratio $J_r/J_s = 0.7$. Although interesting from a scientific standpoint, at the time the difficulty extracting singular rare-earth metals meant it wasn't until the 1960's that research into this range of materials continued. The interest restarted with a paper by Hubbard et al. on the

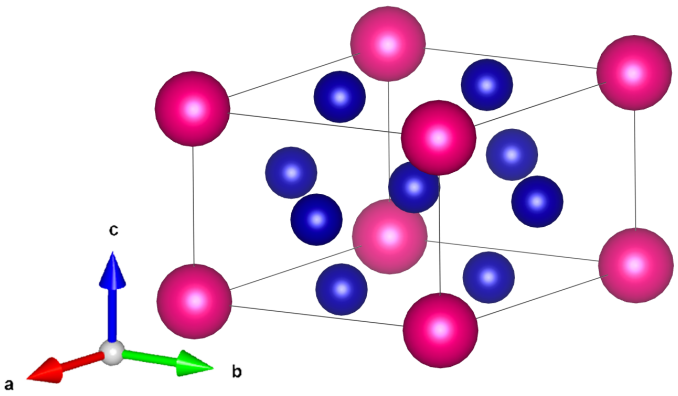

Figure 7: Crystal structure of $SmCo_5$, with samarium atoms in blue, and cobalt atoms in pink. The arrows in the picture indicate the crystal's lattice directions a, b, and c.

properties of gadolinium and various transition metals[35]. This was expanded upon by Strnat et al. in a 1967[36] publication which investigated a range of RCo_5 (R= Y, Ce, Pr, Sm, Y rich and Ce-rich mischmetals). This work revealed the hexagonal structure of the crystal, shown in Figure 7, and its magnetic moment's strong preference to align with the c lattice direction. Of the investigated structures $SmCo_5$ was singled out as the most promising, and in 1970 Benz and Martin[37] published a paper that demonstrated that the addition of Co-Sm(60% wt.) grains to $SmCo_5$ grains allowed the combination to be densified by liquid phase sintering without excessive void formation. The resulting magnets had coercivities of $H_c = 1.2MAm^{-3}$, and a maximum energy product of $BH_{max} = 125kJm^{-3}$, over twice the energy product of anything that had come before it.

The impressive magnetic properties of this structure are derived from its strong preference for the c direction, known as uni-axial magnetocrystalline anisotropy. Buschow et al.[38] showed that this anisotropy is provided by the Sm^{3+} ions[38], which derive this preference from interaction with the crystalline electric field. Although microstructure does play a role, the most significant contributing factor is this magnetocrystalline anisotropy, which made $SmCo_5$ the first in a range of structures that derived almost all their anisotropy from crystal structure alone.

It is difficult to produce $SmCo_5$ materials without the crystallisation of related tertiary phases. One of these phases is Sm_2Co_{17}, with the crystal structure Th_2Ni_{17}, investigations into this phase showed that it too possessed impressive magnetic properties, having a saturation induction in the range J_s = 1.2-1.6T, compared to $SmCo_5$'s J_s =

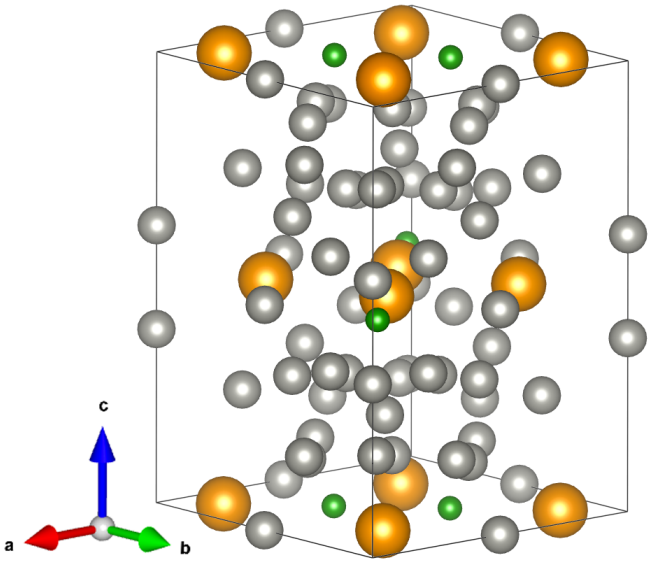

Figure 8: Crystal structure of $Nd_2Fe_{14}B$, with neodymium atoms in yellow, iron atoms in grey, and boron atoms in green. The arrows in the picture indicate the crystal's lattice directions a, b, and c.

0.2-1.2T[39]. The addition of iron to get $Sm_2(Co,Fe)_{17}$ further improved the magnetic properties, with crystal grains demonstrating a high uni-axial crystalline anisotropy along the c direction, derived from the samarium ions as in $SmCo_5$. Manufacturing complications meant a single phase $Sm_2(Co,Fe)_{17}$ magnet wasn't achieved, however copper addition allowed the production of a number of alloys of the form $Sm(Co_{100-x-y}Fe_xCu_y)_7$, which are a combination of the $SmCo_5$ and $SmCo_{17}$ type phases. The best of these $Sm(Co_{74}Fe_{10}Cu_{14})_7$ was made by Senno and Tawara[40] and had a coercivity of $H_c = 490kAm^{-1}$ and a maximum energy product of $BH_{max} = 210kJm^{-3}$.

$Nd_2Fe_{14}B$

Research into $SmCo_{17}$ type phases, opened research avenues into a much wider spectrum of possible rare-earth intermetallic compounds, all of which can be derived from stacking $SmCo_5$ lattices in the c lattice direction[41] (shown in Figure 7). In a bid to lower material costs by using higher abundance elements, researchers began investigating the R-Fe binary alloy phases. This research led to the discovery of $Nd_2Fe_{14}B$ by Sagawa et al. in 1984[42], a ternary compound forming in a tetragonal crystal structure elongated along the c axis, which can be seen in Figure 8. The initial publication[42] reported remarkable magnetic properties of $H_c = 960kAm^{-1}$ and a $BH_{max} = 290kJm^{-3}$, which

were improved in the space of a few years to give a $BH_{max} = 400 kJm^{-3}$[43].

Unlike the simpler $SmCo_5$, the uni-axial anisotropy of $Nd_2Fe_{14}B$ is slightly complicated. Whilst still derived from the anisotropy of R^{3+} ions, two possible subsets for Nd atoms in the lattice 4g and 4f present significantly different crystalline electric fields. The result being that atoms in the 4g subset have a strong preference for uni-axial alignment in the c direction, whereas 4f atoms have a weak preference for alignment in the a,b plane[44]. The strong preference for uni-axial alignment in the 4g atoms is mediated to the 4f atoms by iron, forcing the 4f atoms to align along the c axis also. This magnetic ordering persists at low temperatures, however, at higher temperatures atoms in the 4f position subset start to realign into their preferred in plane positions which plays a role in the demagnetisation of the structure. This lowers the material's curie temperature and is a significant problem for its use in high temperature applications.

The electrical motors in cars and wind turbines are two of the most important applications, generally operating at temperature of 435-455K. As $Nd_2Fe_{14}B$'s base curie temperature is $T_c = 585K$ this operating range puts it at $\sim$75% of the way to losing its permanent magnetism. As can be seen in Figure 9, operating at this temperature results in a significant degradation of the materials magnetic properties, damaging performance.

Currently, the direct chemical solution to this is to substitute 12% of the neodymium in the structure with dysprosium as suggested by Sagawa et al.[43]. Dysprosium atoms have a higher anisotropy than their neodymium counterparts, and are thus less affected by temperature. The problems with this solution are two fold. Firstly, dysprosium prefers antiferromagetic ordering and thus lowers the overall magnetisation of the material. Secondly, dysprosium is significantly more scarce than neodymium and has a prohibitively high material cost, add to that the potential political cost of its supply chain being centred in China and it's not clear this particular solution will be cost effective far into the future.

Although there is currently no direct microstructural solution for raising curie tem-

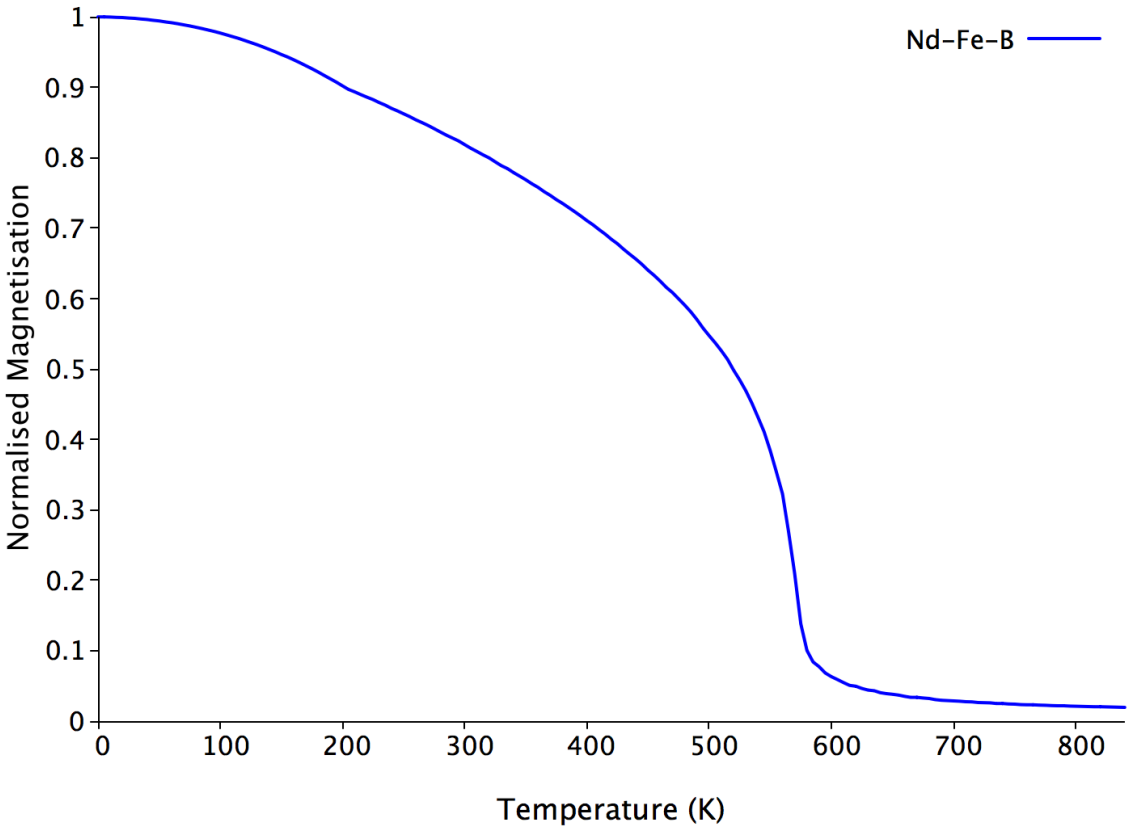

Figure 9: Temperature vs normalised Magnetisation for $Nd_2Fe_{14}B$.

perature, significant efforts have been made to improve the microstructure and hence the magnetic properties of the material. Improved magnetic properties ameliorate the loss of magnetic order by raising the curve seen in Figure 9 and giving it a squarer shape. $Nd_2Fe_{14}B$ is manufactured by milling powder into small particles and hot press sintering the mix to achieve densification. Particular attempts have been made to increase the coercivity by controlling the orientation, size, and intergranular phase of the grains. Work by Bance et al.[45] showed that grain size plays an important role in magnetic domain reversal, with larger sizes increasing the effect of the demagnetising field at the grain's edge, and thus lowering coercivity. A recent patent from Sakuma et al.(US9520230B2) outlines a method for controlling the size as well as the orientation. By coating 100-500nm particles of Nd2Fe14B with a high melting point metal (such as Nb, V, Ti, Cr, Mo, Ta, W, Zr or Hf) grains can be prevented from growing into one another and coarsening. The orientation can be controlled by hot deformation techniques which cause the grains to align along the preferred axis of magnetisation. The result is an anisotropic $Nd_2Fe_{14}B$ magnet.

The first thorough investigation of intergranular phases was undertaken by T. Woodcock et al.[46], who noted two possible phases: a rhombohedral oxide Nd_2O_3 with crystal structure hp5, and an amorphous metallic Nd rich phase. Of the two it was suggested that Nd_2O_3 would cause the greatest lattice distortion, and hence lower coercivity most significantly. In contrast the amorphous Nd phases seemingly reduce the number of defects on the surface, decreasing the number of domain nucleation sites, and keeping the grains magnetically separate.

The development of these ideas relied significantly on both Molecular Dynamics, and Micromagnetics. Marking the beginning of multiscale modelling, which uses a combination of computational simulation and experiment to effectively design and manufacture materials.

RT_{12}

Despite it's impressive properties, the temperature issues of $Nd_2Fe_{14}B$ outlined above, coupled with the push towards a sustainable energy sector based on renewable energy and electric cars, has led to a focus on new magnetic materials with zero or reduced rare-earth elements. Particularly, focusing on low cost, low risk, and high strength magnets. Sadly, there is currently no way to achieve high strength magnets without rare-earth metals. However, just as $Nd_2Fe_{14}B$ replaced the previous phase, $SmCo_5$, it is thought new but related phases could replace $Nd_2Fe_{14}B$.

One of these phases is known as the RT12 phase (R = rare-earth, T = transition metal), whose crystal structure is shown in Figure 10. Previously investigated by De Mooij and Buschow[47], who found the most promising of the ternary structures were the RFe12-xMx phases (M = Si, Ti, V, Cr, Mo or W). Work by Yang et al.[48] found that interstitial nitrogen addition improved these phases even further, particularly $NdFe_{11}TiN$ which has a curie temperature of $T_c \approx 740K$, and a predicted maximum energy product of $BH_{max} \approx 445kJ/m^{-3}$. Despite this, it fell out of favour owing to the intrinsic instability of the binary Nd-Fe phase making it extremely difficult to manufacture through the usual methods of densification.

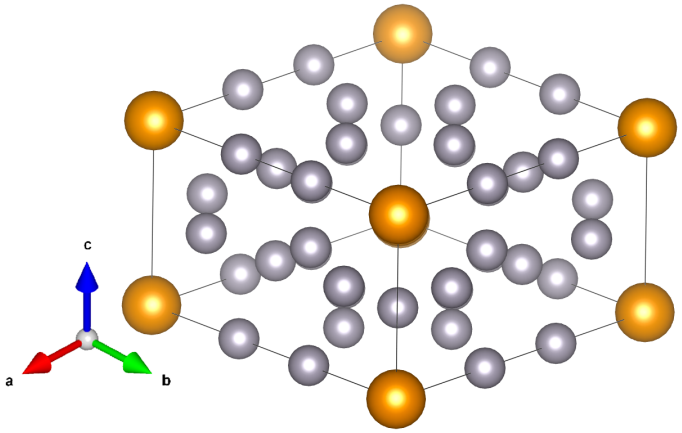

Figure 10: Crystal structure of RT_{12} phase, with rare-earth atoms in yellow, and transition metal atoms in grey. The arrows in the picture indicate the crystal's lattice directions a, b, and c.

As time has gone on however, market conditions and government programs have overcome this initial hurdle and interest in this phase has increased again. A lot of this interest has been driven by a paper from Miyake et al.[49], which studied the magnetic properties of $NdFe_{12}$, $NdFe_{11}Ti$, and $NdFe_{11}TiN$ from first principles. This work found that the reduction of titanium and interstitial nitrogen addition could improve the material's magnetisation, curie temperature, and the strength of its uni-axial magnetocrystalline anisotropy. To test this result, Hiriyama et al. grew $NdFe_{12}$, $NdFe_{12}N$, and $SmFe_{0.8}Co_{0.2}$ epitaxially via sputtering[50, 51] and found that thin film $NdFe_{12}N$ had superior magnetic properties to $Nd_2Fe_{14}B$ with a magnetic saturation $\mu_0 M_s \approx 1.78$T, anisotropy field of $\mu_0 H_a \approx 8$T, and curie temperature $T_C \approx 823\mathrm{K}$. A significant proportion of the work in this thesis is directly dedicated to understanding and stabilising this phase specifically, using the techniques of element substitution[1], interstitial element addition[2], and grain morphology control.

1.5 Atomistic Simulations

Atomistic simulations were first performed in the Los Alamos laboratory. Work on this subject, published in 1949 by Metropolis and Ulam, introduced the Monte Carlo Method[52]. Making use of newly established computational resources, this statistical method allowed for the investigation of complex problems in classical dynamics and

quantum mechanics by a random sampling approach. In 1955 Fermi et al.[53] used these techniques to study the equipartition of energy between the degrees of freedom in a 1D crystal structure consisting of 64 particles on the MANIAC I electronic computing system. The use of electronic computing systems opened up a new avenue for solving complex problems numerically.

Within the next four years Wainwright and Alder developed these ideas into a methodology which solved classical dynamics' many body problem by integrating a solution over a series of time steps. The paper published in 1959 established the basics of Molecular Dynamics[54]. The idea behind the theory was to parameterise interatomic interactions using potentials, and allow them to evolve dynamically by integrating their equations of motion in successive timesteps. As this does not rely on the same random sampling used by Monte Carlo simulations, they can be considered fundamentally separate methodologies. Owing to its dynamical nature, Molecular Dynamics allowed researchers to study previously impractical phenomena such as molecular transport, and fluid dynamics[55]. Over time the methodology has developed into one of the principle tools in the computational scientists toolbox, finding applications in a broad array of fields, such as molecular biology and nuclear physics. It is the principle methodology used in this work, and a thorough discussion of its methods is given in the following chapter on numerical methods.

Another predominant theory used for atomistic simulation is Density Functional Theory (DFT). The idea was established in two papers, one by L. H. Thomas[56], and the other by Fermi which developed a method for calculating the electric field in an atom from first principles. Hohenberg and Kohn[57] expanded on these theories in 1964, allowing the precise functional of an atom to be calculated in the presence of a static or slowly varying field. The theory was finally generalised in 1979 by Levy[58].

The most recent development in the field came in 1985 when Car and Parinello[59] combined the main results of both theories to produce the Ab-initio Molecular Dynamics theory of computational simulation. This combination uses the precise electronic structure calculations from density functional theory as the pair potentials in Molec-

ular Dynamics. Modelling in this manner allows the theory to deal with previously unapproachable problems such as covalent bonding in metals. Ab initio simulations are still used to this day, and are considered the current pinnacle of atomistic simulations. However, owing to their extremely high computational cost, previous theories with less computational work, such as Molecular Dynamics, persist also.

2 Numerical Methods

This section contains a summary of the numerical methods used throughout the thesis, beginning with the principles underlying molecular dynamics, the development of pair potentials through genetic algorithms, and the more specific use of molecular dynamics in temperature simulations. Followed by a section on the structural optimisation of crystals, an explanation of Boltzmann probabilities and how they can be used to produce Boltzmann Factors, and finally their specific use in the present work to produce "cascading probabilities", a method for the deeper analysis of substitution position probability.

2.1 Molecular Dynamics

Molecular dynamics evolved from the need for a solution to the so called "many body problem", formulated in the 17th century by Newton when it was found that his predictions for planetary motion were flawed[60]. Newton realised the flaw in his predictions was derived from the cross interaction of all the planets with one another, but it was not possible to produce analytical equations to predict this interaction and the subsequent motion. To this day it is not possible to produce efficient analytical solutions for the evolution of a system of N bodies - in this case particles/ atoms. Therefore, in order to understand interactions involving many particles, a solution is calculated via numerical methods. Molecular Dynamics is one such method that uses Newton's second law to formulate equations of motion, which can sequentially solve for the movement of many particles in discrete time steps. The integration of these equations makes the method deterministic and allows it to mirror the dynamics of a real system. Numerous simulation codes use this general methodology, however, in this work one code has been used: Large-scale Atomic/Molecular Massively Parallel Simulator (LAMMPS)[61]. The general methodology underlying this code will be elucidated, then a further section will detail how LAMMPS can be used to perform melting point calculations. Although there are a number of references on the basics of molecular dynamics, the three main ones used here are [62], [63], and [64]. The first two offer a general overview and the final

one a more specific overview of LAMMPS.

2.1.1 Methodology

Initialisation

The beginning of any molecular dynamics simulation is initialisation, during which ubiquitous simulation properties are set. The most important of these are: atomic masses, time step length, number of particles, boundary conditions, units, and pair potential equations[65].

Time step length is particularly important in molecular dynamics simulations, and is typically chosen so that it represents a fraction of the period of the structure's highest frequency vibrational mode. Calculating these modes can be done experimentally using vibrational spectroscopy[66], the most accurate method being neutron scattering. A common choice is 1fs as this is generally significantly smaller than the time period of the highest vibrational frequency in most materials. Choosing a timestep which is too large will inevitably fail to capture parts of the material's dynamics, causing particles to drift away from their "True" trajectories - the expected trajectories in the real world. Deviation from realistic trajectories can produce unphysical particle positions that cause atoms to repel each other with extremely large forces and hence steadily increase the energy of the system as a whole, an effect known as "energy drift".

Initial particle positions are defined on a 3D axis, whose origin can be set arbitrarily by defining the boundary placement of the simulation box. Initial particle positions must be defined so that the system either evolves into the state of interest (in the case of liquids or gasses), or already represents the structure of interest (in the case of crystalline or amorphous solids). In either case the particles must be positioned in a structure that does not result in an unphysical overlap, as this would cause large forces to accelerate particles away from one another destroying the system in the process. To avoid this, a system should be initialised in the crystal lattice of the simulated structure, or in the case of a liquid a cubic lattice of arbitrary dimensions as suits the simulation's requirements.

Once in position particle velocities can be initialised, this is done by assigning a velocity to each atom at random on the interval $[-0.5, 0.5]$ ms^{-1}[62] and then altering each velocity slightly so that the total momentum of the whole system is zero. To do this the momentum of each particle can be summed, giving:

$$\boldsymbol{P}_T = \sum_{i=1}^{N} \boldsymbol{p}_i \tag{2.1}$$

where $\boldsymbol{P}_T$ represents the total system momentum, $\boldsymbol{p}_i$ is the momentum of particle i, and N is the total number of particles in the system. In order to zero the momentum of the entire system each atom's momentum should be shifted by the momentum vector $\boldsymbol{p}_s = \frac{\boldsymbol{P}_T}{N}$, where $\boldsymbol{p}_s$ is the individual momentum shift for each particle.

To get the velocity vector shift for each particle that achieves this the following is calculated:

$$\boldsymbol{v}_{i,s} = \frac{\boldsymbol{p}_s}{m_i} \tag{2.2}$$

where $\boldsymbol{v}_{i,s}$ is the shifted velocity of particle i due to $\boldsymbol{p}_s$ and m_i is the mass of particle i. Giving a new velocity vector for each particle:

$$\boldsymbol{v}_i{}' = \boldsymbol{v}_i - \boldsymbol{v}_{i,s} \tag{2.3}$$

where $\boldsymbol{v}_i{}'$ is the shifted velocity of particle i and $\boldsymbol{v}_i$ is the original velocity of particle i. Time is not included in this equation because all of the velocities are at $t = 0$. Once the system's velocities have been shifted to give it zero average momentum the velocity vectors can be rescaled to match a given initial temperature. To find the rescaling factor, first, the system's instantaneous temperature is calculated using the following relation from statistical mechanics for each degree of freedom of each particle[67]:

$$\left\langle \frac{1}{2} m_i v_{i,(x,y,z)}^2 \right\rangle = \frac{1}{2} k_B T \tag{2.4}$$

where the $\langle \dots \rangle$ angle brackets on the left hand side represent the average of the enclosed quantity, m_i is mass of particle i, $v_{i,(x,y,z)}$ is the magnitude of the particle i's velocity

along either the x, y, or z axis, k_B is the Boltzmann constant, and T is temperature. Summing over all the particles and all their degrees of freedom leads to the following equation for the instantaneous temperature of the system:

$$T(t) = \sum_{i=1}^{N} \frac{m_i v_i^2(t)}{k_B N_f} \tag{2.5}$$

where m_i is the mass of particle i, $v_i(t)$ is the velocity of particle i at time t, $T(t)$ is the instantaneous temperature at time t, N_f is the degrees of freedom of the system, and N is the total number of particles[65]. Time is included in this equation, because this general expression can be used to calculate the instantaneous temperature at any time t. Using the instantaneous temperature the following factor can be calculated and used to rescale each particles velocity vector:

$$S_f = \left(\frac{T}{T(t)} \right)^{\frac{1}{2}} \tag{2.6}$$

where S_f is the rescaling factor, T is the desired temperature, and $T(t)$ is the instantaneous temperature. With the system momentum at zero and the temperature at the desired level, the simulation can proceed to the general simulation loop, the first part of this loop is described below.

Pair Potentials and Force Calculations

Mathematically, Molecular Dynamics simulations all represent atoms as point masses which interact through some potential set which collectively defines the interactions between the elements present in the simulation. The potentials are repulsive at short range, maximally attractive at some equilibrium distance, and tail off to zero as the distance between the atoms grows. An example Lennard Jones potential[68] is shown in Figure 11 to illustrate this characteristic shape. In general potentials have a cut off beyond which it's assumed the interaction energy between two atoms is negligible enough to exclude its calculation. For a Lennard Jones potential this gives the mathematical

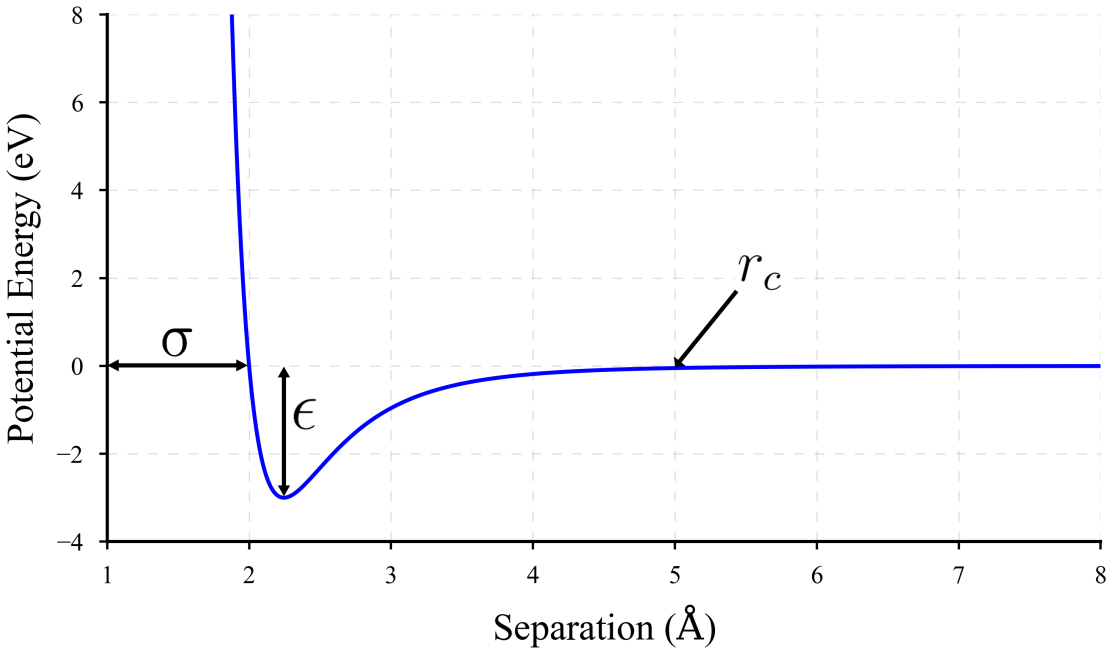

Figure 11: Example Lennard Jones potential, with the effect of each of the potential's constants indicated, please see Equation 2.7 to view these constants in the equation.

form shown in Equation 2.7.

$$u(r_{ij}) = \begin{cases} 4\epsilon \left[\left(\frac{\sigma}{r_{ij}}\right)^{12} - \left(\frac{\sigma}{r_{ij}}\right)^{6} \right] & \text{if } r_{ij} \leq r_c \\ 0 & \text{if } r_{ij} > r_c \end{cases} \tag{2.7}$$

where $u(r_{ij})$ is the potential energy between atoms i and j, r_{ij} is the magnitude of the vector $\boldsymbol{r_{ij}}$ between atoms i and j, ϵ is a scaling constant which controls the depth of the potential well, r_c is the potential's cut off point, and σ defines the point at which the energy between the two atoms is zero, therefore, this point defines at what proximity the two atoms begin to repel one another - σ also controls the width of the potential well. The Lennard Jones potential is an example of a pair potential, the simplest kind of potential that takes into account pair wise interactions only. For some potentials there are further three body or four body interactions, both types are used in this thesis. The work in this thesis is centred on metallic structures, which use Morse potentials[69]. For applicability these will be used to derive the equation for force calculations, to see a similar derivation for the Lennard Jones potential please see[70]. Morse potentials have

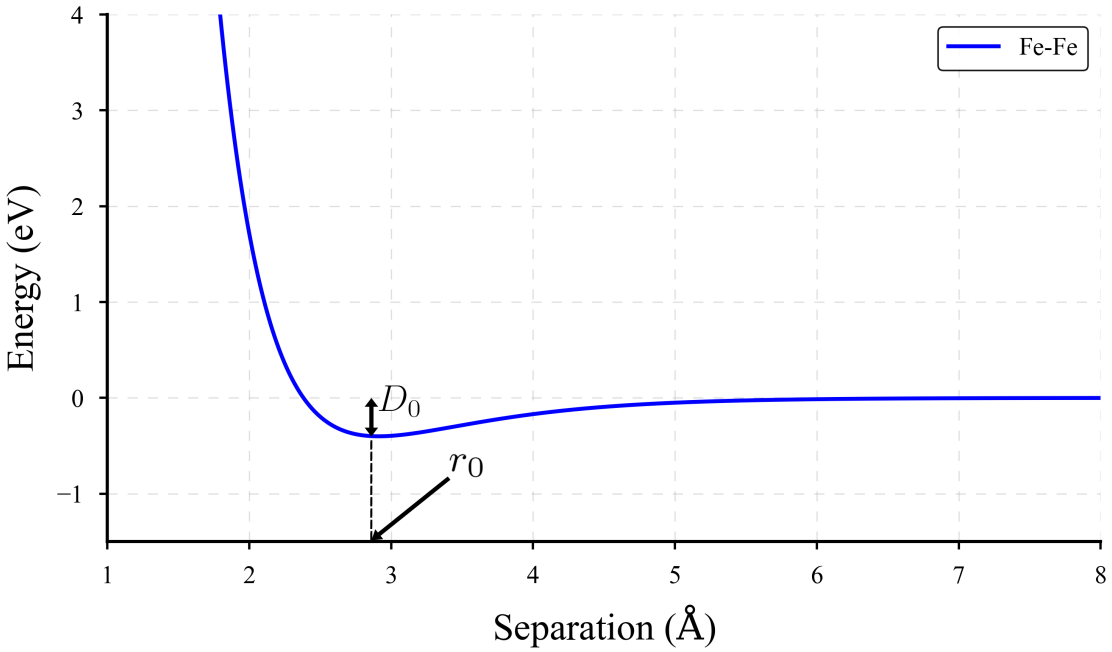

Figure 12: Morse potential of the iron-iron interaction used for work in this thesis. D_0 and r_0 are indicated on the graph.

the form shown in Equation 2.8:

$$u(r_{ij}) = \begin{cases} D_0 \left[e^{-2\alpha(r_{ij}-r_0)} - 2e^{-\alpha(r_{ij}-r_0)} \right] & \text{if } r_{ij} \leq r_c \\ 0 & \text{if } r_{ij} > r_c \end{cases} \tag{2.8}$$

where D_0 is a scaling constant which controls the depth of the potential well, α is a scaling constant that controls the width of the potential well, r_0 is a constant that defines the energy minimum of the well and is the distance at which the interaction is at equilibrium, r_c is the potential cut off distance, and r_{ij} is the magnitude of the vector between two atoms i and j. Figure 12 shows the form graphically for the Fe-Fe interactions used in this thesis. Taking the vector gradient of Equation 2.8 where $r_{ij} \leq r_c$ results in the force vector between atoms i and j:

$$\begin{aligned} \boldsymbol{f}_{ij} &= -\boldsymbol{\nabla} u(r_{ij}) \\ &= -\boldsymbol{\nabla} D_0 \left[e^{-2\alpha(r_{ij}-r_0)} - 2e^{-\alpha(r_{ij}-r_0)} \right] \quad \text{if } r_{ij} \leq r_c \end{aligned} \tag{2.9}$$

where $\boldsymbol{\nabla}$ represents the vector gradient equation which has the form given below:

$$\boldsymbol{\nabla} = \frac{\partial}{\partial x}\hat{\boldsymbol{i}} + \frac{\partial}{\partial y}\hat{\boldsymbol{j}} + \frac{\partial}{\partial z}\hat{\boldsymbol{k}} \tag{2.10}$$

subbing $u(r_{ij})$ into Equation 2.9 leads to:

$$\boldsymbol{\nabla} u(r_{ij}) = \frac{\partial u(r_{ij})}{\partial x}\hat{\boldsymbol{i}} + \frac{\partial u(r_{ij})}{\partial y}\hat{\boldsymbol{j}} + \frac{\partial u(r_{ij})}{\partial z}\hat{\boldsymbol{k}} \tag{2.11}$$

Using the chain rule each of these terms can be separated out to get the following:

$$\begin{aligned} \frac{\partial u(r_{ij})}{\partial x} &= \frac{\partial r_{ij}}{\partial x}\frac{\partial u(r_{ij})}{\partial r_{ij}} \\ \frac{\partial u(r_{ij})}{\partial y} &= \frac{\partial r_{ij}}{\partial y}\frac{\partial u(r_{ij})}{\partial r_{ij}} \\ \frac{\partial u(r_{ij})}{\partial z} &= \frac{\partial r_{ij}}{\partial z}\frac{\partial u(r_{ij})}{\partial r_{ij}} \end{aligned} \tag{2.12}$$

As r_{ij} is a vector magnitude it's form can be given as:

$$r_{ij} = |\boldsymbol{r}_{ij}| = \sqrt{x^2 + y^2 + z^2} = \left(x^2 + y^2 + z^2\right)^{\frac{1}{2}} \tag{2.13}$$

since

$$\boldsymbol{r}_{ij} = x\hat{\boldsymbol{i}} + y\hat{\boldsymbol{j}} + z\hat{\boldsymbol{k}} \tag{2.14}$$

The form given in Equation 2.13 can be differentiated to give:

$$\frac{\partial r_{ij}}{\partial x} = \frac{x}{r_{ij}} \tag{2.15}$$

$$\frac{\partial r_{ij}}{\partial y} = \frac{y}{r_{ij}} \tag{2.16}$$

$$\frac{\partial r_{ij}}{\partial z} = \frac{z}{r_{ij}} \tag{2.17}$$

Substituting Equations 2.15, 2.16, and 2.17 back in to Equation 2.12, and performing the partial differential, $\frac{\partial u(r_{ij})}{\partial r_{ij}}$, gives the following equations:

$$\begin{aligned}
\frac{\partial u(r_{ij})}{\partial x} &= \frac{x}{r_{ij}} D_0 \left[(-2\alpha)\, e^{-2\alpha(r_{ij}-r_0)} - (-2\alpha) e^{-\alpha(r_{ij}-r_0)}\right] \\
\frac{\partial u(r_{ij})}{\partial y} &= \frac{y}{r_{ij}} D_0 \left[(-2\alpha)\, e^{-2\alpha(r_{ij}-r_0)} - (-2\alpha) e^{-\alpha(r_{ij}-r_0)}\right] \\
\frac{\partial u(r_{ij})}{\partial z} &= \frac{z}{r_{ij}} D_0 \left[(-2\alpha)\, e^{-2\alpha(r_{ij}-r_0)} - (-2\alpha) e^{-\alpha(r_{ij}-r_0)}\right]
\end{aligned} \tag{2.18}$$

Substituting the equations from 2.18 back in to Equation 2.11 results in:

$$\begin{aligned}
\boldsymbol{\nabla} u(r_{ij}) &= D_0 \left[(-2\alpha)\, e^{-2\alpha(r_{ij}-r_0)} - (-2\alpha) e^{-\alpha(r_{ij}-r_0)}\right] \left(\frac{1}{r_{ij}}\right) \left(x\hat{\boldsymbol{i}} + y\hat{\boldsymbol{j}} + z\hat{\boldsymbol{k}}\right) \\
&= (-2\alpha) D_0 \left[e^{-2\alpha(r_{ij}-r_0)} - e^{-\alpha(r_{ij}-r_0)}\right] \hat{\boldsymbol{r}}_{ij}
\end{aligned} \tag{2.19}$$

where:

$$\hat{\boldsymbol{r}}_{ij} = \frac{\boldsymbol{r}_{ij}}{r_{ij}} = \left(\frac{1}{r_{ij}}\right) \left(x\hat{\boldsymbol{i}} + y\hat{\boldsymbol{j}} + z\hat{\boldsymbol{k}}\right) \tag{2.20}$$

Substituting 2.19 into Equation 2.9 gives:

$$\boldsymbol{f}_{ij} = (2\alpha) D_0 \left[e^{-2\alpha(r_{ij}-r_0)} - e^{-\alpha(r_{ij}-r_0)}\right] \hat{\boldsymbol{r}}_{ij} \tag{2.21}$$

Equation 2.21 can be used to calculate the force on every atom i due to its interaction with neighbouring atoms j by Newton's Second Law of motion:

$$\begin{aligned}
m\ddot{\boldsymbol{r}}_i = \boldsymbol{f}_i &= \sum_{\substack{j=1 \\ (j \neq i)}}^{N} \boldsymbol{f}_{ij} \\
\ddot{\boldsymbol{r}}_i &= \frac{1}{m} \sum_{\substack{j=1 \\ (j \neq i)}}^{N} \boldsymbol{f}_{ij}
\end{aligned} \tag{2.22}$$

Calculating the force on each atom and the associated acceleration is the preliminary step of the algorithm which updates atomic positions. The process of updating positions is known as time integration, and is explained in a separate section.

Boundary Conditions

Every simulation takes place within a defined region, depending on the simulation type this region can differ. Simulations in the Canonical Ensemble (NVT simulations), which occur at constant volume and temperature, have their region defined at the start of the simulation. Whilst Isothermal-Isobaric (NPT simulations), which occur at constant pressure and temperature, alter their regions as the system evolves to achieve the correct pressure.

The interaction of particles with the simulation region boundaries are known collectively as "boundary conditions". These boundary conditions generally come in two main types, fixed boundary conditions and periodic boundary conditions.

Fixed boundary conditions define the limit of the simulation cell, acting as hard boundaries to further atomic movement. This method is limited by the fact that simulation breakdown will occur if an atom moves beyond these boundaries. To prevent this, it's possible to add repulsive potentials to the boundaries that cause particles to reflect as they approach. However, because most Molecular Dynamics simulations are quite small, on the order of 10^4 or 10^6 atoms, particles which are affected by this potential can grow to be a significant minority and even a majority of the simulation. As these particles cease to accurately represent particles in the bulk, fixed boundary conditions will have an effect on the macroscopic properties of a system beneath the thermodynamic limit[71]. To avoid this, and still represent macroscopic systems in microscopic form, periodic boundary conditions can be used in place of fixed ones. The periodic boundary method creates virtual copies of the simulation environment in all directions, treating the original simulation region as a primitive unit cell. The virtual simulation regions provide virtual particles, which interact with particles in the original simulation region. A two dimensional example of this is shown in Figure 13. As can be seen, interactions occur between the simulation particle and virtual particles across the boundary.

Further, particles that cross a periodic boundary re-emerge through the opposite one. Computationally this is achieved by a momentum preserving coordinate alteration,

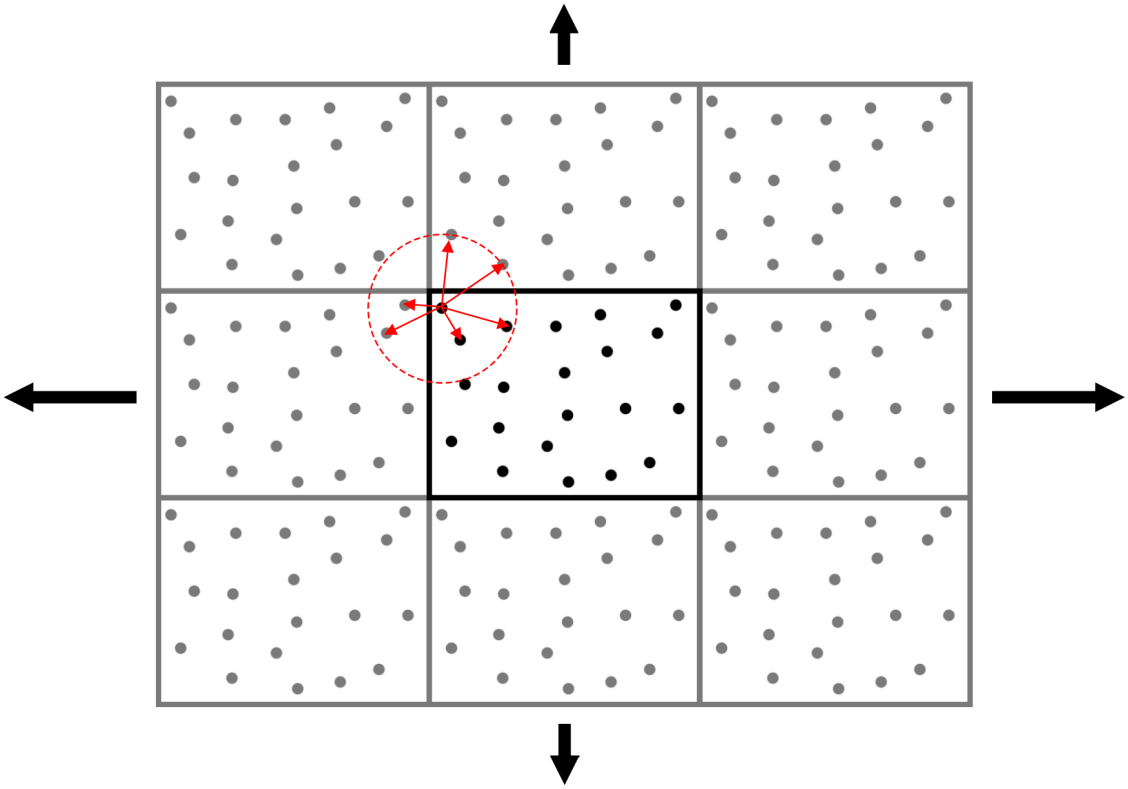

Figure 13: 2D visualisation of periodic boundary conditions. The main simulation region is outlined in black, surrounded by numerous identical virtual simulation regions outlined in grey. The red circle shows the interaction cut off point for one particle in the simulation, and the red arrows indicate the particles it interacts with. The arrows indicate that further virtual simulation regions can be created if necessary.

but conceptually it can be thought of as an exchange of particles between the original simulation and a pair of virtual simulations. Two such particle exchanges are illustrated in Figure 14, which shows the paths of two particles passing from the original simulation region into a virtual simulation region. As can be seen, the particle behaviour is mirrored by a secondary virtual simulation region opposite the first, which passes its virtual version of the particle back into the original simulation region.

These boundary conditions are achieved mathematically/ programmatically by: A) including all virtual particles in the extended particle list used for finding nearest neighbour pairs in force calculations, and B) Using an operator to shift particle positions when they leave the simulation region[72]. An example of a shift operator, assuming a

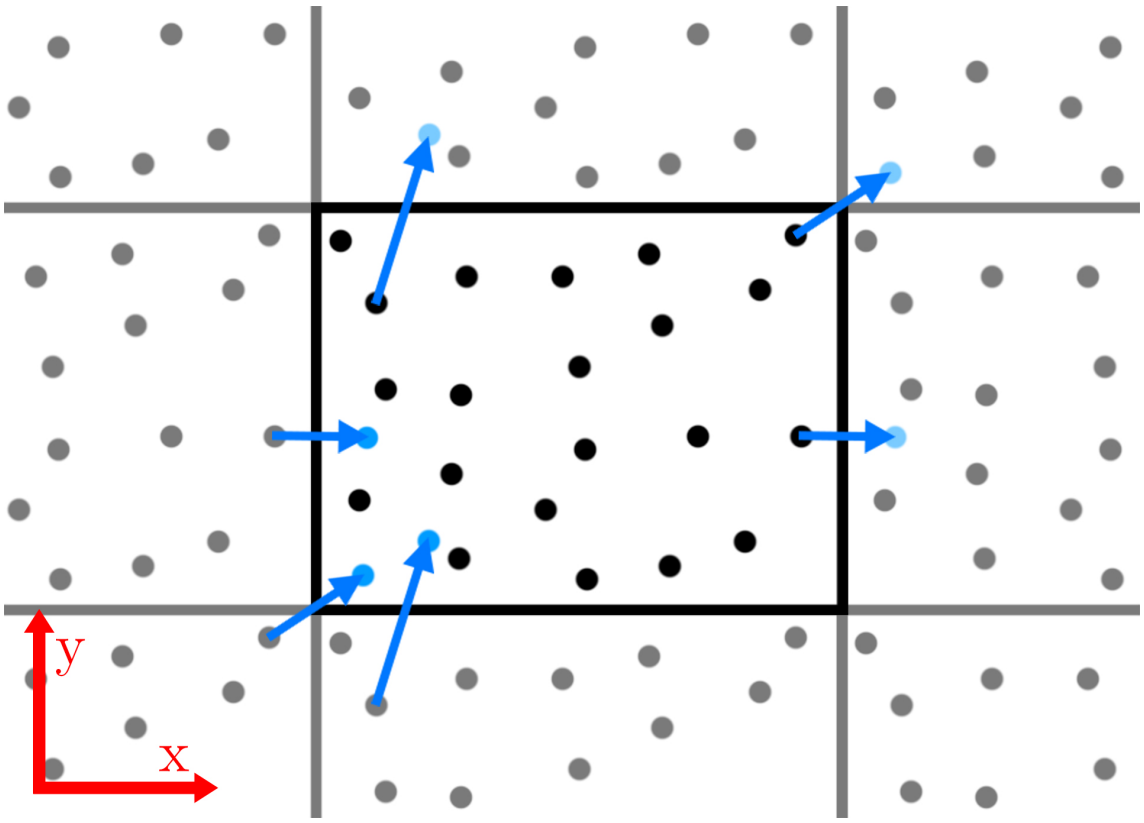

Figure 14: Two dimensional representation of particles crossing from the original simulation region into virtual simulation regions, with the corresponding virtual particle from the opposite virtual region crossing into the original simulation region. Three transfers are shown, one in which the particle crosses the x boundary, another which crosses the y boundary, and a final transfer which shows a particle crossing the x and y boundary. The x and y directions are indicated in the bottom left corner.

rectangular simulation region, is shown in Equation 2.23:

$$\boldsymbol{S}_{(x,y,z)}(r_{i,(x,y,z)}) = \begin{cases} r_{i,(x,y,z)} & \text{if} \quad 0 < r_{i,(x,y,z)} \leq L_{(x,y,z)} \\ r_{i,(x,y,z)} - L_{(x,y,z)} & \text{if} \quad r_{i,(x,y,z)} > L_{(x,y,z)} \\ r_{i,(x,y,z)} + L_{(x,y,z)} & \text{if} \quad r_{i,(x,y,z)} < 0 \end{cases} \tag{2.23}$$

where the notation (x, y, z) indicates any of the three axes can be used in the equation, $\boldsymbol{S}_{(x,y,z)}$ is the shift operator for one of the three axes x, y, z, $r_{i,(x,y,z)}$ is the coordinate of particle i along one of the x, y, z axes, and $L_{(x,y,z)}$ is the length of the simulation box along one of the x, y, z axes. At every time step this operator can be applied to each particle and change its coordinates if necessary without altering its momentum.

The wrap around effect produced by periodic boundaries allows a very small region to

approximate an infinite space, and thus simulate the behaviour of particles in the bulk. However, if the interaction length of the pair potentials is over half the smallest region size, particles can interact with multiple copies of the same atom producing spurious effects[73]. Less directly, if particle behaviour is correlated over long ranges, particles can interact with themselves through their neighbours, producing oddities such as infinite travelling waves. The possibility of these finite size effects should always be taken into account when defining the simulation region.

Time Integration of Particle Positions

Once the simulation has been initialised the program enters its main loop, calculating particle positions at successive time steps. This process requires the force calculations from Equation 2.21 and the position of the particles at the previous two time steps. These are combined into an equation which calculates the next particle position. The equation used to find the next position varies, but the most common methods are variations of Verlet integration. The derivation of this method can be found in Understanding Molecular Simulation[74], and is presented below.

Taking the Taylor expansion of one of a particle's coordinates (x, y, z) gives the following form:

$$\begin{aligned} r(t+\triangle t) &= \frac{r(t)}{0!} + \frac{\triangle t}{1!}\frac{dr(t)}{dt} + \frac{\triangle t^2}{2!}\frac{d^2r(t)}{dt^2} + \frac{\triangle t^3}{3!}\frac{d^3r(t)}{dt^3} + \mathcal{O}\left(\triangle t^4\right) \\ r(t-\triangle t) &= \frac{r(t)}{0!} - \frac{\triangle t}{1!}\frac{dr(t)}{dt} + \frac{\triangle t^2}{2!}\frac{d^2r(t)}{dt^2} - \frac{\triangle t^3}{3!}\frac{d^3r(t)}{dt^3} + \mathcal{O}\left(\triangle t^4\right) \end{aligned} \tag{2.24}$$

where, $r(t)$ is the position coordinate for a particle in x, y, or z, $\triangle t$ is the time step, and the $\mathcal{O}\left(\triangle t^4\right)$ is big O notation for: some function on the order of $\triangle t^4$. Adding together the equations in 2.24 gives the following:

$$\begin{aligned} r(t+\triangle t) + r(t-\triangle t) &= 2\frac{r(t)}{0!} + 2\frac{\triangle t^2}{2!}\frac{d^2r(t)}{dt^2} + \mathcal{O}\left(\triangle t^4\right) \\ &= 2r(t) + \triangle t^2\frac{d^2r(t)}{dt^2} + \mathcal{O}\left(\triangle t^4\right) \end{aligned} \tag{2.25}$$

As $\frac{d^2r(t)}{dt^2}(t) = a(t)$ and $f(t) = ma(t)$, $a(t) = \frac{f(t)}{m}$ can be substituted into the Equation 2.25 to get the following:

$$\begin{aligned} r(t+\triangle t) + r(t-\triangle t) &= 2r(t) + \triangle t^2 \frac{f(t)}{m} + \mathcal{O}\left(\triangle t^4\right) \\ r(t+\triangle t) &= 2r(t) - r(t-\triangle t) + \triangle t^2 \frac{f(t)}{m} + \mathcal{O}\left(\triangle t^4\right) \end{aligned} \tag{2.26}$$

By choosing a very small time step, the $\mathcal{O}\left(\triangle t^4\right)$ term can be disregarded and the equation simplified to:

$$r(t+\triangle t) \approx 2r(t) - r(t-\triangle t) + \triangle t^2 \frac{f(t)}{m} \tag{2.27}$$

This produces a compounding error on the order of $\triangle t^4$ but as this value is very small compared to the remainder of the equation it's safe to omit. Equation 2.27 shows that calculating a particle's next position requires its position at the current and preceding time step, along with its total force calculation at the current time step.

Algorithms like Equation 2.27 are used because they preserve the accessible area of the particle system's phase space. This means that at some given energy E, the states which the system can reach remains roughly the same and there is no long term drift in total system energy.

Whilst there are higher order integration methods which can give greater accuracy in particle position, all methods will suffer from numerical instability at some point, and deviate from the true particle trajectory sooner or later. Therefore, it is far more important to preserve the macroscopic quantities of the system, such as total energy. For this purpose the algorithm with the lowest computational cost, above a certain accuracy, is preferred. Equation 2.27 fits these criteria.

Thermostats and Barostats

Alone, the above methodology can only produce systems in the Microcanonical (NVE) ensemble, for which energy, volume and particle number are conserved. This

restricts the states the system can reach to a single energy, which makes it hard to compare computed results with real world experiments, as most real world experiments occur at constant temperature, particle number, and volume (NVT), or constant temperature, particle number, and pressure (NPT). The NVT ensemble is known as the Canonical ensemble, and the NPT ensemble as the Isothermal-Isobaric ensemble.

Two methodologies are used to replicate these ensembles in Molecular Dynamics. The first, stochastically couples the system to a known ensemble through a quasi Monte Carlo method[75]. The second, couples the system to a given ensemble by the addition of an extra term to each particles equation of motion, the term serves to constrain the system as a whole to the chosen ensemble[76].

An example of the former case is the Andersen Thermostat[75], which models stochastic collisions between the system and a theoretical heat bath by selecting particles and giving them a momentum from the Maxwell-Boltzmann distribution, shown in Equation 2.28.

$$\mathcal{P}(\boldsymbol{p}) = \left(\frac{\beta}{2\pi m}\right)^{3/2} \exp\left[\frac{-\beta p^2}{2m}\right] \tag{2.28}$$

where p is momentum magnitude, $\mathcal{P}(p)$ is the probability of momentum magnitude p, $\beta = 1/k_B T$ where k_B is the Boltzmann constant and T is temperature, and m is mass. As the choice of momentum matches this distribution, the Andersen Thermostat can effectively put the system in the Canonical ensemble at temperature T.

The strength of coupling to the heat bath is defined by the frequency at which these collisions occur v, so that for each timestep $\triangle t$ there should be $v\triangle t$ collisions. The main problem with this method, is that it destroys the time reversibility of the system, making it impossible to study dynamic properties.

An improvement on this method, and an example of the latter case is the Nose-Hoover thermostat[76]. In this method an extra term is added to the equation of motion for every particle, which adds a positive or negative friction to the particle's motion. This term acts to either speed up or slow down each particle depending on the whole systems deviation from, for example, a desired temperature T_D. The modified

equations of motion take the following form:

$$m_i \frac{d^2 \boldsymbol{r}_i}{dt^2} = \boldsymbol{F}(\boldsymbol{r}_i) - \zeta \left(\boldsymbol{r}_i, \frac{d\boldsymbol{r}_i}{dt} \right) \frac{d\boldsymbol{r}_i}{dt} \tag{2.29}$$

where $\frac{d^2 \boldsymbol{r}_i}{dt^2}$ is the acceleration of particle i, m_i is the mass of particle i, $\boldsymbol{F}(\boldsymbol{r}_i)$ is the force on particle i, $\zeta(\boldsymbol{r}_i, \frac{d\boldsymbol{r}_i}{dt})$ is the frictional term that scales particle velocity, and $\frac{d\boldsymbol{r}_i}{dt}$ is the velocity of particle i. For the Nose-Hoover thermostat ζ is defined by its differential with respect to time, which is given in the following equation:

$$\frac{d\zeta}{dt} = \frac{(\sum_i m_i v_i^2) - 3N k_B T_D}{Q} \tag{2.30}$$

where v_i^2 is the velocity of particle i squared, N is the number of particles, k_B is the Boltzmann constant, T_D is the desired temperature, and Q is an adjustable parameter that defines the coupling strength between the system and the heat bath[77]. The numerator in this equation represents the system's deviation from the average kinetic energy it's expected to have in the Canonical ensemble. The expected average velocity can be calculated from each of the system's velocity component averages using Equation 2.4[67]. Taking into account the system's three degrees of freedom results in the following average square velocity for each particle:

$$\begin{aligned} \frac{1}{2} m_i \left\langle v_{i,x}^2 \right\rangle + \frac{1}{2} m_i \left\langle v_{i,y}^2 \right\rangle + \frac{1}{2} m_i \left\langle v_{i,z}^2 \right\rangle &= \frac{3}{2} k_B T \\ \frac{1}{2} m_i \left\langle v_i^2 \right\rangle &= \frac{3}{2} k_B T \end{aligned} \tag{2.31}$$

This can be used to demonstrate that the kinetic energies of the particles in a system in the Canonical Ensemble should sum to equal N times $\frac{3}{2} k_B T$. In Equation 2.30 the factor of $\frac{1}{2}$ has been taken into the denominator Q. The result of Equation 2.30 is that any deviation from the desired temperature T_D will cause a change in the friction constant ζ, which over time will damp the system into the Canonical ensemble. The speed at which the system changes to match the desired distribution is governed by Q. This parameter must be chosen carefully, otherwise unphysical oscillations in energy cause the system to leave the canonical ensemble.

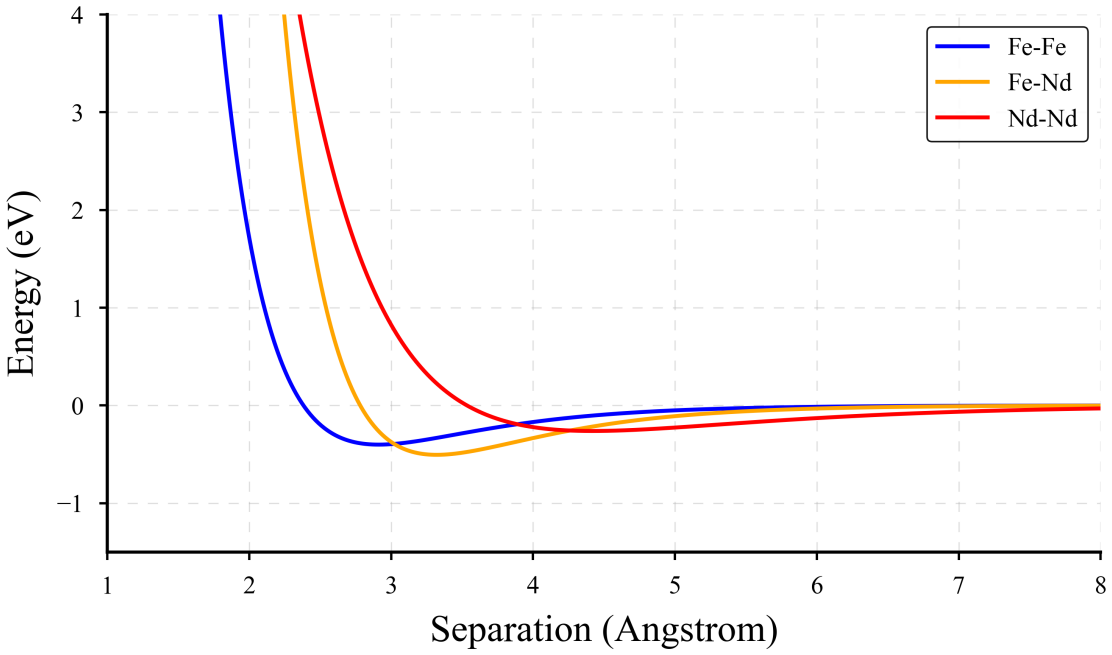

Figure 15: Morse potentials for Fe-Fe, Fe-Nd, and Nd-Nd.

Similar to the above thermostat, system dynamics can have volume built into them to produce a barostat. In this way volume can be altered to keep the pressure at some constant value.

2.1.2 Pair Potential Development

Pair potentials are an approximation to an underlying truth. In molecular dynamics they're based on a physically motivated functional form that has been empirically derived to reproduce some properties of reality - in this case macroscopic and microscopic crystal properties. Each functional form is defined by a finite number of constants. By varying the constants, a pair potential can be fit to macroscopic properties obtained from experimental data, or macroscopic and microscopic properties obtained from ab initio data. Whilst the amount of data available from ab initio methods is significantly higher, it is based on calculations at 0K and thus may not be appropriate for all purposes.

To examine the process of pair potential development, we will use the Morse functional form from the previous section. Figure 15 shows three of these Morse potentials, which were refit to match experimental data.

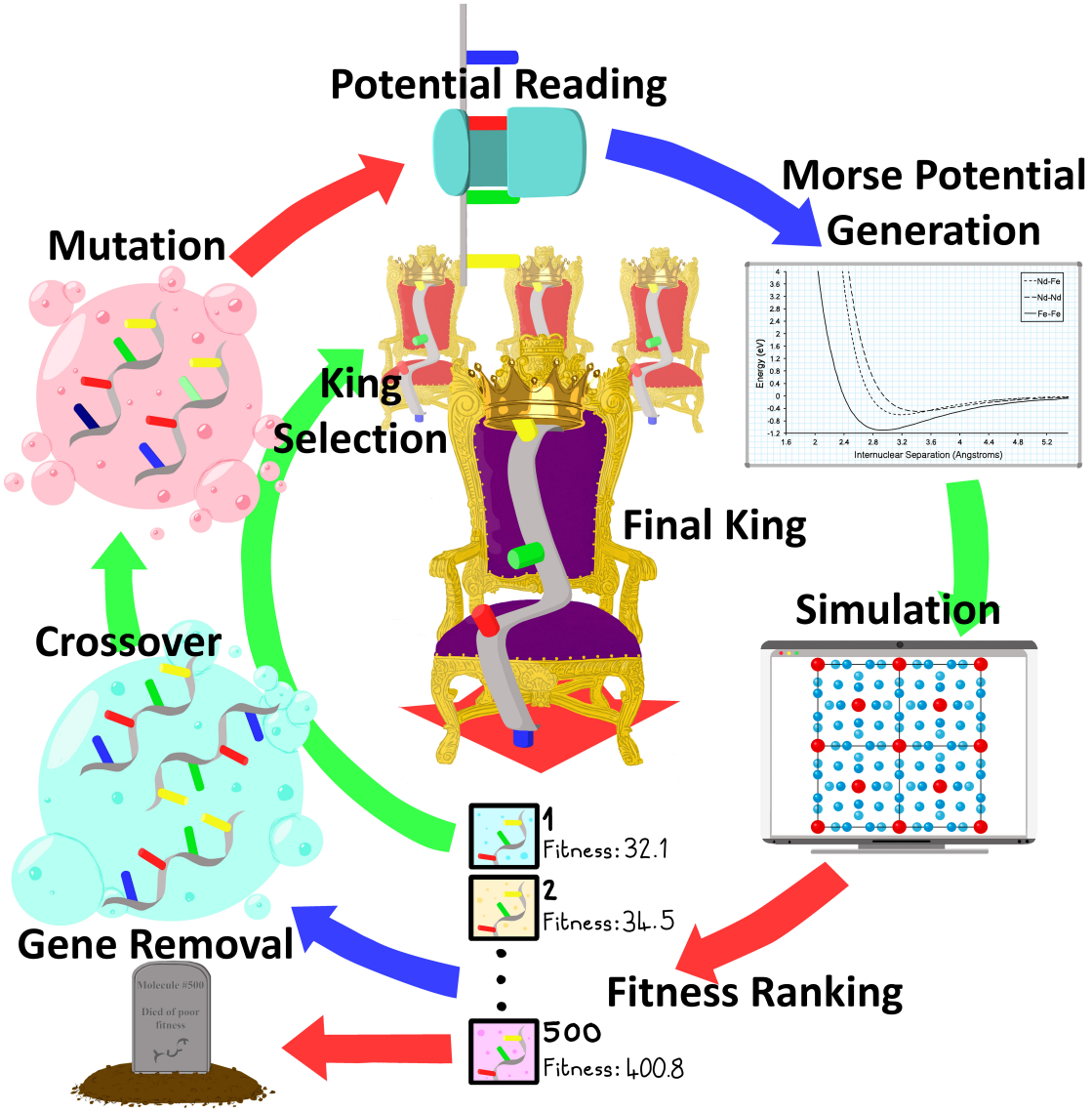

Figure 16: Visual representation of the Genetic algorithm process.

There are four constants in this potential: D_0 for controlling the potential well depth, α for controlling the potential well width, r_0 for controlling the minimum energy distance, and r_c for controlling the potential's cut off distance.

Fitting a potential to match experimental data is an old idea, and was alluded to by Morse in his own 1929 paper[69], in which he introduced the potential as an approximation to the potential energy between two nuclei in a diatomic molecule. He suggests that as the precise expression for this potential cannot be known, that an approximation should be used and its constants adjusted to match experimental data. The following section discusses one method for fitting a functional form to experimental data.

Genetic Algorithms

Genetic Algorithms are a nature inspired computational method[78, 79]. Typically, they are used when a problem needs to optimise an undifferentiable function or when a problem is likely to have multiple local optima. They are also useful when good solutions to a problem are sparsely spread across a search space, or when the parameters of a problem are likely to be interconnected[79]. In this thesis, Genetic Algorithms are used to solve an optimisation problem which matches all of the above criteria. They make use of data structures that represent short sequences of genetic code (genes), where each gene contains all the information required to form a solution to some posed problem. For example, in the case of a Morse potential, the posed problem could be finding the potential that most accurately produces known cohesive energies for a given structure - making the genes a parameter set that define a Morse potential.

In the above scenario, the steps comprising a basic implementation of the algorithm are given below:

1. Generate a population of genes, in which all the parameters forming the Morse potential are completely random.
2. Using each gene in the population calculate cohesive energy.
3. Rank order the genes by their proximity to the correct cohesive energy, high rank or "good" genes are those which are closest to the energy.
4. Remove the low rank genes from the population and repopulate with more genes, using Crossover and Mutation operators (explained later).
5. Move to step 2 and repeat the process with the new population of genes.

Although simple, this example contains the basics of the Genetic Algorithm method. The steps are shown graphically in Figure 16. A detailed explanation of each step is given below, along with the implementation specifics of the Genetic Algorithm used in Chapter 4 of this thesis - a custom code written in Python that follows conventional Genetic Algorithm practices using real numbers for the parameters.

Step 1: Generating a Population

The first step in the above algorithm is an initialisation step, occurring only once at the start of the problem. This initial step produces an initial set of genes which broadly cover most of the probable parameter space - a mathematical abstraction that represents all possible combinations of gene parameters. The probable parameter space is a subsection of all the possible combinations that past experience or outside considerations have shown are likely to hold the correct answer. The broadness of this space will differ from problem to problem, and is dependent on the foreknowledge of the problem at hand. A simplified example of this is: "How many people should you invite for dinner when you have 10 steaks, 2kg of potatoes, and 5kg of assorted green vegetables?". You could probably guess the answer is around 10, based on your foreknowledge of how much people eat. The answer is certainly not 1,000,000, even though the algorithm would deem this an acceptable number of people to invite. To avoid unrealistic answers, the initial choice of the probable parameter space should reflect this. Figure 17 illustrates a simple parameter space and the region in which a genetic algorithm might start.

Taking any possible foreknowledge into account, genes are created at random by selecting from the range of parameter combinations that fall within the acceptable region. It is assumed that choosing the parameters at random will give a reasonable coverage of the parameter space. The first set of genes is deemed the first generation.

To ensure good coverage of the probable parameter space, the work in this thesis centred the initial parameter space around pre-existing potentials, which were already capable of producing reasonable results. The Morse potential methodology uses four parameters, making the optimisation's parameter space 4D. Trial and Error showed that a parameter variation $> \pm 20\%$ resulted in a completely deformed or un-computable structure. Therefore, initial parameter sets were created to have values in the range [-20%, -10%, 0%, +10%, +20%] of the original parameter. Creating the set in this way produced 625 parameter combinations which became the optimisation's first generation.

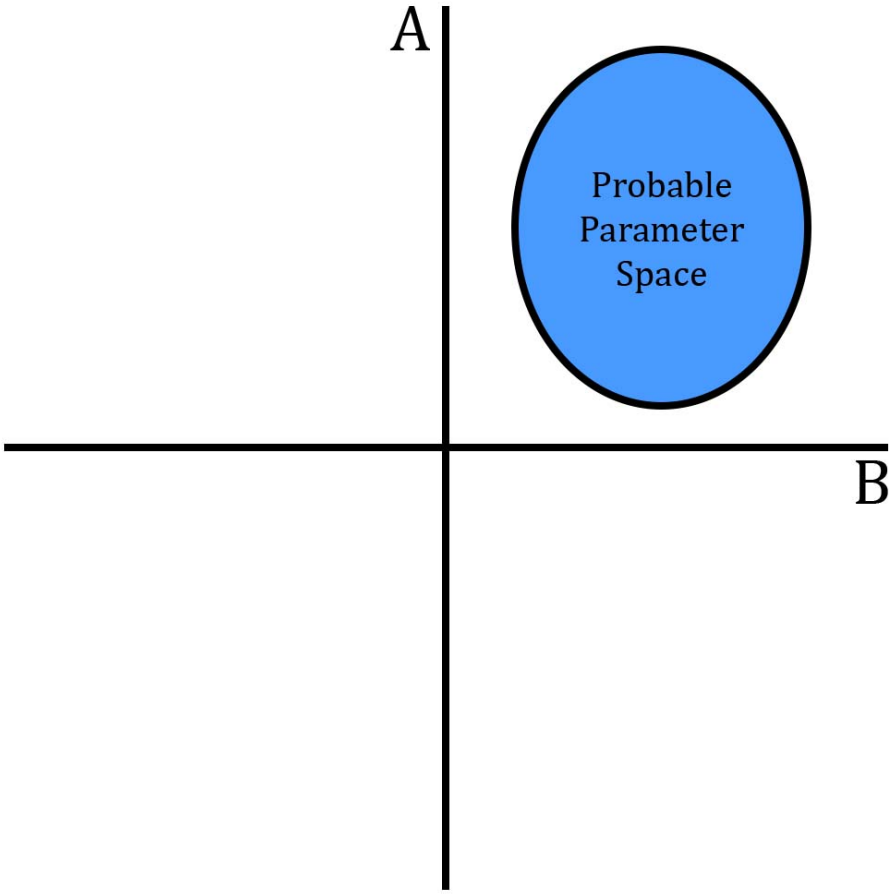

Figure 17: An illustration of a simple 2D parameter space with parameters A, and B. A hypothetical probable parameter space is circled in the first quadrant.

Step 2: Evaluating Genes

In the basic implementation this is simply written as "calculate cohesive energy", however in general this step is known as the evaluation step[79]. Evaluation allows the algorithm to quantify which genes are the *fittest*, and therefore which of them should *reproduce*. In none genetic terms, the algorithm decides how well each parameter set produces a desired result, and uses this to decide which sets propagate into the next iteration of the algorithm.

The evaluation step is governed by an *Evaluation Function* which is defined prior to the beginning of the algorithm. The *Evaluation Function* can in principle be anything whose results are reliant on the parameters in the genes. For example, to calculate cohesive energy the parameter set could be fed into a molecular dynamics simulation and used to perform an energy minimisation calculation. In this scenario the minimisation calculation is the *Evaluation Function*, and the cohesive energy is its output.

For the work in this thesis, cohesive energy, elastic constants, lattice parameters, bulk modulus, and Young's modulus were calculated using an energy minimisation calculation. In this case the *Evaluation Function's* output consists of multiple values, each of which needs to be considered when evaluating *fitness*, which is discussed in the next step.

Step 3: Assigning Fitness

A *Fitness Function* is some method of taking the output of the *Evaluation Function* and turning it into a measure of *fitness* for each gene. The ability to reproduce and propagate through the next iteration of the algorithm is dependent on this *fitness*.

In the simple case given in step 2, it suffices to rank the genes by their proximity or percentage deviation from the desired cohesive energy. The highest ranking or *fittest* genes being those that produce the least deviation.

For a complicated case with multiple outputs, the *Fitness Function* must take into account each of the *Evaluation Function's* outputs and combine them to produce a *fitness* for each gene. This can be done by weighting the importance of each output, so that the accuracy of the most important outputs has a larger effect on the *Fitness Function*. Such a *Fitness Function* can be written as follows:

$$F(O_g) = \sum_{i}^{N} w_i \frac{|O_{g,i} - E_i|}{E_i} \tag{2.32}$$

where $F(O_g)$ is the *Fitness Function* for the outputs of gene g, O_g is the *Evaluation Function's* outputs for gene g, N is the number of outputs, w_i is the weighting factor for output i, $O_{g,i}$ is the value of gene g's output i, and E_i is the expected value of output i. As Equation 2.32 shows, a good *fitness* is associated with a low value, with optimal *fitness* being a value of 0. The weighting factors w_i determine the importance of each output, and are defined at the start of the algorithm. To determine the weightings, consideration is given to which of the *Evaluation Function's* outputs are of greatest importance to the algorithm's success. For example, for Chapter 4 of this thesis, potentials were refit to get a closer approximation to melting temperature. In this case the reproduction

of the correct cohesive energy is of primary importance, and other constants, such as lattice parameters, are secondary. To reflect their relative importance, a weighting of w_1 was assigned to cohesive energy, and a weighting of w_2 to each lattice parameter, where $w_1 \gg w_2$. Assigning a larger weighting to the most important outputs amplified their relevance, ensuring that genes that were optimised to accurately produce important outputs were consistently ranked as the *fittest*.

Over successive generations this caused the genetic algorithm to converge on Morse potential parameters that produced solutions with high accuracy in cohesive energy and poorer accuracy in lattice parameters. To ensure the accuracy of the less important outputs is maintained, the relative weightings should be set so that one output doesn't erroneously dominate the *Fitness Function*.

Step 4: Selective Reproduction

Once every gene has been given a fitness value, the next step is the formation of an intermediate population. In the original text outlining Genetic Algorithms[78] the intermediate population is formed by calculating the average fitness across the population and using it to normalise all fitness values. The result is a collection of values of the form $f_i/\bar{f}$, where f_i is the fitness of gene i, and $\bar{f}$ is the average fitness for the generation. This normalised value is then proportional to the probability a gene is selected to move into the intermediate population. However, there are many appropriate ways to select genes, for example, the same normalised fitness values could be rounded down to the nearest whole number and have that many copies of themselves placed into the intermediate population. The remainder of every gene's normalised fitness could then be used in the same proportional probability selection as before. For example, a gene with a normalised fitness value of 1.5 would have one copy automatically placed in the intermediate population, with the chance of a second placement being proportional to 0.5.

To form the intermediate population, the Genetic Algorithm used in this work follows two selection criteria. Firstly, any genes that produce an error in the energy minimisation

calculation are discarded, and secondly, any genes with a fitness one standard deviation lower than the previous generations average fitness are discarded. All the remaining genes are carried forward into the intermediate population.

Once the intermediate population has been selected, *Recombination* can occur. *Recombination* is performed by Crossover and Mutation operators, which are the iteration elements of Genetic Algorithms that generate new genes to be tested against the problem. A Crossover operator takes two genes from the intermediate population as an input, and with a probability P_C swaps over each part of their parameter set, as an example consider the two genes defined below:

$$\begin{aligned} G_1 &= [1, 3, 5, 2] \\ G_2 &= [2, 4, 1, 0] \end{aligned} \tag{2.33}$$

where G_i is a gene and $i = 1, 2$, and $[p_1, p_2, p_3, p_4]$ represents a morse potential with parameters p_1, p_2, p_3, p_4. Placing both these genes into a Crossover operator with a swap probability P_C gives:

$$C(G_1, G_2, P_C) = (G_3, G_4) \tag{2.34}$$

where $C(G_1, G_2, P_C)$ is a Crossover operator producing two new genes from G_1 and G_2 by swapping their parameters with probability P_C, and G_3, G_4 are the two new genes resulting from the Crossover operator. As an example if $P_C = 0.5$, G_3 and G_4 might have the following forms:

$$\begin{aligned} G_3 &= [2, 3, 1, 2] \\ G_4 &= [1, 4, 5, 0] \end{aligned} \tag{2.35}$$

where the first and third indexes of the original genes G_1 and G_2 have been swapped. This behaviour is expected as the probability of a swap, $P_C = 0.5$, indicates that on average the Crossover operator should swap two of the gene's parameters. However, this doesn't have to be the case, for example, using the same two genes, G_1, G_2 as before

with $P_C = 0.75$ could give the following:

$$\begin{aligned} G_3 &= [1, 3, 1, 0] \\ G_4 &= [2, 4, 5, 2] \end{aligned} \tag{2.36}$$

where the third and fourth indexes of the original genes G_1 and G_2 have been swapped. This behaviour is still possible, although with a $P_C = 0.75$ on average the Crossover operator should swap three of the four parameters.

After the Crossover operations, the resulting genes go through Mutation operations. Mutation operators take a gene, and with probability P_M, alter each of its parameters by some percentage to produce a new gene. For example, a reasonable range for the percentage change of pair potential's parameters is $\pm 1 - 5\%$. This process is represented mathematically below, following on from one of the results of the Crossover operation in Equation 2.35:

$$M(G_3, P_M) = G_3' = [2.1, 2.97, 1, 2] \tag{2.37}$$

where G_3 is one of the Crossover genes in Equation 2.35, $M(G_3, P_M)$ is a Mutation operator acting on each parameter of G_3 with probability P_M, P_M is the probability of a mutation occurring, and G_3' is the mutated form of G_3. The two operators together comprise the Recombination stage of the Genetic Algorithm process and are used on the intermediate population to produce the next generation. The next generation's population size matches that of previous generations. Once the new generation has been produced the algorithm loops, beginning again at step 2.

For the work in this thesis, $P_C = 0.05$ throughout the entire algorithm, as trial and error showed that larger P_C hindered convergence on a solution. In contrast, P_M was altered as the algorithm progressed, its magnitude following a sinusoidal pattern encased in an exponential envelope set to go to zero at a predefined number of generations. Letting P_M vary in this manner has two effects, firstly, it allows the algorithm to periodically explore a wider search space before honing in on the local optima of that space,

and secondly, it guarantees the algorithm's convergence onto a global minimum of the explored local optima at a set number of generations. Although this method doesn't guarantee convergence on a true global minimum, it is a useful heuristic model that showed good results through trial and error in Chapter 4.

2.1.3 Solid-Liquid Coexistence Method

The solid-liquid coexistence method is a Molecular Dynamics technique for finding the melting point of a structure[80, 81, 82].

Beginning from a single solid crystal in a periodic simulation, a solid-liquid interface is created by zeroing the force interactions and velocity of atoms on one half of the crystal. The atoms in the remaining half of the crystal are superheated until the original crystal structure degenerates into a liquid. In this work, a liquid is defined as a system in which no atom is tied to a bounded region within the system. Once liquified the melted system is brought back into contact with the solid system at a constant temperature and pressure and allowed to equilibrate.

To do this, the frozen half of the system has its force interactions and velocity switched back on, before both halves are run under the same statistical ensemble. Because they had greater energy in the melting stage, atoms in the liquid half of the system can occupy positions that are unphysically close to the solid half at the new temperature and pressure. Therefore, instantaneously bringing the two halves into direct contact produces shock waves as the system responds to the unphysically large force interactions. To avoid these shock waves one of two methods is used:

1. Minimisation calculations, first, on the liquid half of the simulation only, followed by the system as a whole.

2. Spring forces, attached to all the atoms within some distance d of the interface.

The goal of either method is to prevent disturbance of the generated interface. In the first case, the liquid only minimisation allows the liquid atoms to move into positions of

low energy relative to the solid which prevents unphysical forces disturbing the interface on the secondary minimisation. The secondary minimisation allows the whole interface system to form a low energy and therefore stable structure.

In the second case, interface disturbance is prevented by the spring forces, which simultaneously hold the interface in place and damp out the vibrations caused by the shock waves. Spring forces can be released in stages as the vibrations are damped out of the system. Release rate should be proportional to the percentage of unphysical vibrations that have been damped out of the system. Once removed entirely a stable interface remains.

As mentioned above, once the system's interface has been stabilised, the whole system is equilibrated at a given temperature and pressure. The evolution of the system during this equilibration phase indicates whether the temperature is above, below, or at the melting temperature for the selected pressure.

If the temperature, T, is above the melting temperature: $T > T_M$, the interface of the system will move into the solid phase and the liquid phase will grow. If $T < T_M$ the liquid phase will remain the same size but freeze into a glass like amorphous state, leaving the interface completely fixed. If $T = T_M + \triangle t$ for $\triangle t \to 0$, both phases will remain in their previous states and the interface will demonstrate no net movement into either phase. Figure 18 shows these three cases visually, along with the system's interface directly after stabilisation.

Visual inspection can be used to establish the state of the system. In the cases where such inspection would be time prohibitive, a radial distribution function can be used to measure the density of atoms at a distance d from a central atom. Density is calculated by finding the number of points in a spherical shell of thickness Δd, a distance d from a central atom, and dividing this number by the shell's volume - giving a function of the following form:

$$g(d) = \frac{N}{\frac{4}{3}\pi\left((d+\Delta d)^3 - (d)^3\right)} \tag{2.38}$$

where $g(d)$ is the radial distribution about some atom, N is the number of atoms found

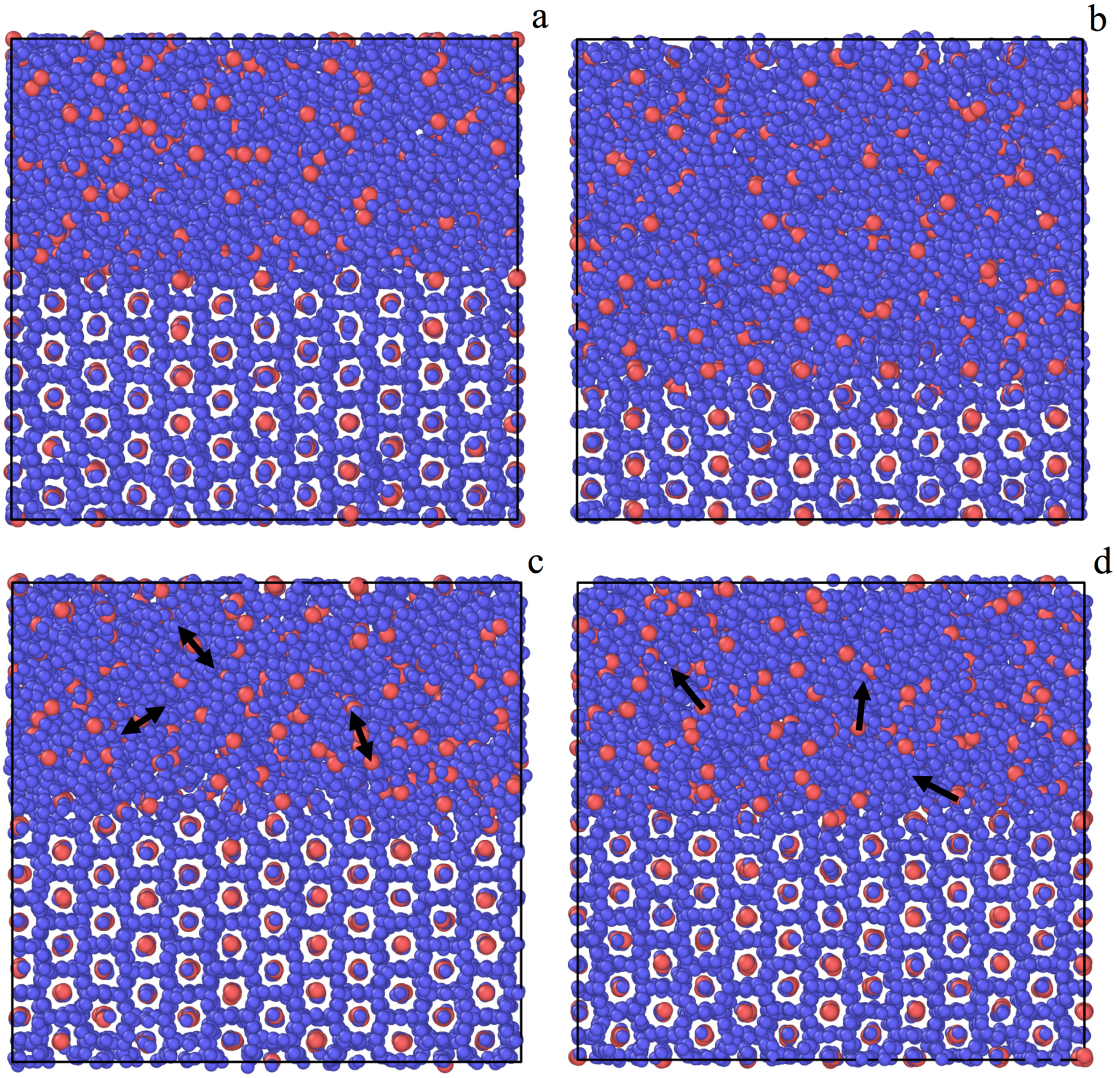

Figure 18: Various states of a system in a solid-liquid coexistence simulation, showing: a) A system directly after the interface has been stabilised, b) Movement of a system's interface into the solid phase, indicating $T > T_M$, c) Stable interface between a crystalline solid and amorphous glass solid, arrows show atoms are bounded to specific regions, indicating $T < T_M$, d) Stable interface between crystalline solid and liquid, arrows show atoms are not bounded to specific regions, $T = T_M + \triangle t$ for $\triangle t \to 0$.

at distance d, and Δd is the thickness of the shell. Ordered crystal structures have very distinct radial distribution functions, whilst liquids have slightly less distinct but characteristic distributions. By measuring each atom's order parameter at consecutive time intervals, the movement of the interface can be quantified over time.

2.2 Structural Optimisation

Structural optimisation is a collection of static lattice methods which optimise the atomic positions of a given input lattice. Using pair potentials and potential energy calculations, the methods can calculate cohesive energy and use it as a figure of merit for the lattice. Cohesive energy represents the energy required to completely separate the atoms that compose a lattice into a vapour. Therefore, lattice's that have negative cohesive energies represent atomic arrangements that are energetically preferable to the same atoms in a vapour state. For arrangements of the same group of atoms, the arrangement with the lowest (most negative) cohesive energy is the most stable and therefore most probable structure. Lattice's that have a positive cohesive energy are completely unstable and will either not form or spontaneously degenerate into the vapour state/ a Lattice structure with a negative cohesive energy. Using cohesive energy as a metric allows for the creation of a potential energy surface which represents all the possible configurations of atoms in the lattice. On this surface a local minimum or maximum corresponds to the most preferable or least preferable set of atomic positions in the locality of interest.

With a link established between atomic positions and cohesive energy, structural optimisation can be defined as the search for a local energy minimum. As the energy search finds a local minimum, the configurations searched in atomic position space must also be local and thus are unlikely to deviate significantly from the original lattice. Therefore, structural optimisation methods are lattice preserving and find the lowest possible energy for a given lattice with the minimal possible structural change. Figure 19 gives an example of structural change that preserves structure.

One of the predominant software packages used in academia to perform these calculations is the General Utility Lattice Program (GULP)[83, 84]. This is the software package used throughout this work and therefore will be the focus of this section.

The default GULP optimiser uses a form of Newton-Raphson method, known as the Quasi-Newton method given in the following paper by Shanno[85]. The method is used throughout this thesis, and its derivation and explanation is given below.

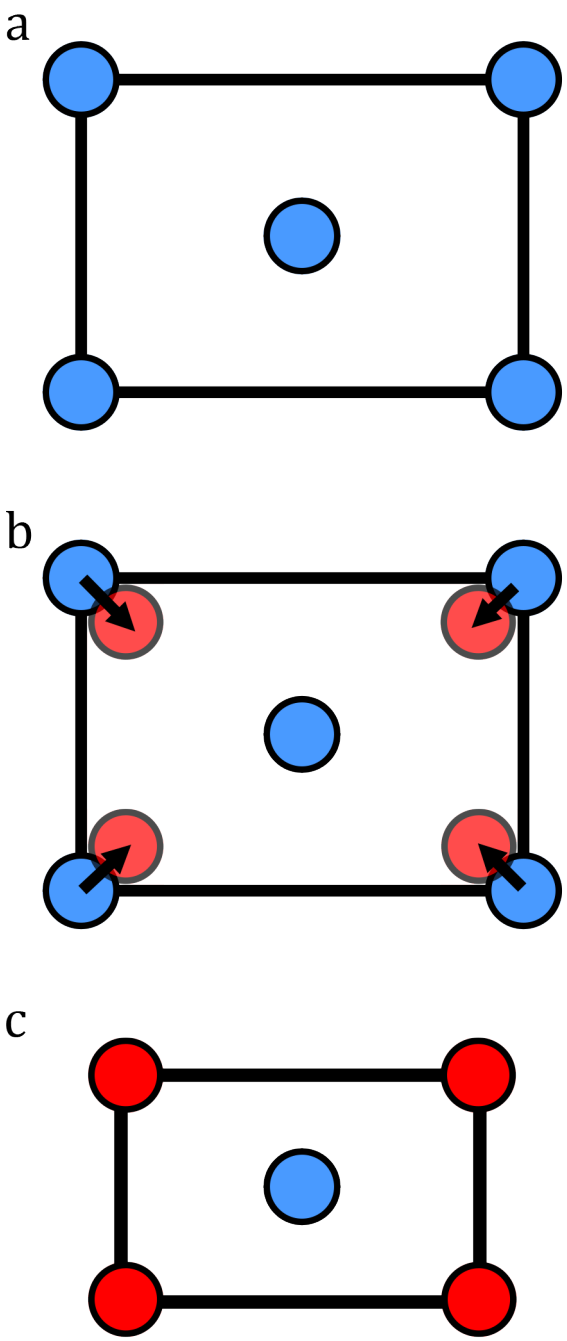

Figure 19: Illustration of the optimisation process for a 2D lattice. a) Shows a 2D lattice input, where blue circles represent atoms and black lines represent the lattice boundary, b) Shows an example of atomic movement that minimises the cohesive energy of the structure, where the atomic movement is shown by the black arrows and red atoms are the new atomic positions, c) The final optimised structure, where red circles represent atoms that moved during optimisation and the single blue atom represents an atom that remained in the same position during the minimisation.

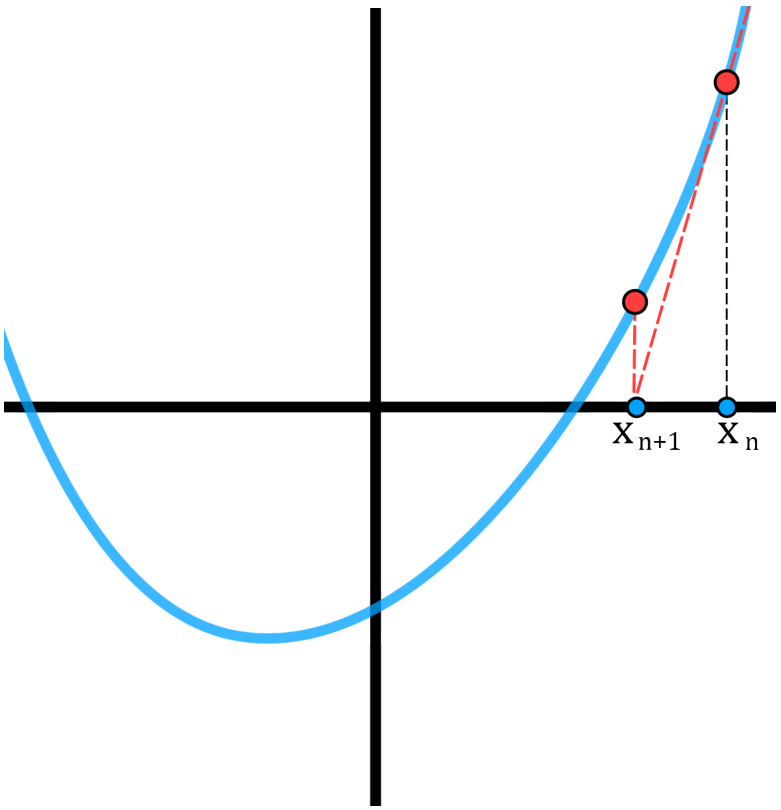

Figure 20: Geometric visualisation of the Newton-Raphson algorithm and how it converges to some root of a function $f(x)$.

2.2.1 Newton-Raphson

The Basic Idea

Newton-Raphson methods iteratively produce closer and closer approximations to a root of a function, $f(x)$, using an equation of the form:

$$x_{n+1} = x_n - \frac{f(x_n)}{f'(x_n)} \tag{2.39}$$

where x_n is the method's nth approximation of the root of $f(x)$, x_{n+1} is the method's $n+1$th approximation of the root of $f(x)$, $f(x_n)$ is the value of $f(x)$ at x_n, and $f'(x_n)$ is the value of the first derivative of $f(x)$ at x_n. This equation is based on a method for finding the root of function, $f(x)$, by taking its tangent at a point x_n, calculating the tangent's x intercept, and using that as the value of x_{n+1}. The process is shown visually in Figure 20. Given a point on the line $(x_1, f(x_1))$ its tangent can be found by using the point slope equation:

$$f(x) - f(x_1) = f'(x_1)(x - x_1) \tag{2.40}$$

Setting $x_1 = x_n$, and $f(x) = y$ gives the following:

$$y - f(x_n) = f'(x_n)(x - x_n) \tag{2.41}$$

$$y = f'(x_n)(x - x_n) + f(x_n) \tag{2.42}$$

To get the root of this tangent line, y is set to 0 and the equation is rearranged:

$$f'(x_n)(x - x_n) + f(x_n) = 0 \tag{2.43}$$

$$f'(x_n)(x - x_n) = -f(x_n) \tag{2.44}$$

$$x - x_n = -\frac{f(x_n)}{f'(x_n)} \tag{2.45}$$

$$x = x_n - \frac{f(x_n)}{f'(x_n)} \tag{2.46}$$

The calculated root x is the next approximation, so setting $x_{n+1} = x$ gives us Equation 2.39 above. This can be extended to find a minimum or maximum point of a twice differentiable function by finding the roots of its gradient $g(x) = f'(x)$. This changes Equation 2.39 to the modified form:

$$x_{n+1} = x_n - \frac{g(x_n)}{g'(x_n)} = x_n - \frac{f'(x_n)}{f''(x_n)} \tag{2.47}$$

Derivation from Taylor Series in 1D

A function relating atomic positions to energy is an example of an unconstrained, convex function. Unconstrained because there are no constraints on the atomic positions, and convex because the function's initial parameters, the atomic positions, situate the function around a local minimum. This kind of function is known as a special function and is amenable to the Newton-Raphson method[86]. The function, f, is a multi-variable, scalar valued function, which accepts every atom's position coordinates as arguments and returns a single cohesive energy value. Deriving the Newton-Raphson method for a multivariable function requires a different approach using Taylor series. This approach

will be outlined here, starting from the derivation in 1D which begins with the following definition for the Newton-Raphson equation:

$$x_{n+1} = x_n + \Delta x \tag{2.48}$$

where Δx is the change required to make x_n a root of $f(x)$, x_n is the nth approximation for a root of $f(x)$, and x_{n+1} is the n+1th approximation for a root of $f(x)$. To find Δx we take the Taylor series expansion of the function $f(x_n + \Delta x)$ about x_n:

$$\begin{aligned} f(x_n + \Delta x) &= f(x_n) + f'(x_n)((x_n + \Delta x) - x_n) + ... \\ &= f(x_n) + f'(x_n)\Delta x + ... \end{aligned} \tag{2.49}$$

by definition Δx brings x_n to a root of $f(x)$ so the left hand side of Equation 2.49 can be set to zero. Rearranging the equation so that zero appears on the right hand side for notation's sake gives:

$$f(x_n) + f'(x_n)\Delta x + ... = 0 \tag{2.50}$$

Assuming the initial guess was close to the root, the terms can be truncated at the first order and the following equation can be used to find an approximation of the Δx required to reach a root of $f(x)$:

$$f(x_n) + f'(x_n)\Delta x \approx 0 \tag{2.51}$$

Rearranging this gives the following:

$$\Delta x \approx -\frac{f(x_n)}{f'(x_n)} \tag{2.52}$$

Subbing this approximate value for Δx back into Equation 2.48 reproduces Equation 2.39:

$$x_{n+1} = x_n - \frac{f(x_n)}{f'(x_n)} \tag{2.53}$$

Multivariable Newton-Raphson

Extending this to a multivariable function, $f(\boldsymbol{x})$, where f is a scalar valued function, $\boldsymbol{x}$ is a vector in $\mathbb{R}^N$, and N is the equal to the total number of atomic position coordinates, Equation 2.48 can be redefined to give:

$$\boldsymbol{x}_{n+1} = \boldsymbol{x}_n + \Delta\boldsymbol{x} \tag{2.54}$$

where $\boldsymbol{x}_{n+1}$, $\boldsymbol{x}_n$, and $\Delta\boldsymbol{x}$ are all vectors in $\mathbb{R}^N$ that reside within function f's parameter space. Using a similar process to that outlined in the 1D case, $\Delta\boldsymbol{x}$ becomes:

$$\Delta\boldsymbol{x} \approx \frac{f(\boldsymbol{x}_n)}{f'(\boldsymbol{x}_n)} = \frac{f(\boldsymbol{x}_n)}{\boldsymbol{\nabla} f(\boldsymbol{x}_n)} \tag{2.55}$$

where $\boldsymbol{\nabla} f(\boldsymbol{x}_n) = f'(\boldsymbol{x}_n) = g(\boldsymbol{x})$ and is the gradient of $f(\boldsymbol{x})$. To find the minimum and maximum points of a function, $\Delta\boldsymbol{x}$ from Equation 2.47 for finding the points in 1D becomes the following:

$$\Delta\boldsymbol{x} = -\mathbf{H}^{-1} g(\boldsymbol{x}) \tag{2.56}$$

where $\mathbf{H}$ is the Hessian of the function $f(\boldsymbol{x})$, the multivariable equivalent of $f''(x_n)$ in Equation 2.47, and $g(\boldsymbol{x})$ is the gradient of $f(\boldsymbol{x})$ the multivariable equivalent of $f'(x_n)$. The two are defined as follows:

$$\mathbf{H} = \begin{bmatrix} \frac{\partial^2 f}{\partial x_1^2} & \frac{\partial^2 f}{\partial x_1 \partial x_2} & \cdots & \frac{\partial^2 f}{\partial x_1 \partial x_n} \\ \frac{\partial^2 f}{\partial x_2 \partial x_1} & \frac{\partial^2 f}{\partial x_2^2} & \cdots & \frac{\partial^2 f}{\partial x_2 \partial x_n} \\ \vdots & \vdots & \ddots & \vdots \\ \frac{\partial^2 f}{\partial x_n \partial x_1} & \frac{\partial^2 f}{\partial x_n \partial x_2} & \cdots & \frac{\partial^2 f}{\partial x_n^2} \end{bmatrix} \tag{2.57}$$

$$\boldsymbol{g} = \boldsymbol{\nabla} f(\boldsymbol{x}) = \left[\frac{\partial f}{\partial x_1}, \frac{\partial f}{\partial x_2}, \ldots, \frac{\partial f}{\partial x_n} \right] \tag{2.58}$$

where the Hessian $\mathbf{H}$ is a matrix of all the possible second partial derivatives of $f(\boldsymbol{x})$, and the gradient $g(\boldsymbol{x})$ is a vector of all the possible first partial derivatives of $f(\boldsymbol{x})$.

To turn this into an iterative algorithm, Shanno gives the following[85]:

$$\boldsymbol{x}_{n+1} = \boldsymbol{x}_n - s_n \mathbf{H}_n^{-1} g(\boldsymbol{x})_n \tag{2.59}$$

where s_n is a scalar chosen at each step to minimise $f(\boldsymbol{x}_{n+1})$ in the direction of $-\mathbf{H}_n^{-1} g(\boldsymbol{x})_n$, $\mathbf{H}_n^{-1}$ is the inverse Hessian at the nth approximation, and $g(\boldsymbol{x})_n$ is the gradient at the nth approximation. Iteratively solving this moves $\boldsymbol{x}$ towards a local minimum of $f(\boldsymbol{x})$.

Quasi-Newton Methods

Because of the computational cost of calculating the exact inverse Hessian at every step, methods have been developed which use an approximate inverse Hessian in its place, and update it as the algorithm progresses. Because they don't use the exact Hessian, these methods are known as "Quasi-Newton". There are two main update schemes that are generally employed Davidon–Fletcher–Powell (DFP) [87] and Broyden–Fletcher–Goldfarb– Shanno (BFGS) [85], of the two BFGS converges on solutions faster and is the most computationally efficient.

Both methods begin with either the exact inverse Hessian, or some other positive definite matrix, often the unit matrix. This matrix is then updated as the algorithm progresses. Positive definiteness is a necessary condition, as the Hessian must approximate a well shape for which it is possible to find a minimum.

The advantage of a Quasi-Newton method, is that it can use the curvature of the energy space to converge to a solution faster, without the computational overhead of calculating the inverse Hessian at every iteration.

The method's initial point must be chosen carefully[88], as it's possible that the algorithm will converge to some other critical point, such as a saddle, if the local potential energy surface isn't a well. Fortunately this isn't a problem for structural optimisations, as the initial atomic positions provided to the algorithm are based on known crystal

structures. Therefore, as long as the potentials are a good approximation of the atomic interactions, the system is by definition within a local potential energy well, as a stable crystal system is an example of a real world local potential energy well.

Implementation of the Algorithm in GULP

To implement the algorithm it's necessary to consider: A) when the updated inverse Hessian has drifted too far from the real inverse Hessian, and B) when the algorithm has reached an appropriate minimum.

In the first case, although the methodology updates the inverse Hessian, the approximation can become further from the real Hessian over successive time steps through compounding error or the inability to predict significant changes in the function's local curvature. If the approximation drifts too far from reality, and no longer accurately represents the function's local curvature, it must be recalculated to prevent the algorithm using erroneous gradients and converging to an incorrect point. In the General Utility Lattice Program(GULP) Hessian recalculation is triggered by one of the following events[84]:

1. The maximum number of iterative cycles between exact inverse Hessian computations is exceeded (user defined).
2. The angle between the gradient vector calculated for the current step and its search direction vector $\Delta \boldsymbol{x}$ exceeds some user defined value.
3. The energy drops by more than some user defined value in one iteration of the minimisation cycle, indicating a change to the local curvature of the function.
4. Line minimisation along the current search vector $\Delta \boldsymbol{x}$ does not minimise $f(\boldsymbol{x})$. This equates to no value of s_n in Equation 2.59 being able to decrease the value of $f(\boldsymbol{x})$.

Apart from the final condition, these conditions are user defined and must be chosen carefully to avoid an erroneous convergence.

In the second case, GULP's stopping point for the algorithm is given by one of following conditions:

1. The gradient norm of the function calculated at iteration n is below some user defined value.
2. The maximum component of the function's gradient is below some user defined value.
3. The estimated displacement vector norm is below some user defined value.
4. The change in energy between successive iterations falls below some user defined value.
5. The change in the variables contained in $\boldsymbol{x}$ falls below some user defined value between successive iterations.

All of these conditions are user defined. It is therefore up to the user to decide at what point they consider the system sufficiently converged. Good stopping conditions prevent the optimisation ending prematurely or continuing indefinitely.

2.3 Boltzmann Factors

Boltzmann factors are a useful tool from statistical mechanics that can be used to compare the probabilities of two microstates in a system without knowing the systems partition function Z. They have been used extensively in this thesis to compare the probability of different structural configurations.

They are derived from the Canonical ensemble, and measure the probability of a microstate of energy ϵ at temperature T[89]. The Boltzmann factor for a single microstate is:

$$p_s(\epsilon_s) \propto \exp\left(-\frac{\epsilon_s}{k_B T}\right) \tag{2.60}$$

where $p_s(\epsilon_s)$ is the probability of a microstate s with energy ϵ_s, k_B is the Boltzmann constant, and T is the temperature. The exact probability of a state can be found by normalising it by the system's canonical partition function Z:

$$p_s(\epsilon_s) = \frac{\exp\left(-\frac{\epsilon_s}{k_B T}\right)}{Z} \tag{2.61}$$

where Z is given by:

$$Z = \sum_{i=1}^{N} p_i = \sum_{i=1}^{N} \exp\left(-\frac{\epsilon_i}{k_B T}\right) \tag{2.62}$$

where p_i is the probability associated with microstate i, ϵ_i is the energy of microstate i, and N is the number of accessible microstates. Therefore, Z is the summation of every possible microstate i's probability. This makes it a constant of the system which can be factored out when taking the ratio of two states:

$$\frac{p_i}{p_j} = \left(\frac{\exp\left(-\frac{\epsilon_i}{k_B T}\right)}{Z}\right)\left(\frac{Z}{\exp\left(-\frac{\epsilon_j}{k_B T}\right)}\right) \tag{2.63}$$

$$= \frac{\exp\left(-\frac{\epsilon_i}{k_B T}\right)}{\exp\left(-\frac{\epsilon_j}{k_B T}\right)} \tag{2.64}$$

$$= \exp\left(\frac{\epsilon_j - \epsilon_i}{k_B T}\right) \tag{2.65}$$

where p_i, p_j are the probabilities of microstates i, j respectively, ϵ_i, ϵ_j are the energies of microstates i, j respectively, k_B is the Boltzmann constant, and T is the temperature. Calculating these ratios makes it possible to decide on the most likely microstate out of a subset of all those available to the system. The next section details an application of these comparisons, which was developed for work in this thesis.

2.3.1 Cascading Probabilities

This method stems from work performed for this thesis, which was published in IEEE Transactions on Magnetics[1, 2], that established the most probable substitution positions of titanium in RT_{12} structures through substitution permutation and structural

optimisation. The method is based on the following idea, for M substitution positions, and m substitutions the number of possible substitution configurations is:

$$C_m(M) = \frac{M!}{m!(M-m)!} \tag{2.66}$$

where $C_m(M)$ represents the number of possible substitution configurations in the crystal lattice. To compare the probability of the different configurations, the probability of each configuration's minimum energy microstate is used as a proxy for its probability as a whole. This adds the assumption that the probability of a configuration's minimum energy microstate is representative of its probability as a whole. Based on the structural optimisation algorithm's requirement of a well like potential energy surface near the minimum energy point, it is reasonable to accept this assumption.

For a small system it's possible to calculate every possible configuration of substitutions, but as system size increases this becomes computationally prohibitive. Although doing so can unambiguously provide the globally optimal substitution configuration, for any system of a reasonable size the computational effort is impractical. Therefore, it is preferable to avoid this computational effort by applying an algorithm that narrows the choice of configurations to a practical number. Cascading Probabilities achieves this by making some assumptions about how substitutions enter the crystal lattice.

The first assumption is that every substitution is discrete, which means that each substitution enters the crystal on a separate occasion. Making this assumption allows substitution events to be modelled as stages. The second assumption is that the time between substitutions is sufficient for each substitution to occupy the minimum energy position. Making this assumption provides a selection criteria that can be used to select the most probable configuration at each stage. The final assumption is that once substitutions have occurred they do not change from one stage to the next. Making this assumption means that the minimum energy configuration of the preceding stage informs the available configurations of the stage directly after it.

Taken together these assumptions provide a framework for permutating substitutions

into the crystal. To illustrate this, consider the following example, at stage one of the algorithm the crystal has M available positions which are substituted in turn, providing M possible configurations. Structural optimisation is performed on each of the M configurations and the minimum energy configuration for a single substitution is found - the substitution's position in this configuration is the minimum energy position. This configuration is passed on to the second stage of the algorithm. Because the first substitution cannot switch position, the second substitution only has $M-1$ available positions, resulting in $M-1$ configurations for the two substitutions. Compared to the number of possible configurations given in Equation 2.66 for $m=2$, this is already a significant reduction of complexity.

Making these assumptions limits the investigated configurations to those which follow a substitution path of greatest energetic favourability. As energetic favourability is tied to probability, this method can be defined as a selection criteria that follows the most probable substitution pathway.

Because structural optimisation is performed on every configuration in a stage, the minimised energy of all a stage's configurations are known. This means Equation 2.60 can be used to get a Boltzmann factor for every configuration. Summing these Boltzmann factors gives the following:

$$P_S = \sum_{i=1}^{M} p_i \tag{2.67}$$

where P_S is the summed probability of all the Boltzmann factors (p_i) associated with the stage's configurations, M is the number of configurations associated with the stage, and p_i is the relative Boltzmann factor of configuration i. Normalising the Boltzmann factors of every configuration in the stage with Equation 2.67 produces their relative probability of being selected at that stage:

$$p_{i,R} = \frac{p_i}{P_S} \tag{2.68}$$

where $p_{i,R}$ is the relative probability of configuration i. Using this as a measure, the probability of a particular substitution pathway can be calculated by compounding the

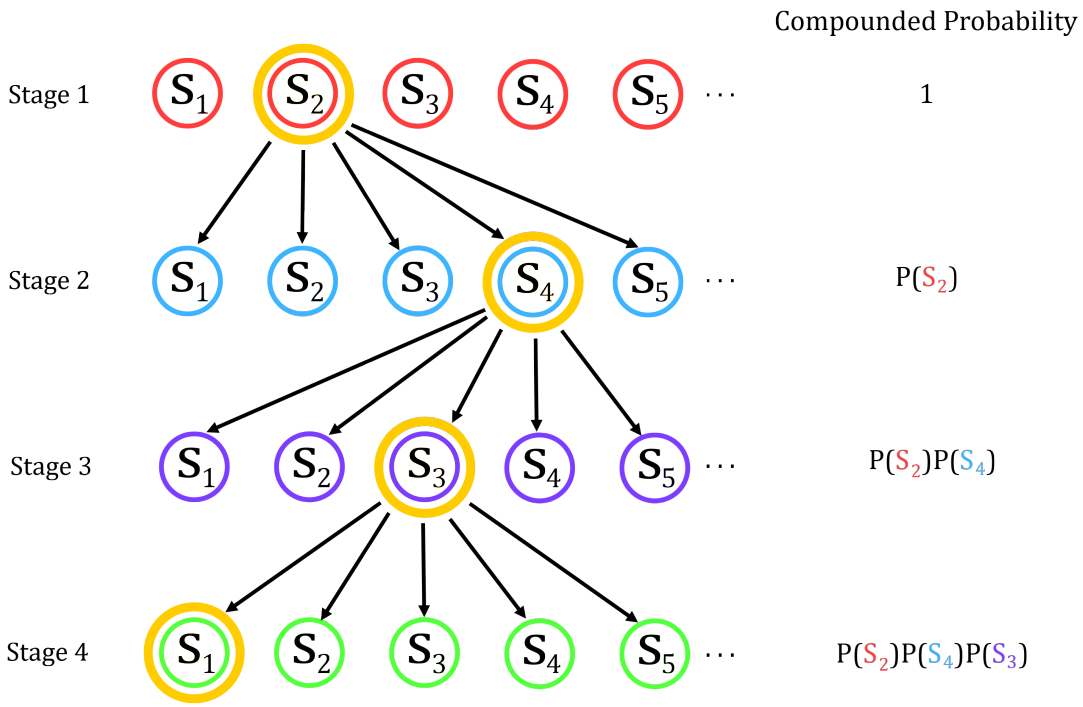

Figure 21: Simple visualisation of the how the probability compounds at each stage. S_1, S_2 etc. represent the stage's configuration microstates, where each colour corresponds to a different stage. Large yellow circles indicate the chosen minimum energy microstate for a stage and arrows represent this configurational microstate being carried forward into the next stage. The column of compounded probability shows the pathway's probability, W_P (from Equation 2.69), up to that stage. $P(S_x)$ is the probability of microstate x at the relevant stage. The probabilities are ordered by their stage, left to right, with lower stages on the left.

relative probability of the chosen configuration at each stage:

$$W_P = \prod_{j=1}^{m} p_j \tag{2.69}$$

where W_P is the probability of pathway P, m is the number of substitutions along pathway P, j is the substitution stage, and p_j is the relative probability of the chosen configuration at stage j.

Figure 21 shows this process visually, as can be seen, in the first stage, each configuration (S_1, S_2, S_3, ..., S_M) is structurally optimised and the minimum energy configuration, S_2, is selected to move forward to the next stage. At this initial stage the compounded probability of the pathway is one, as the relative probability of stage zero (no substitutions) is one. Stage two carries the probability of the first stage, $P(S_2)$, forward making

the compounded probability of the substitution pathway $P(S_2)$ at this stage. As the figure shows, this process continues and probability of each stage's configuration cascades down the pathway. This process is what gives the algorithm its name.

Although not shown on Figure 21, due to crystal symmetry, at many stages there are multiple minimum energy positions. This means that there are many possible substitution pathways, W_P, through the structure. Summing the probability of these pathways provides a measure of the selection criteria's ability to capture the most probable substitution configurations:

$$T_P = \sum_{i=1}^{A} W_i \tag{2.70}$$

where T_P is the Total Configurational Probability and is the summation of each path W_i's probability, A (for 'All') is the total number of substitution pathways, and W_i is the compounded probability for substitution pathway i. A high value of T_P indicates the selection criteria has a good coverage of the probable substitution configurations, with the maximum possible value being one - typically this is only seen for a very predictable structure at low temperature. A low value of T_P indicates that the selection criteria has poor coverage of the probable substitution configurations with a minimum value of zero - this value can only be reached when using a very poor selection criteria at low temperature.

Beyond measuring the configurational coverage of a selection criteria, T_P has another use as a measure of the predictability of a structure. For the standard choice of selection criteria: minimum energy, high values of T_P indicate that substitutions in the structure have high predictability, and low values of T_P indicate that substitutions in the structure have low predictability. Further, as T_P is based on Boltzmann factors, which are dependent on temperature, T_P is temperature dependent, making it possible to assess structural predictability with temperature. T_P is used in Chapter 3 of this thesis to assess the applicability of selection criteria and to analyse structural predictability with temperature.

If required, the selection criteria can be narrowed or broadened to suit the problem

at hand. In some cases, for example selection criteria validation, it can be swapped for a different metric e.g. maximum energy. Because of this, when this method is used in this work, the specific selection criteria is outlined.

3 Site Preference and Structural Effects of Titanium Substitution in $SmFe_{12}$, $SmCo_{12}$ and $NdFe_{12}$

3.1 Introduction

Permanent magnetic materials are necessary for the continuation of the modern world, and are used in everything from cars to computers. In cars they find their main use in electrical engines, which require very powerful permanent magnets if they are to be maximally efficient. The most powerful permanent magnets have the crystal structure $Nd_2Fe_{14}B$, first discovered by Sagawa et al.[42]. Whilst impressive they are limited by their low curie temperature and require the addition of dysprosium[90], to give $(Nd,Dy)_2Fe_{14}B$, if they are being used in high temperature applications. Dysprosium addition degrades magnetic properties by aligning anti-parallel to the general spin direction, whilst also adding significant cost to the structures base materials. Couple this with the scarcity of both Rare-Earth elements and the fact that most of the rare-earth material supply chain is focused in China[91], and the case for new materials composed of less critical elements becomes clear.

Numerous nations and organisations around the world are seeking new materials, and through the collaboration of a number of them in Japan the "Technology Research Association of Magnetic Materials for High Performance Motors" (MagHEM)[5] was formed, with a stated aim of developing:

> *"... innovative high-performance magnets without rare-earth materials which exceeds current magnets with rare-earth materials in performance, high-efficiency soft magnetic materials (Iron core) for internal loss reduction, and compact high-efficiency motors."*

One of the stated aims of the project is to produce magnetic materials that rival $(Nd,Dy)_2Fe_{14}B$ but contain reduced or no rare-earth materials. Currently, there are no discovered or proposed rare-earth free magnetic materials with a similar performance

to $(Nd,Dy)_2Fe_{14}B$, a fact which has lead the MagHEM consortium to focus on improving the current market leading magnets $Nd_2Fe_{14}B$, and on developing new rare-earth based magnets which exceed it. The work presented in this chapter is focused on the latter goal.

In collaboration with MagHEM and the Toyota Motor Corporation, this work investigated the phase stabilisation of a previously unstable set of crystal structures forming in the $ThMn_{12}$ type structure. Their discovery was fueled by the excitement surrounding $Nd_2Fe_{14}B$ in the 1980s, which was preceded by $SmCo_5$ another rare-earth containing compound. Numerous research groups at the time were attempting to create new high performance ternary structures by using composition ranges based on $Nd_2Fe_{14}B$, and working with rare-earths, transition metals, and tertiary dopants. One set of structures that arose from this were the $ThMn_{12}$ structural types, with a generic chemical formula of $RT_{12-x}M_x$, where R $\equiv$ (Nd, Sm, Gd, Tb, Dy, Ho, Er, Tm, Lu, Y), T $\equiv$ (Fe, Co)[92], and M $\equiv$ (Si, Ti, V, Cr, Mo, W)[47]. The primary work undertaken on these structures was performed by D. Mooij and Buschow[92, 47], but as the $ThMn_{12}$ compounds proved harder to stabilise than $Nd_2Fe_{14}B$ they faded into the background. D. Mooij and Buschow focused on $RFe_{12-x}M_x$ type structures, as the large magnetic moment of the iron atoms makes them suitable for magnetic applications. During their work, they noted that of the possible M substitutional elements, titanium (Ti) and tungsten (W) could form ternary structures with the lowest atom content, an important property for minimising magnetic degradation.

Although interest waned for some decades after their initial discovery, the study of the structures was given new impetus by a paper from Miyake et al.[49], which studied the magnetic properties of $NdFe_{12}$, $NdFe_{11}Ti$, and $NdFe_{11}TiN$ from first principles. In this paper they found that reduction of the ternary M element, in this case Ti, could improve the magnetic properties of the structure. Following on from this paper, Hiriyama et al. grew $NdFe_{12}$, $NdFe_{12}N$, and $Sm(Fe_{0.8}Co_{0.2})_{12}$ epitaxially via sputtering[50, 51]. Analysing their magnetic properties they found that the $NdFe_{12}N$ thin film had superior magnetic properties to $Nd_2Fe_{14}B$, with values of $\mu_0 M_s \approx 1.78\mathrm{T}$, $\mu_0 H_a \approx 8\mathrm{T}$, and $T_C \approx 823\mathrm{K}$,

and that the $Sm(Fe_{0.8}Co_{0.2})_{12}$ thin film had superior magnetic properties also, with values of $\mu_0 M_s = 1.78\mathrm{T}$, $\mu_0 H_a = 12\mathrm{T}$, and $T_C = 859\mathrm{K}$, all higher or roughly the same as $Nd_2Fe_{14}B$'s values of $\mu_0 M_s \approx 1.61\mathrm{T}$, $\mu_0 H_a \approx 8.7\mathrm{T}$, and $T_C \approx 586\mathrm{K}$.

In the case of $NdFe_{12}N$, it was deemed impossible to effectively manufacture the material through common hot press sintering methods, as the structure decomposes at 873K. However, due to its reduced requirement for rare-earth elements it is still considered a cost effective replacement for $Nd_2Fe_{14}B$ by MagHEM, along with $SmFe_{12-x}Ti_x$, $SmCo_{12-x}Ti_x$, and $NdFe_{12-x}Ti_x$. This chapter focuses on the latter three compounds, the structural and energetic effects of titanium substitution and how this affects stability and cohesive energy, substitutional site preference, energy density, and the stability region of the ternary structures.

3.2 Study Resources

The Morse potentials used in this work were derived from cohesive energy curves of the three materials. Ab initio calculations provided the cohesive energy data and Chen's inversion Lattice technique[93] was used to fit each Morse potential. The shape of all the potentials for neodymium and samarium interactions can be seen in Figure 22. The constants of all the potentials used can be seen in Table 1, see Equation 2.8 for the potential definition.

To analyse the energetic and structural changes, the GULP simulation software package's structural optimisation methods[84], discussed in Chapter 2, were used, along with the Cascading Probabilities method for Titanium substitution site selection.

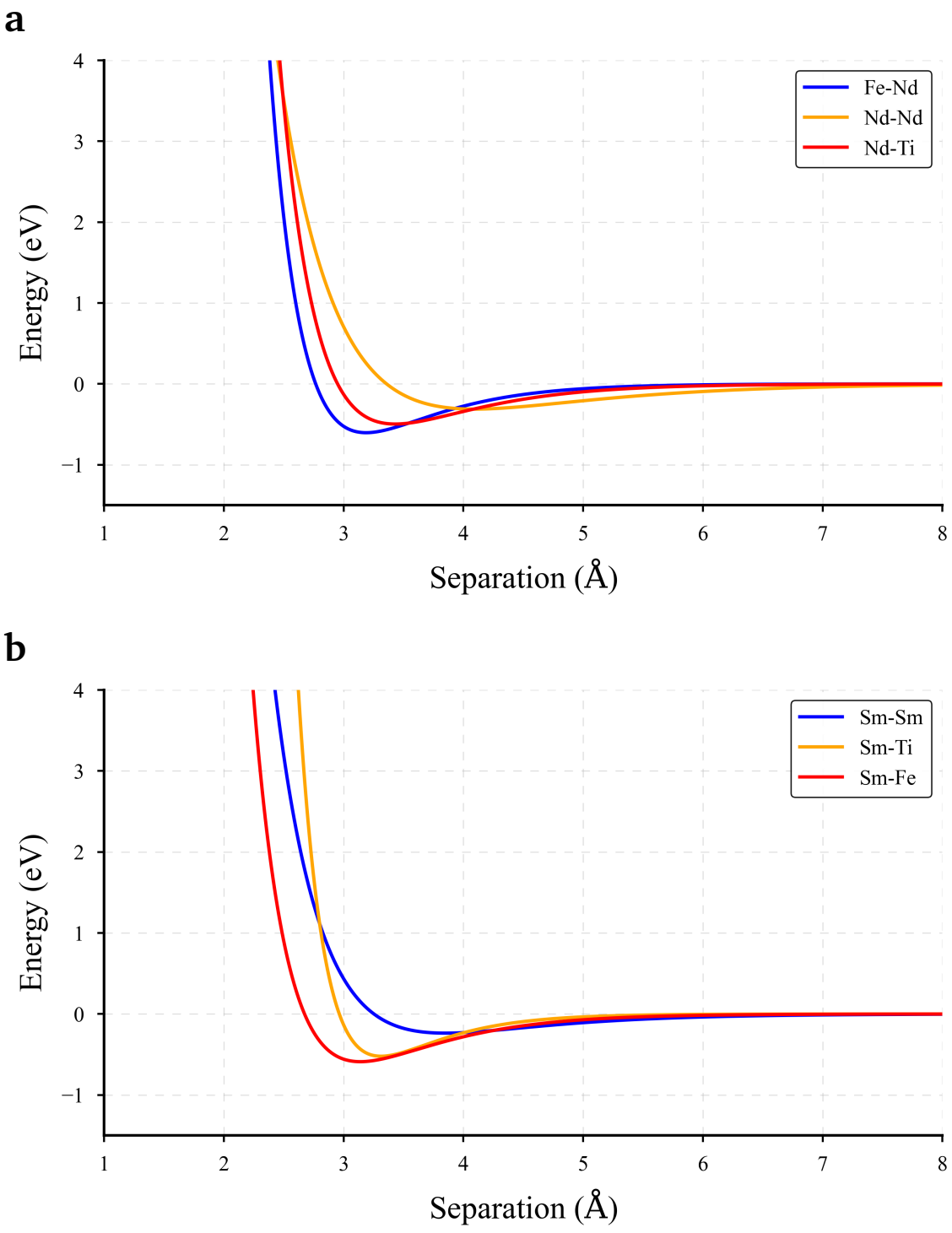

Figure 22: Rare-earth Morse potentials used during the structural optimisations, showing a) neodymium, and b) samarium.

Atom Pair	D_0 (eV)	α (1/Å)	r_0 (Å)	Cut Off (Å)
Fe-Fe	0.764	1.5995	2.7361	12
Fe-Ti	0.8162	1.448	2.914	12
Fe-Nd	0.6036	1.6458	3.188	12
Nd-Nd	0.312	0.945	4.092	12
Nd-Ti	0.4964	1.440118	3.4309	12
Ti-Ti	0.6540	1.2118	3.3476	12
Sm-Sm	0.2365	1.16433	3.8485	12
Sm-Ti	0.5219	1.98644	3.3129	12
Sm-Fe	0.5891	1.48848	3.1394	12
Sm-Co	0.5686	1.47399	3.1725	12
Ti-Co	0.7527	1.40291	2.9331	12
Co-Co	0.6774	1.64306	2.7093	12

Table 1: Table of all values used for the Morse potentials in the following study.

3.3 Method Validation

Potentials

All the potentials used in this work, see Table 1, were validated by structural optimisation calculations of known crystal structures that produced lattice parameters and titanium site preferences that could be compared to values from the literature.

Structural optimisation was performed for $SmFe_{11}Ti$, $NdFe_{11}Ti$, and $SmCo_{11}Ti$. The calculated lattice parameters were in agreement with lattice parameters from the literature[48, 94] to within $<2\%$, see Table 2 for a detailed comparison.

To examine the site preferences, structural optimisation calculations for each single substitution configuration were performed, which showed titanium had the expected site preference, set out by De Mooij and Buschow in 1988[47]. De Mooij and Buschow showed there are three symmetry related Wyckoff position subsets in the RT_{12} structure: 8i, 8j, and 8f with a preferability order of: 8i $\rightarrow$ 8j $\rightarrow$ 8f. Figure 23 demonstrates this preference by plotting the relative probability of each position's configuration.

	Calculated		Expected		% Difference	
Structure	a (Å)	c (Å)	a (Å)	c (Å)	a (%)	c (%)
$NdFe_{11}Ti$	8.554	4.853	8.574*	4.907*	+0.23	+1.10
$SmFe_{11}Ti$	8.488	4.814	8.557*	4.800*	+0.81	-0.29
$SmCo_{11}Ti$	8.510	4.821	8.426†	4.741†	-1.00	-1.69

Table 2: Table of calculated and expected lattice constants, values annotated with $*$ are from [48], values annotated with † are from [94].

As can be seen in Figure 23, there is a significant bias for configurations with a substitution in an 8i position, as is expected from the literature. The exact probability ratios are P(8j)/P(8i) $\approx 10^{-19}$, P(8f)/P(8i) $\approx 10^{-32}$, and P(8f)/P(8j) $\approx 10^{-13}$ at 300K. Due to symmetry, the probability of each of the subset's configurations is identical.

Correct site preference is an important metric, as it demonstrates the potential's ability to choose realistic structures using structural optimisation. This indicates that despite any inaccuracy between the calculated cohesive energy and the true cohesive energy, the ratio between the different positions should be accurate, as any error in calculation is systematic and affects all calculations.

Selection Criteria

This chapter is based on the results of two separate studies which used different selection criteria and therefore have different validation methods. Both studies used supercells to model low percentage titanium substitution.

The first study used 2×2×1 supercells, where A×B×C represents: A unit cell repeats in the $\boldsymbol{a}$ lattice direction, B unit cell repeats in the $\boldsymbol{b}$ lattice direction, and C unit cell repeats in the $\boldsymbol{c}$ lattice direction. The study's selection criteria was the following:

> *Substitute titanium atoms into the 8i position subset only. If the minimum energy is shared by more than one position, calculate separate substitution pathways for each minimum energy position.*

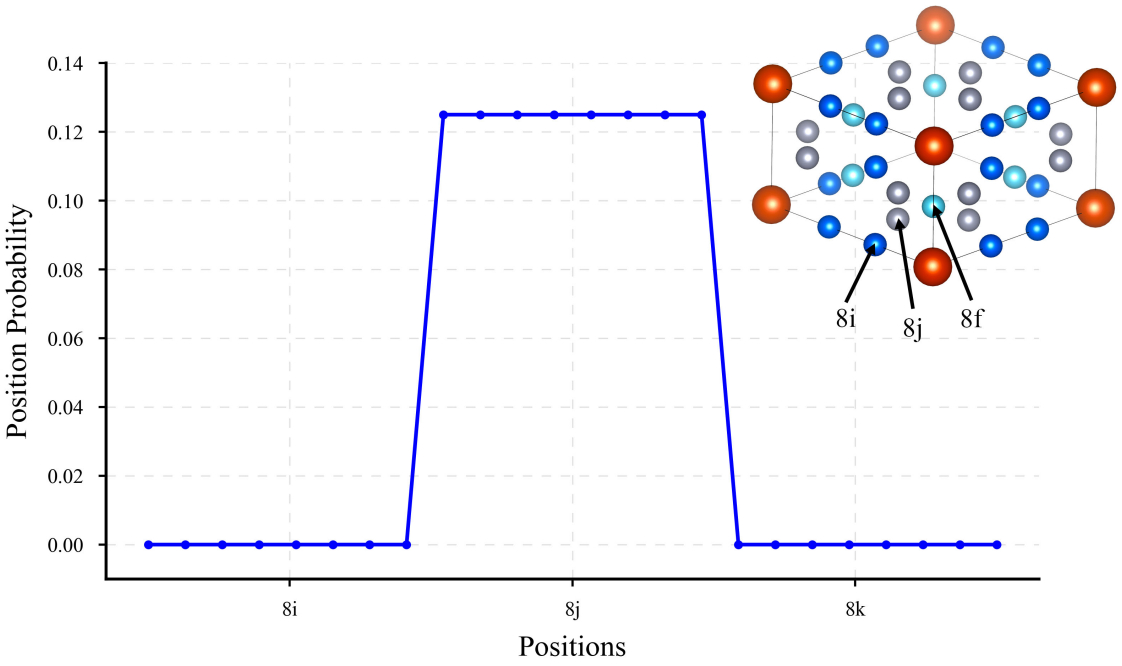

Figure 23: Probability comparison of the three Wyckoff position subsets in the RT_{12} structure at 300K, along with a visualisation of the general RT_{12} structure. Wyckoff position subsets are labelled, atoms which share the same colour as the labelled atom are in that subset. Probabilities are all normalised by the summed total of all the comparison ratios.

Narrowing the selection criteria to 8i substitutions only was motivated by the subset probability ratios given above and the need to avoid combinatorial explosions in the required computational work. Every possible minimum energy path was followed to capture a broad picture of the possible titanium substitution configurations. The choice of selection criteria can be verified by examining Figure 24 and seeing that at low temperature the criteria captures as much as 100% of the Total Configurational Probability defined in chapter 2.

The second study used 3×3×2 supercells, for which the selection criteria was the following:

> *Substitute titanium atoms into the 8i positions. If the minimum energy is shared by more than one position select the position with the lowest assigned numbering only.*

Curtailment of equally probable substitution pathways was necessary in this case for two reasons, the Quasi-Newton methods have an N^2 dependence on system size, and

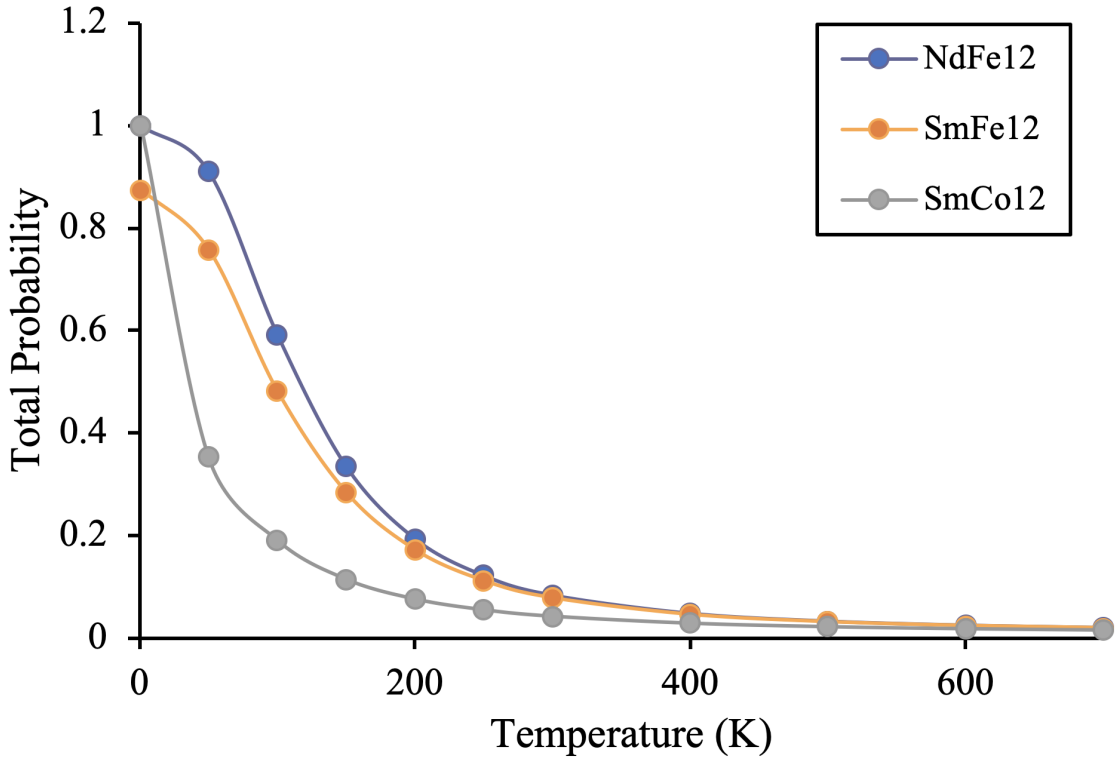

Figure 24: Total configurational probability graph with temperature for the 2×2×1 $RT_{12-x}Ti_x$ supercell structures.

combinatorial explosion has a $\left(\frac{N}{C}\right)!$ dependence on system size, where C is some constant and $C \geq 1$.

As the 3×3×2 selection criteria limits the number of analysable position configurations, it is not possible to use the total configurational probability as a measure of how well this criteria captures likely structures. Instead, the criteria was validated by comparison with others, the results of this can be seen in Figure 25. The alternative criteria still only selected one path at each stage, and are given below:

1. 8i positions only, choosing the maximum energy position at each stage.
2. 8j positions only, choosing the minimum energy position at each stage.
3. 8f positions only, choosing the minimum energy position at each stage.

As Figure 25 shows, for all structures, the 8i minimum energy position selection criteria produces significantly greater decreases in cohesive energy, giving a per substitution decrease that is between 227% and 664% greater for $NdFe_{12-x}Ti_x$, between 158% and

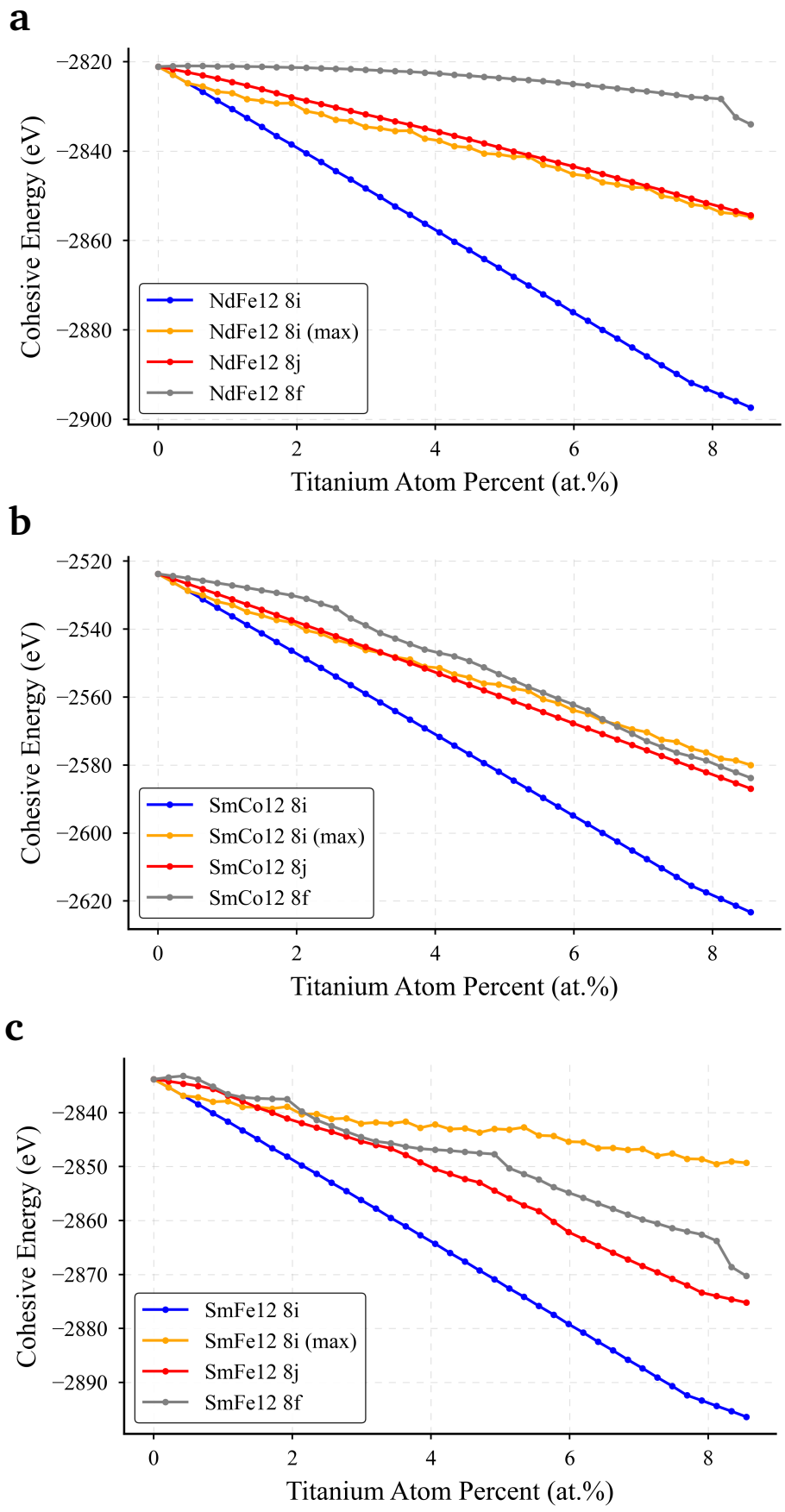

Figure 25: Selection Criteria comparison for a) $NdFe_{12-x}Ti_x$, b) $SmCo_{12-x}Ti_x$, c) $SmFe_{12-x}Ti_x$.

178% greater for $SmCo_{12-x}Ti_x$, and between 151% and 404% greater for $SmFe_{12-x}Ti_x$. From this it can be inferred the selection criteria produces one of the most probable substitution pathways.

3.4 Results

As titanium substitution occurs at low percentages and the goal is to minimise its inclusion to maintain magnetic properties, supercell models of the three crystal structures were used to attain lower titanium atom percentages. Supercells were needed because the RT_{12} unit cell only contains 26 atoms, meaning a single titanium substitution gives the a unitcell $\sim$3.85% titanium atom percent. With such high jumps it would not have been possible to investigate the lower percentages of titanium substitution, nor to perform a deep analysis of structural behaviour.

As the stability range of titanium substitution found by De Mooij and Buschow [95] in $RT_{12-x}Ti_x$ structures is $x \approx 1$, the present work only investigated titanium substitution up to $\sim$16Ti at.%, which equates to $x \approx 2$, or 4 titanium substitutions per unit cell. The higher percentage was chosen to investigate whether structural changes caused by titanium substitution above $\sim$8Ti at.% are responsible for the stability loss that results in the range found by D Mooij and Buschow.

As mentioned in the validation step, this work consists of two studies that used two different supercell sizes: $2\times2\times1$, and $3\times3\times2$. Owing to its increased size the $3\times3\times2$ supercell could reach lower titanium atom percentages and thus the majority of the analysis focuses on this structure.

Stabilisation of RT_{12} Structures

Across all structures, increasing titanium substitution produces an associated decrease in cohesive energy. Figure 26 shows this trend for the $2\times2\times1$ and the $3\times3\times2$ supercell structures separately. Inspecting the lattice parameters indicates part of the

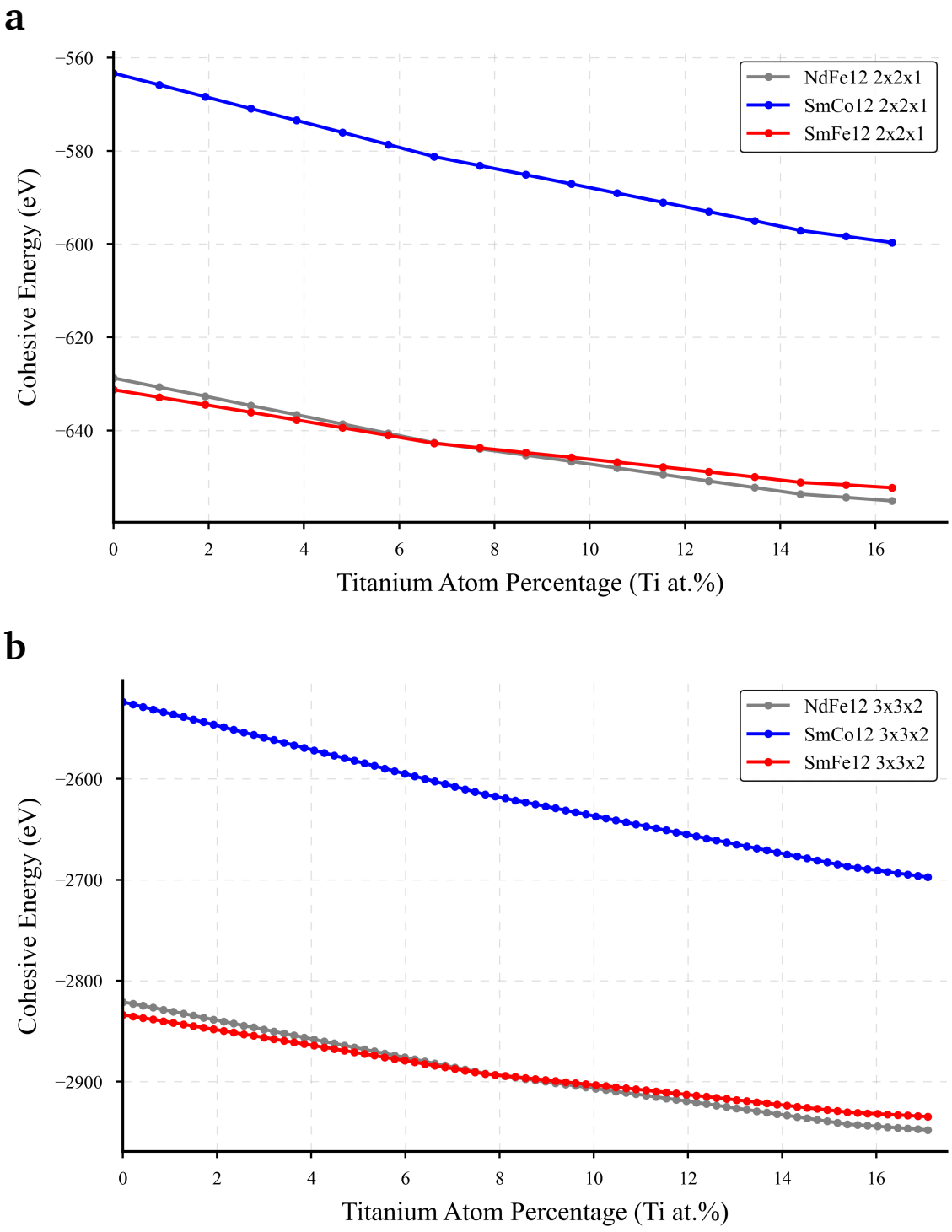

Figure 26: Cohesive energy with increasing titanium substitution for a) all 2×2×1 supercell structures, and b) all 3×3×2 supercell strucutures. The effect of substitution is shown up to 17Ti at.%

reason for the decrease in cohesive energy, titanium substitution causes an asymmetric expansion in the a, and b lattice parameters, an example of this can be seen in Figure 27 for $NdFe_{12-x}Ti_x$. The resultant symmetry breaking allows the structure to relax anisotropically and therefore more effectively into a lower energy state.

The dominant factor lowering the cohesive energy of the structure is the preferential bonds formed by titanium substitutions with their surrounding atoms. The minimum energy reachable by the bond is indicated by the Morse potential constant D_0 in Table 1. Taking the ratio of their D_0's shows that Fe-Ti interactions have a 6% lower minimum energy than Fe-Fe interactions, and Ti-Co interactions have a 10% lower minimum energy than Co-Co interactions. By the same analysis Nd-Ti interactions have an 18% higher minimum energy than Nd-Fe interactions, and Sm-Ti interactions have an 11%, and 8% higher minimum energy than Sm-Fe, and Sm-Co interactions respectively. Here a higher minimum energy indicates a weaker bond, and thus lower structural stability, and vice versa.

Therefore, in order to reach the minimum cohesive energy, titanium substitutions should have as few rare-earth nearest neighbours as possible. To establish how their proximity to rare-earths influences their preferability, the three Wyckoff position subsets were examined.

Wyckoff Position Subset Preference

Following from above, it's logical to assume that the 8i position subset has the lowest level of interaction with rare-earths. To test this hypothesis, the number of neodymium atoms that occur in the nearest 25 neighbours of all the possible Wyckoff positions were calculated. The first 25 nearest neighbours were chosen as this is equivalent to the number of atoms in a single RT_{12} unit cell, less one (the position being checked). Calculation confirmed that of all the subsets, 8i has the fewest rare-earth nearest neighbours, only one out of 25, whereas 8j has two, and 8f has three. This was quantified using two metrics, the average distance between the chosen position and its rare-earth neighbours, and the summed reciprocal of the distances between the chosen position

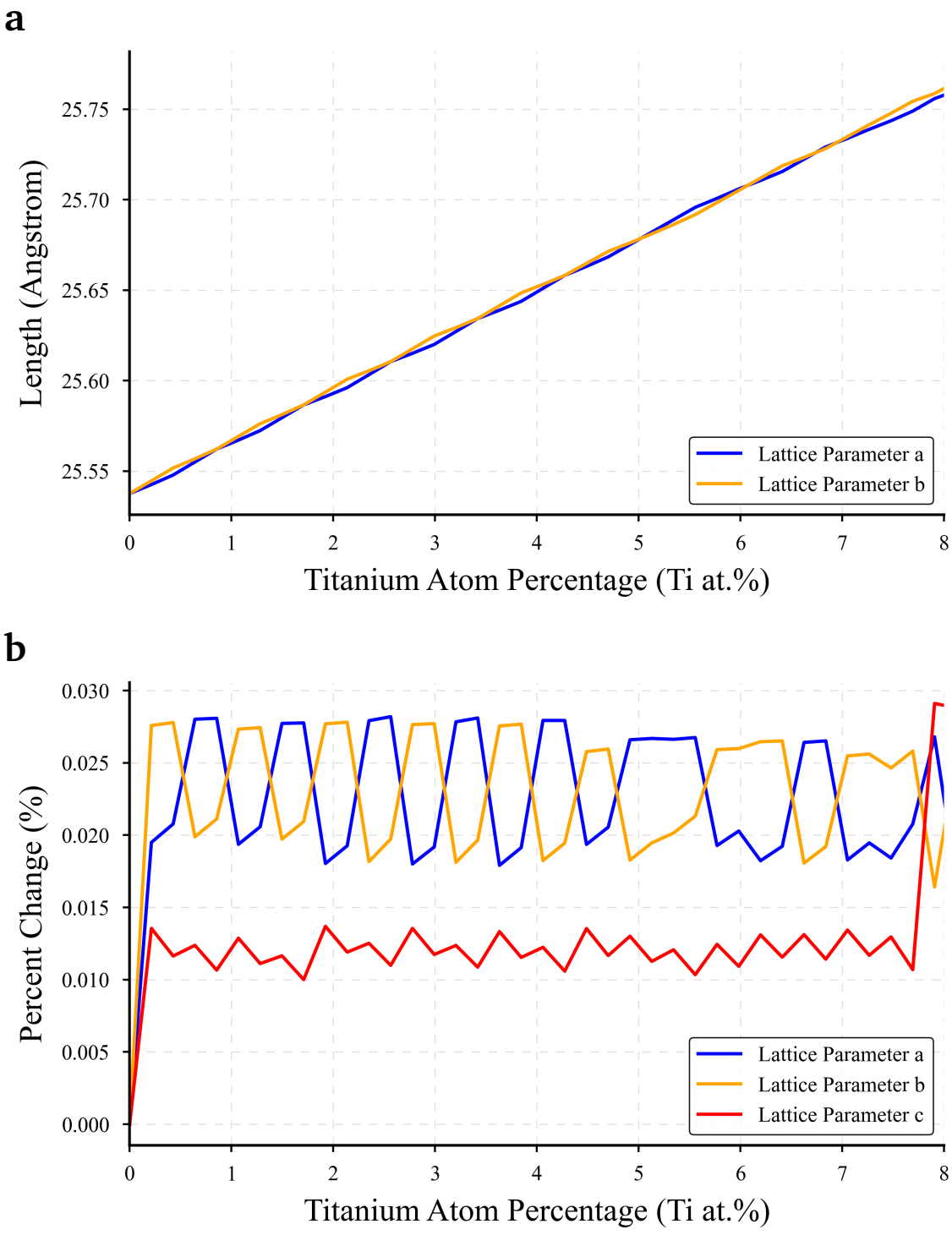

Figure 27: Lattice parameter changes for the $NdFe_{12-x}Ti_x$ 3x3x2 supercell structure, showing a) the absolute length of the a and b lattice parameters against titanium substitution, and b) the percentage change in all the lattice parameters from the crystal structure of the previous stage.

Wyckoff Subset	Nd Nearest Neighbours	Average Distance (Å)	S_R (1/Å)
8i	1	3.037	0.329
8j	2	3.099	0.645
8f	3	3.734	0.829

Table 3: Proximity of the three Wyckoff position subsets to rare-earth atoms in $NdFe_{12}$. Proximity is shown in three ways, firstly, through the number of Nd atoms within the first 25 nearest neighbours (one whole unit cell) of each position, secondly the average distance to each neighbour, and thirdly the summed reciprocal (S_R) of the distance to each neighbour. For the summed reciprocal a larger value means greater proximity to rare-earths

and its rare-earth neighbours. The equation giving the sum can be seen below:

$$S_R = \sum_{i}^{N} \frac{1}{D_i} \tag{3.1}$$

where S_R is the sum of the reciprocal distances, N represents the number of rare-earth nearest neighbours, and D_i is the distance from rare-earth i to the chosen position. Table 3 shows these metrics for $NdFe_{12}$, calculations for $SmFe_{12}$, and $SmCo_{12}$ show the exact same trend.

The summed reciprocal can measure the proximity of a position subset to any atom, the energetic preferability of this proximity is dependent on the particular interatomic interaction. For example, in the above case R-Ti interactions are unfavourable, so a higher S_R value indicates an energetically less favourable position. If the equation is altered to check each subset's proximity to iron atoms, it finds 8i has the largest S_R value and is therefore in the closest proximity to iron atoms. Thus, from calculation, the 8i position subset is maximally proximal to iron atoms (energetically favourable) and minimally proximal to rare-earth atoms (energetically unfavourable), resulting in the strong preference for this position subset. Wyckoff subsets 8j and 8f have very similar proximities to iron atoms, although 8j is slightly closer. This explains the remainder of the order preference, as the 8j position subset is the second most proximal to iron atoms

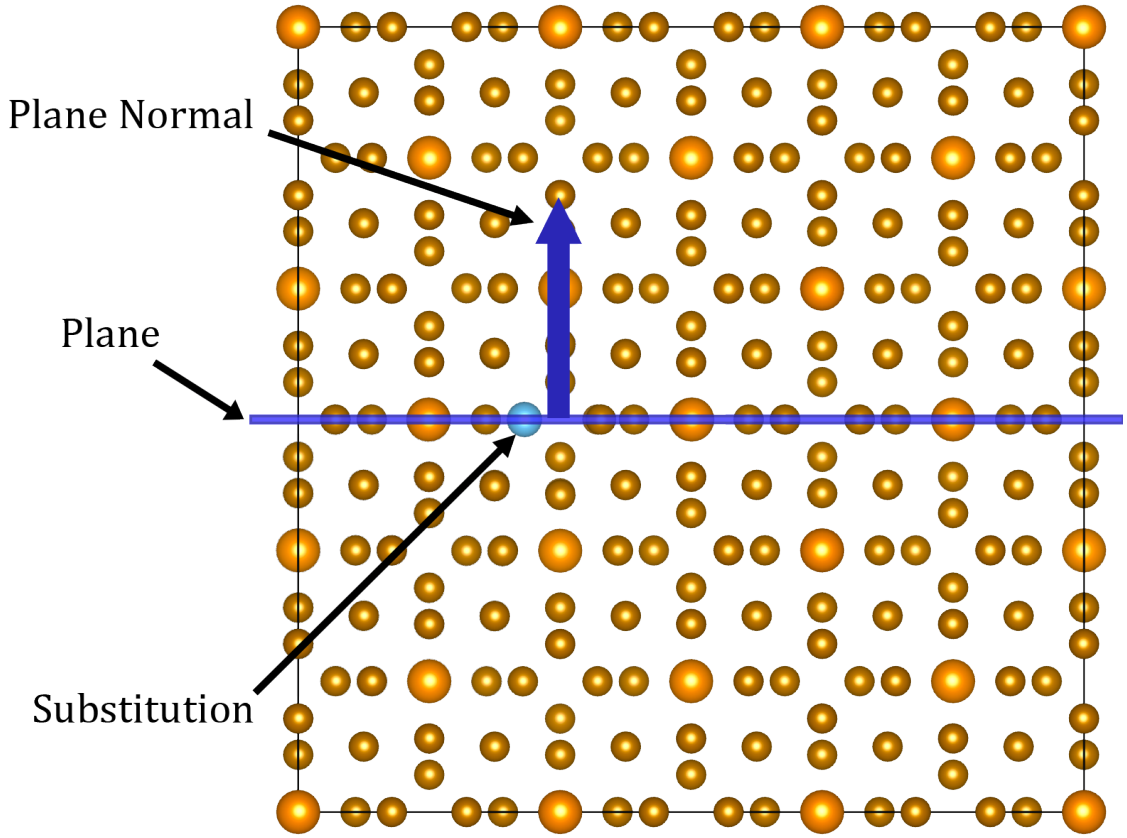

Figure 28: Diagram of plane connecting a titanium substitution with its nearest rare-earth in RT_{12}, the plane normal gives the direction of greatest expansion

(energetically favourable), and the second least proximal to rare-earths (energetically unfavourable), giving it the second highest energetic favourability. Only the 8f subset is left, which is least proximal to iron atoms, and most proximal to rare-earths, the worst case scenario energetically and the least energetically favourable subset.

Structural Changes from Titanium Substitution

The asymmetry induced in the a, and b lattice parameters, discussed in Stabilisation of RT_{12} Structures, is determined by substitution site. Maximum expansion occurs in the lattice direction that is closest to parallel with the normal of a plane that is both perpendicular to the ab plane and cuts through the substitution and its nearest rare-earth. Figure 28 shows a visual illustration of this plane, and the direction of maximum expansion. At first glance this seems counter intuitive, as the R-Ti interatomic interactions have a greater equilibrium distance, r_0, than any of the R-Fe, and R-Co interactions, which leads to the assumption that this interaction will cause maximum expansion in

the lattice direction aligned in the plane. However, neodymium and samarium have ∼3 times the mass of titanium, and therefore, on relaxation, titanium moves the majority of the distance required to reach equilibrium. To achieve this the titanium atom moves directly away from the rare-earth within the aforementioned adjoining plane, forcing it closer to some of its other nearest neighbours - iron atoms aligned parallel to the plane's normal. Because Iron is roughly the same mass as titanium, these interactions have a more balanced effect, and the iron atoms are pushed out of their positions, along the positive and negative of the plane normal respectively. Their movement induces an asymmetrical expanding force on the lattice and drives the asymmetric expansion in lattice parameter a or b. A general expansion of all lattice parameters occurs, as all of titanium's neighbour interactions have a greater equilibrium distance.

Substitution Patterns

In all structures the titanium substitutions up to ∼8Ti at.% follow a pattern which maximally spreads them out across the structure. The pattern is most easily seen and understood in the 3×3×2 supercells, which can be see in Figure 29. Although the pattern is slightly different for each structure there is an overarching rule to the the titanium atom placement which can be seen in Figure 30. Drawing lines across the supercell shows that titanium substitutions follow a pattern across the structure that avoids close contact in the a and b lattice directions, and confines each substitution within a surrounding cell of rare-earth atoms. As discussed previously these rare-earth atoms act as a barrier to the lattice expanding effects of titanium, and as the Ti-Ti interaction has the highest equilibrium distance of all the transition metal interactions, ∼3.35Å, this spread out pattern prevents Ti-Ti interactions causing large energetically unfavourable lattice expansions.

One thing to note is that, whilst titanium substitutions appear to avoid close placement in the a and b lattice directions, they do align vertically along the z axis or c lattice direction. Along this axis, however, they are separated by ∼4.82Å, which puts them right at the tail end of their morse potential interaction. Th energy gradient at this

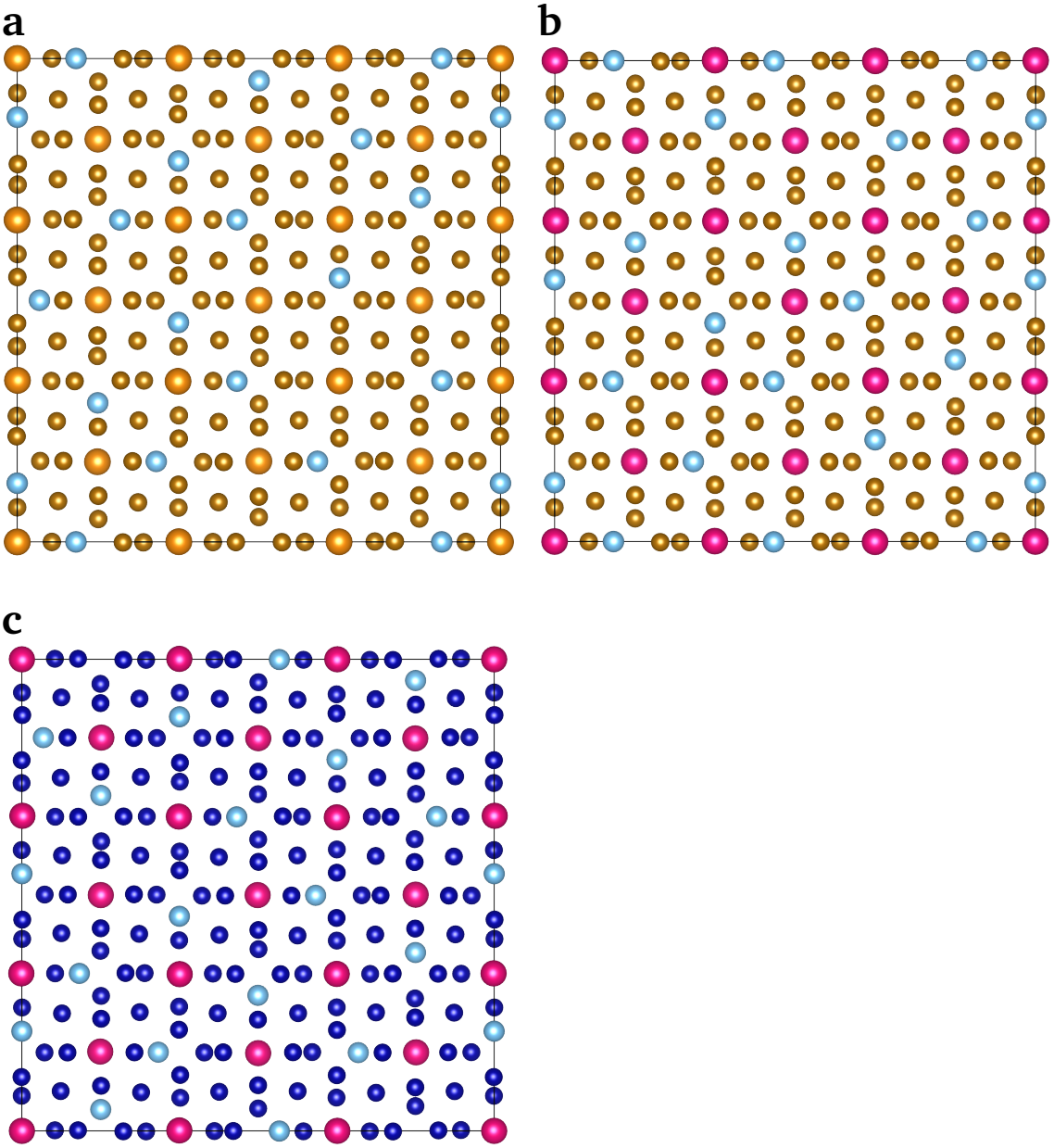

Figure 29: $RT_{12-x}Ti_x$ structure filling pattern for a) $NdFe_{12-x}Ti_x$, b) $SmFe_{12-x}Ti_x$, and c) $SmCo_{12-x}Ti_x$, up to ~8Ti at.%. Across all the structures, the large yellow atoms are neodymium, the small yellow atoms are iron, the large pink atoms are samarium, the small dark blue atoms are cobalt, and the small light blue atoms are titanium.

point can be calculated using the differential of the Morse potential from Equation 2.8:

$$\frac{du(r_{ij})}{dr} = D_0 \left[-2\alpha e^{-2\alpha(r_{ij}-r_0)} + 2\alpha e^{-\alpha(r_{ij}-r_0)} \right] \tag{3.2}$$

where D_0 scales well depth, α controls potential well width, r_0 defines the energy minimum point of the well, and r_{ij} is the distance between two atoms i, and j. Subbing in the values for the Ti-Ti interaction from Table 1 along with $r_{ij} = 4.82$Å gives 0.221

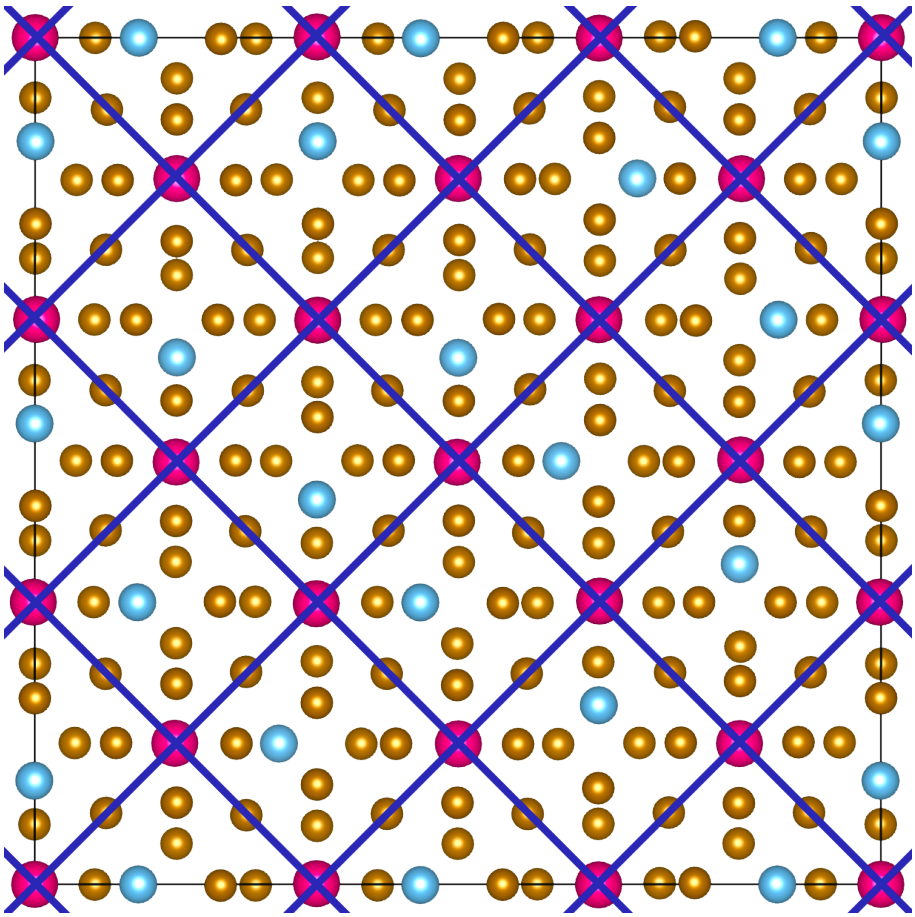

Figure 30: Visual illustration of the rule dictating the overarching pattern for $SmFe_{12-x}Ti_x$ at 8Ti at.% (or 36 titanium substitutions for a 3×3×2 structure). The same rule can be decuded from the pattern of any of the $RT_{12-x}Ti_x$ structures. Here the pink atoms are samarium, the yellow atoms are iron, and the light blue atoms are titanium.

eV/Å for the energy gradient, which equates to a minor force pulling the two atoms closer together. As the force is so minor and causes lattice contraction not expansion, these interactions are of little relevance to the overall stability of the crystal structure. The pattern formed by titanium substitution up to ∼8Ti at.% is termed substitution pattern one, or the primary substitution pattern.

Beyond ∼8Ti at.% the primary substitution pattern is curtailed by a lack of available substitution positions, forcing the occurrence of a new substitution pattern, which is termed substitution pattern two, or the secondary substitution pattern. The structural changes caused by the secondary substitution pattern are key to understanding the limited stability range of $RT_{12-x}Ti_x$.

Figure 31 shows the new substitution pattern's first substitution, and a secondary figure shows what the completed pattern would look like if it could be reached by

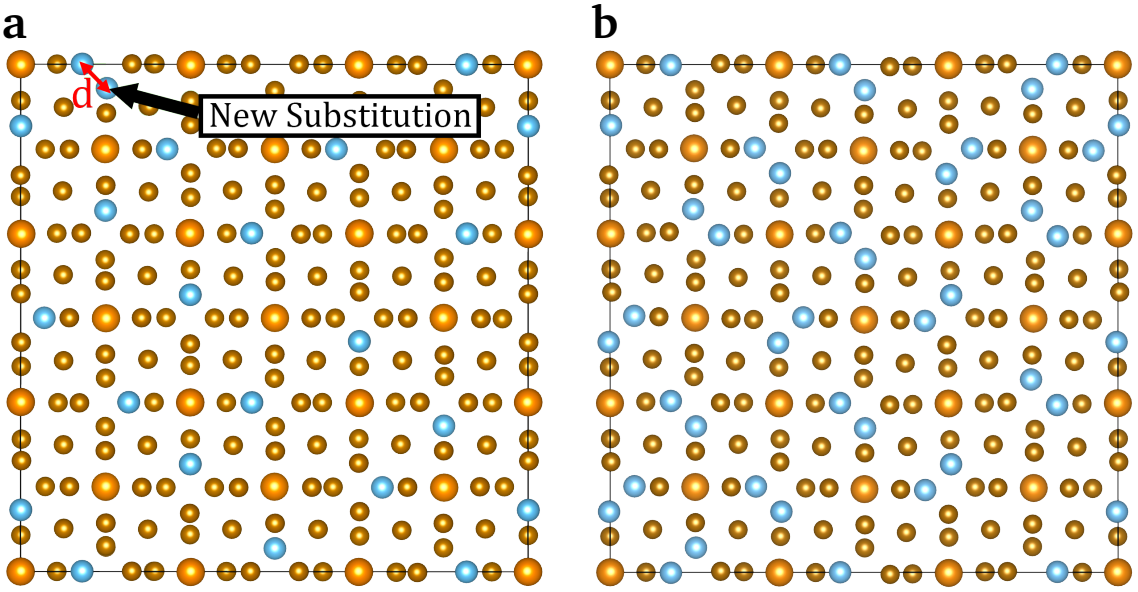

Figure 31: Secondary substitution pattern for the $NdFe_{12-x}Ti_x$ 3×3×2 structure, showing a) The first substitution in the secondary pattern - indicated in the figure, and b) the complete pattern after all the secondary pattern's substitutions at ∼15.5Ti at.%. The red arrow between the two neighbouring titanium atoms is used to indicate there is a distance d between them. Both structures are shown looking down the c axis.

any of the investigated structures, which is doubtful due to stability. Figure 31 shows that, in the new substitution pattern, titanium atoms must be in close proximity to other titanium atoms. As discussed this is energetically unfavourable due to the Ti-Ti interaction's large equilibrium distance, which is ∼0.4Å more than its interaction with any other transition metal element. In fact, due to the primary substitution pattern, secondary substitution atoms are in close proximity to two titanium atoms, as is shown in Figure 32. To illustrate why this is an issue, examine $NdFe_{12-x}Ti_x$. Before titanium substitution, the soon to be substituted iron atom and the titanium atoms are 2.943Å apart, which is nearly exactly their preferred equilibrium distance of 2.914Å. If a titanium atom is placed directly into the same position as the iron atom, using Equation 3.2, we get an energy gradient/force between a titanium atom pair of -1.64eV/Å, the negative sign indicates this is an expanding force. As there are two titanium atoms in the vicinity of this substitution this force is doubled and, due to geometry, acts mainly in the c lattice direction.

Structurally this means every titanium substitution in the second substitution pattern causes a significantly larger increase in the c lattice parameter. Figure 33 shows this

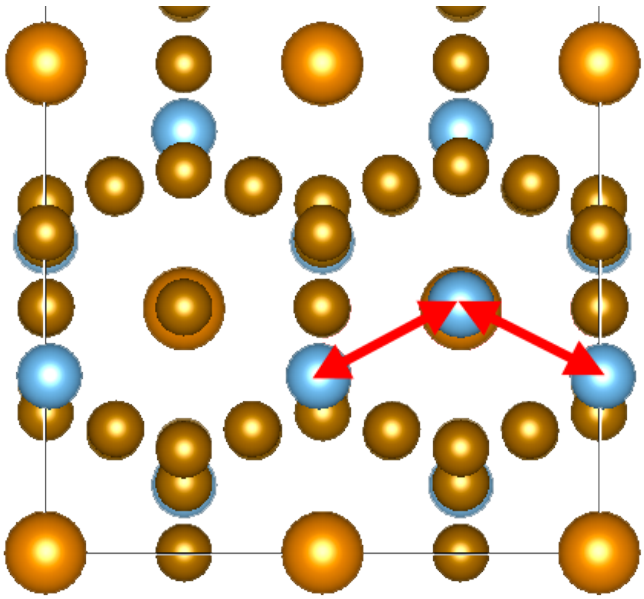

Figure 32: Side view of $NdFe_{12-x}Ti_x$ with the c lattice parameter horizontally across the page. The red arrows indicate the new titanium substitution's interaction with its two titanium neighbours.

increase for all three structures. After ∼8Ti at.%, the percentage change in the c lattice parameter with every substitution jumps to roughly double what it was previously. Even after minimisation the distance between the two primary substitution titanium atoms and the single secondary substitution titanium atom is still only 3.06Å roughly 0.3Å below the equilibrium distance, making the force between them -0.936eV/Å. This is 10 times the magnitude of the previous iron-titanium interactions which had a value of 0.0932eV/Å, a small contractive force. Stress induced by titanium atoms in the structure, which cannot be removed by relaxation, will eventually destabilise, warp, and transform the structure into a lower energy state.

In short, the large structural changes caused by titanium substitutions in the secondary substitution pattern, accompanied by the stress they induce in the system, are the cause of the unfavourability of further titanium substitution.

Energy Density Changes in the Second Substitution Pattern

An overall rubric combining cohesive energy with coarse structural changes is the energy density, which divides a structure's cohesive energy by its volume. Figure 34 shows energy density against Ti at.% for the three structures as 3×3×2 and 2×2×1

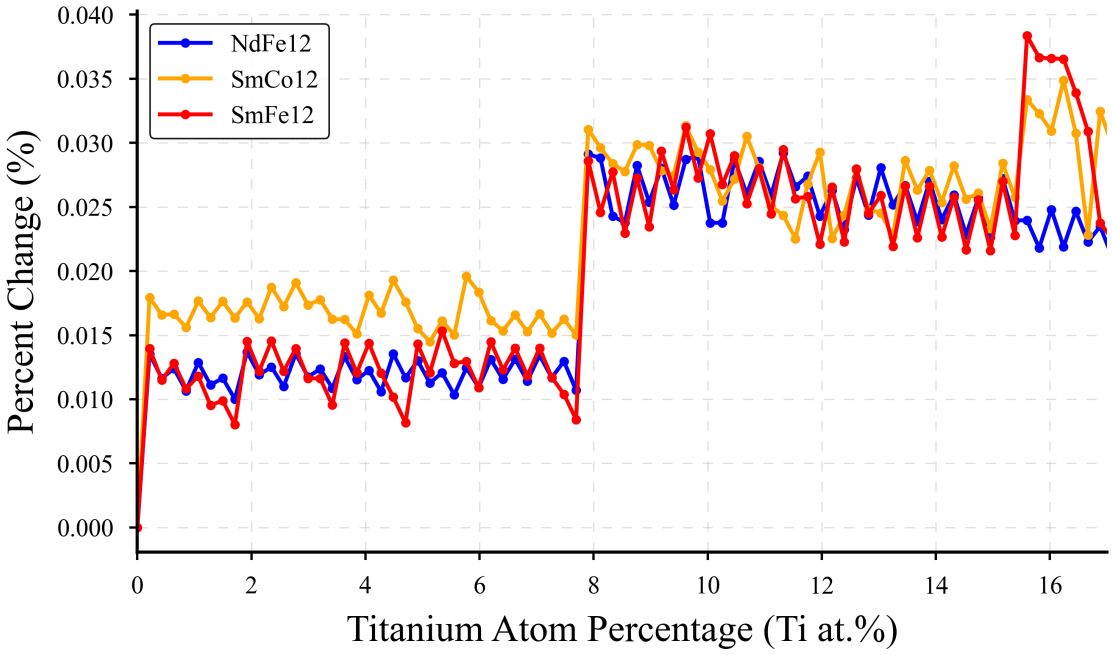

Figure 33: C lattice parameter expansion against titanium atom percentage for $NdFe_{12-x}Ti_x$, $SmCo_{12-x}Ti_x$, and $SmFe_{12-x}Ti_x$.

supercells. As the graphs show, for two of the structures $NdFe_{12-x}Ti_x$, and $SmCo_{12-x}Ti_x$ the energy density decreases with additional titanium over the first substitution pattern, whilst for $SmFe_{12-x}Ti_x$ it increases ever so slightly. Beyond 8Ti at.%, within the second substitution pattern, all structures have a strong increase in energy density. Undoubtedly, the change is due to, firstly, unfavourable titanium-titanium bonding in the secondary substitution pattern and, secondly, a larger increase the c lattice parameter with every substitution.

Lower energy density corresponds to structural instability, as its a measure of the binding force keeping the crystal together divided by the volume of space the crystal occupies. If the volume is expanding faster than the force binding the crystal together eventually the expanding space will lower the activation energy for some form of structural transformation.

Summed Comparative Probability

Because of the Cascading Probabilities method, the Boltzmann factor of each possible position configuration is known at every stage. Working on a stage by stage basis, and

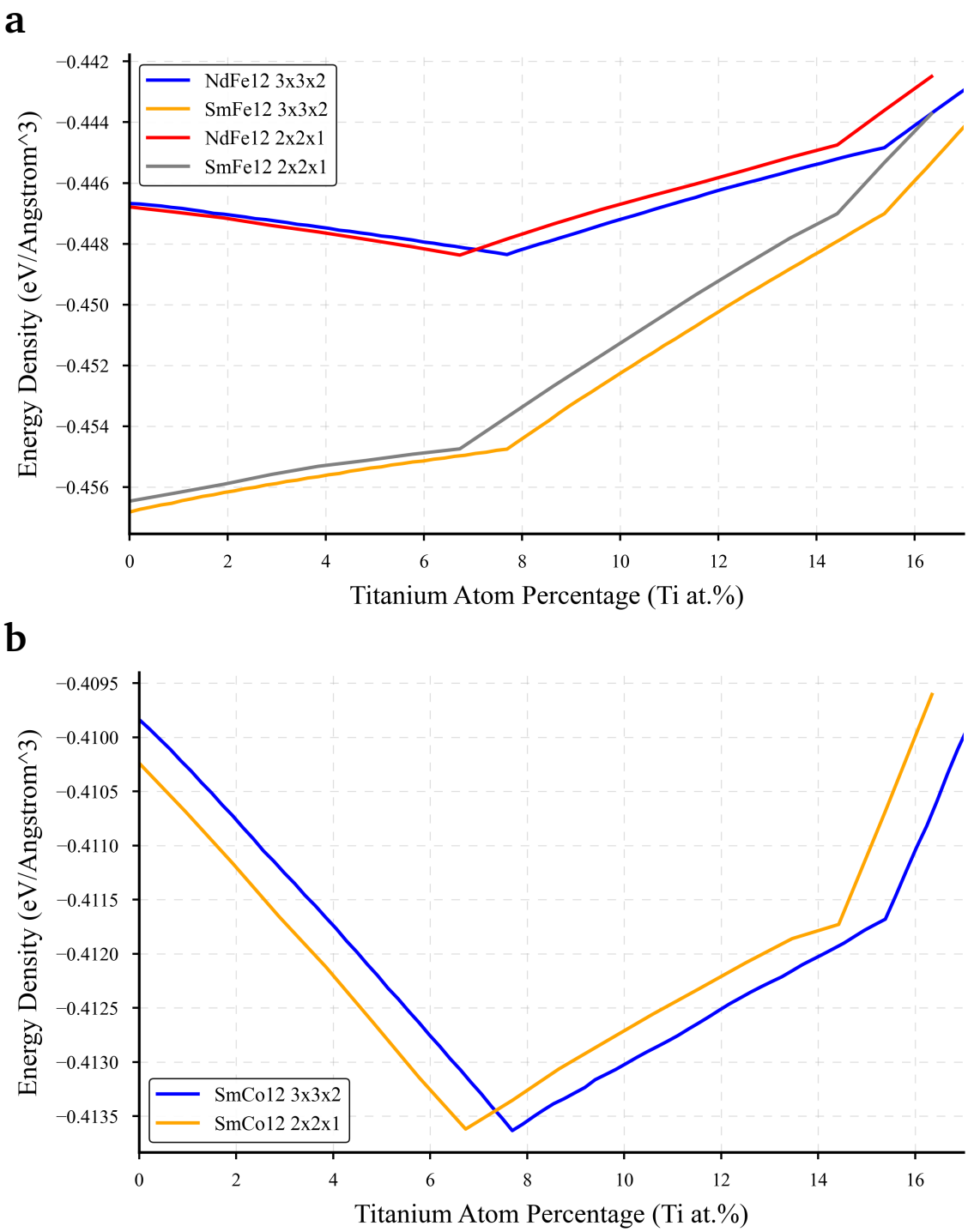

Figure 34: Energy density against titanium atom percentage (Ti at.%) for all the investigated supercell structures, showing a) the energy density trend for $NdFe_{12-x}Ti_x$, and $SmFe_{12-x}Ti_x$, and b) $SmCo_{12-x}Ti_x$.

taking the ratio of each configuration's Boltzmann factor with the minimum energy configuration's Boltzmann factor and summing them produces that stage's Summed Comparative Probability. This measure quantifies how close the positions' energies are to the minimum energy position at each stage of substitution. The larger the number,

the larger the number of positions that are close to the minimum energy and hence of similar probability to the minimum energy position. Figure 35 shows a measure of this for the 3×3×2 supercells of the three structures. The regular jumps in Summed Comparative Probability are due to intermittent symmetries that occur as titanium is substituted into the structure. High symmetry corresponds to large peaks, as it suggests there are multiple positions with identical neighbour environments. That explains the large peak at the start of every graph, where the titanium substitution has every possible 8i position to choose from, and the increased peak at the end of every graph, where the titanium substitution is the first of the secondary substitution pattern. The trend of every graph is a decrease in Summed Comparative Probability as titanium substitution continues, indicating there are fewer positions at each stage which come close to the minimum energy. This implies that as substitution increases each new titanium atom must expend more energy reaching a desirable position, or else settle for a slightly less favourable one. As shown in this chapter, unfavourable titanium substitutions have a destabilising effect on the crystal structure. As unfavourable substitutions become more likely with increasing Ti at.%, this is a further factor limiting the structural stability range of $RT_{12-x}Ti_x$.

3.5 Discussion

Using ab initio derived Morse potentials, this chapter has investigated the structural and energetic changes caused by titanium substitution and found that titanium stabilises the RT_{12} structures by forming preferential bonds with minimum structural effects below ∼8Ti at.% in the Primary Substitution Pattern. Beyond ∼8Ti at.%, titanium goes through a secondary substitution pattern that induces much larger changes in the crystal structure that increase the destabilising stress within the crystal, likely causing it to undergo a lattice transformation. This unfavourable secondary substitution pattern is the reason it's not possible to increase Ti at.% much beyond the Primary Substitution Pattern.

For $NdFe_{12-x}Ti_x$ based structures the stability range is roughly 6.1-9.2 Ti at.%, which

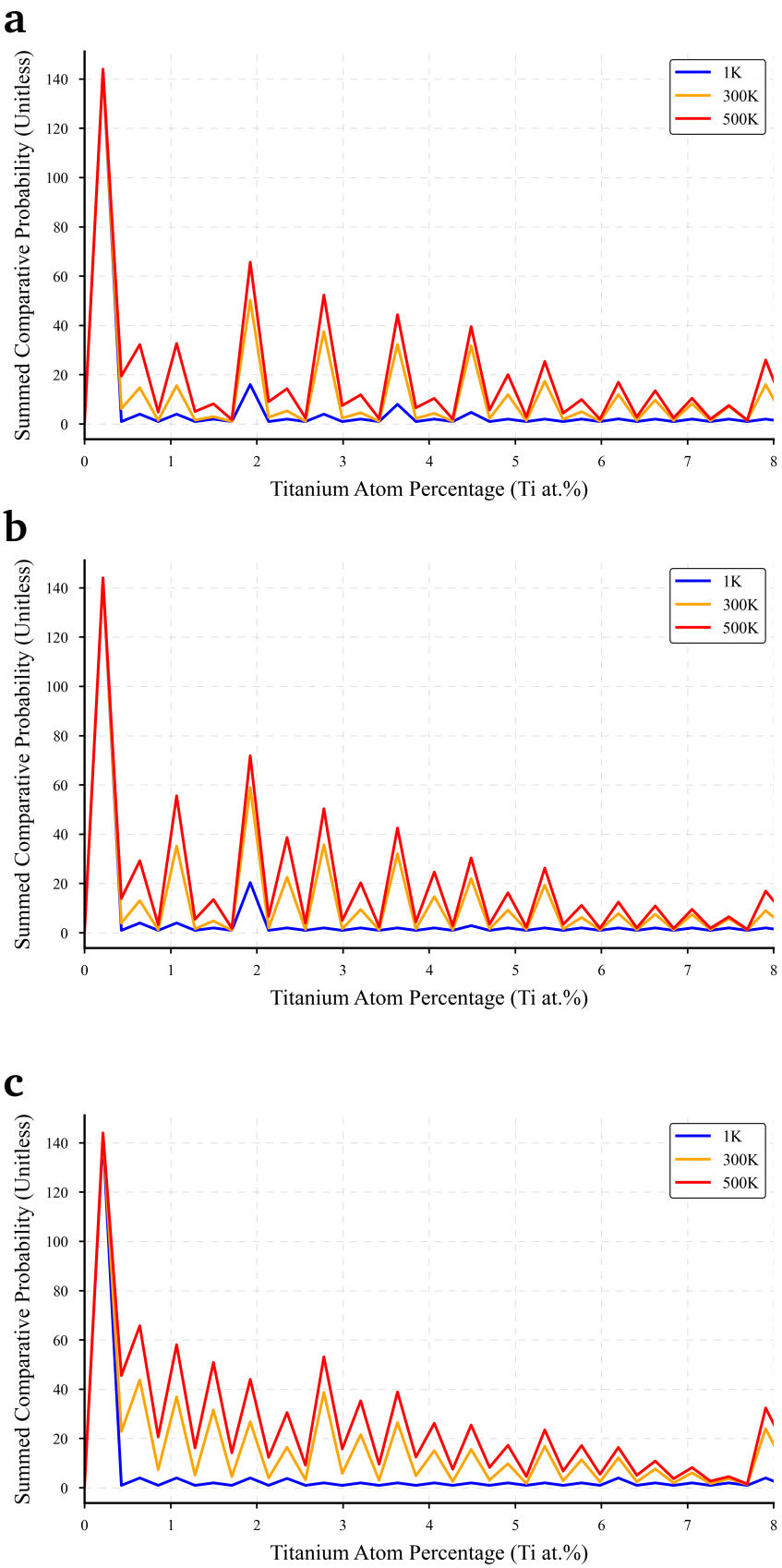

Figure 35: Total comparative probability against titanium atom percentage for a) $NdFe_{12-x}Ti_x$, b) $SmFe_{12-x}Ti_x$, and c) $SmCo_{12-x}Ti_x$.

aligns reasonably well with its minimum energy density. However, for $SmFe_{12-x}Ti_x$ the energy density always increases despite its cohesive energy decreasing with increasing titanium substitution. This is due to volume growth and indicates that the crystal structure does not become more stable as a direct consequence of titanium substitution. However, it is possible that titanium's presence in a bulk polycrystalline structure may affect the presence of tertiary phases which increase stability, although this is not investigated here.

In contrast to $SmFe_{12-x}Ti_x$, $SmCo_{12-x}Ti_x$ has the largest decrease in energy density of all the structures, and maintains its lower energy density over a wider Ti at.% range than the iron based structures. Therefore, this work suggests a quarternary structure of $Sm(Fe,Co)_{11}Ti$ could have the improved magnetic performance conveyed by the iron atoms coupled with the stability provided by cobalt interactions. These structures are currently being investigated by Hono et al.[96] as a possible replacement for $Nd_2Fe_{14}B$.

This work suggests that, when considering $RT_{12-x}Ti_x$ single crystal structural integrity only, the titanium atom percentage be kept near the low end of the the primary substitution pattern. This will allow improvements in stability from titanium bonding without the destabilisation of the structure that is a result of titanium atoms falling into the secondary substitution pattern. Keeping titanium substitution away from the upper end of this scale will also avoid any unfavourable substitutions that occur due to the decreasing number of primary substitution pattern positions. On a single crystal basis, this work shows there is no benefit to increasing titanium substitution beyond this point in any of the $RT_{12-x}Ti_x$ structures.

4 Effect of Pressure on the melting point of $NdFe_{12}$

Introduction

Papers by Miyake et al.[49], and Hirayama et al.[50] have shown the high performance of $NdFe_{12}N$. In the first case by first principles, and in the latter case by experimental epitaxial growth. However, neither paper considers the possibility of a complete manufacturing route for $NdFe_{12}N$.

This was partly addressed in Chapter 3 by investigating the effect of titanium substitution on stability and structure in the RT_{12} family. Providing a range of optimal element ratios for maximum structural stability, a key stage in initial ingot production[97]. Initial ingots are turned into powder by pulverisation, jet milling, or some other comparable method, before finally undergoing densification. Densification covers a range of processes that turn intermediary magnetic powder into a solid magnet. Following one of three common methods: polymer bonding, hot press deformation, and hot press sintering. Polymer bonding uses a resin to bind together the original powder which can be compressed into a variety of shapes and aligned along a magnetic field due to the powders high anisotropy[98]. Hot press deformation compacts a magnetic powder in a mold under high pressure and heats it until liquid grain boundaries can follow a solution-precipitation creep process in which grains grow into one another along strain lines densifying the compact. Hot press sintering follows a similar procedure but heats the powder to higher temperatures than that used in hot press deformation. Higher temperatures cause partial liquefaction and the liquifidied sections of each part of the powder melt into one another. This process is not as dependent on induced strain from the pressing and thus performing an initial alignment of the powder under a magnetic field and maintaining this throughout the process is effective at increasing the anisotropy of the final magnet. Hot press sintering is the best method used today and has remained the same since it was first used by Sagawa et al.[42] - the original discoverers of $Nd_2Fe_{14}B$.

Of the three processes, hot press sintering provides magnets with the highest energy product, but also requires the highest temperatures, with typical sintering temperatures

in $Nd_2Fe_{14}B$ being $\sim$1400K[97]. As this requires the material to partially melt, it's necessary to have a firm understanding of the materials behaviour with temperature. As the most investigated and most promising of the RT_{12} structures, this chapter investigates the melting point of $NdFe_{12}$, with a view towards future manufacturing.

The first attempt at this used the same ab initio derived pair potentials from the preceding chapter and a simplistic methodology which heated a perfectly periodic crystal, however, this had a number of issues. Firstly, the basic methodology resulted in the modelled materials melting at temperatures significantly higher than expected, a phenomena known as superheating[99]. Superheating occurs because melting is a dynamic process and must nucleate from some initial point, generally a discontinuity in the lattice. In a perfect periodic crystal there is no obvious point of nucleation, and so nucleation occurs at the mechanical melting point. The mechanical melting point corresponds to a phonon instability in the crystal, at this point the lattice vibrations cause catastrophic melting across the whole crystal simultaneously without any specific point of nucleation[99]. Experimentally this generally does not occur, owing to the presence of extended defects, such as grain boundaries, which nucleate melting far more easily than the bulk[100]. This is possible as high atom mobility is a requirement for melting and grain boundaries have this property due to their imperfect atomic fits.

In order to provide areas of high atom mobility and thus avoid superheating, the methodology was changed to the two phase coexistence methodology described in Section 2.1.3 above. This lowered the melting temperatures but not to their true values, which lead to a secondary problem, the inability of the original pair potentials to capture structural behaviour at high temperature. This is a common problem, as empirical potentials are an approximation to true interatomic interactions, and thus no method can be considered wholly accurate. For example, due to silicon's many technological uses, numerous empirical potentials have been created and tested against one another[101] in a drive to produce the most accurate simulations. Even potentials that are based on ab initio calculations are biased by the environment from which they are derived. For the original potentials, the ab initio data was calculated at 0K, and thus the potentials are

Atom Pair	D_0 (eV)	α (1/Å)	r_0 (Å)	Cut Off (Å)
Fe-Fe	0.401	1.3086	2.9119	14.077
Fe-Nd	0.505403	1.28603	3.32096	10.99023
Nd-Nd	0.26148	0.78305	4.41936	12.7512

Table 4: Refit Morse potential parameters used in the $NdFe_{12}$ melting point simulations.

only truly accurate at or near that temperature.

Testing the potentials at high temperature on the pure base-structures of neodymium and iron showed that the potentials produced cohesive energies that were 5% lower (neodymium), and 55% higher (iron) than those reported in the literature. Further examination showed discrepancies in the elastic constants, the bulk modulus, the Young's modulus, and longitudinal wave speed.

To address this problem, constants from materials in the Nd-Fe phase diagram were collected and used as the fitness parameters for a Genetic Algorithm, with the aim of refitting the pre-existing ab initio potentials to accurate material constants. The material constants are given in Tables 6 and 7. The specifics of the Genetic Algorithm method, and the solid-liquid coexistence method are given below. For the non-specific aspects of these methods please see Section 2.1.2, and Section 2.1.3 respectively.

4.1 Study Resources

The final parameters of the refit Morse potentials can be seen in Table 4 and are shown visually in Figure 36.

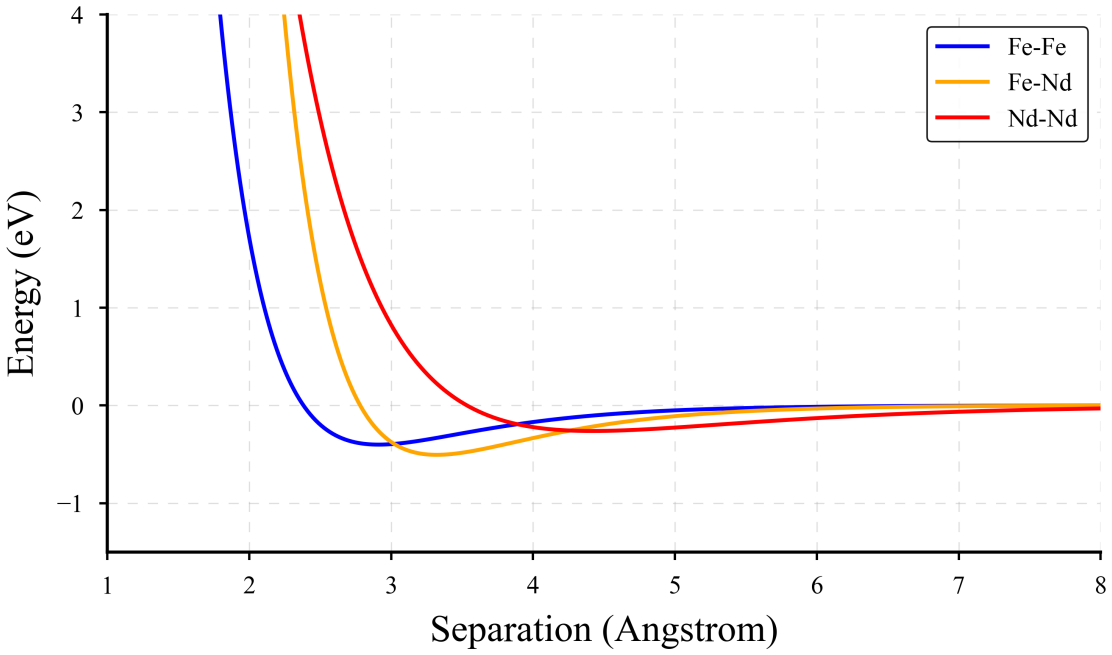

Figure 36: Refit Morse potentials used for the $NdFe_{12}$ melting point simulations.

4.2 Methodology specifics

4.2.1 Genetic Algorithm

As a binary structure, $NdFe_{12}$ interacts through three potentials Nd-Nd, Fe-Fe, and Fe-Nd. Therefore, the genetic algorithms used in this work were targeted at these three potentials. The "gene" or parameter set used by the genetic algorithm was comprised of all the Morse potential parameters plus cut off radius. The fitness function summed the percentage differences between the calculated and expected material properties - its form can be seen in Equation 2.32. Weighting factors were chosen so that the most important parameters to melting, for example cohesive energy, took primacy in directing solutions. The material constants chosen for neodymium and iron can be seen in Table 5 alongside their respective weightings. As mentioned, the cohesive energy has the highest weighting of 1,000 making it 20 times more significant than any other constant, and overwhelmingly the most important, due to its strong influence on melting temperature. The Lattice parameters were given a weighting of 50 because they are a fundamental part of the crystal's structure, which the potentials must capture to be considered a good approximation of reality. Trial and error showed that without high weightings the lattice

Material Constant	Weighting
a (Å)	50
b (Å)	50
c (Å)	50
α (°)	1
β (°)	1
γ (°)	1
E (eV)	1000
B (GPa)	8
c_{11} (GPa)	3
c_{12} (GPa)	3
c_{44} (GPa)	3
P (Km/s)	50

Table 5: Material constants used for the Fitness function (Equation 2.32) in the neodymium and iron potential fittings, alongside the weightings, w_i, each is given in the fitness function. Where a, b, c are lattice parameters a, b, and c, α, β, and γ are the angles between the lattice vectors, E is the cohesive energy of structure, B is the Bulk Modulus, c_{11}, c_{12}, and c_{44} are elastic constants, and P is the longitudinal sound wave speed.

parameters strayed from their expected values. In contrast, the angles of the crystal were given the lowest weighting of 1 because trial and error showed that higher weightings made little difference to structural accuracy. Longitudinal sound wave speed was given a weighting of 50 as it is a proxy for all the elastic constants and has consistently measured values across the literature. Every other constant was given a lower weighting as their measured values differ across sources.

The material constants used to fit the Nd-Nd and Fe-Fe potentials were taken from the α-neodymium and α-iron structures respectively - the relevant material constants can be seen in Table 6. Fitting the Nd-Fe potential was more complicated as no fundamental research into the material constants of Nd-Fe binary phase structures could be found. Despite this, $NdFe_{12}$[49], and Nd_2Fe_{17}[107] are well studied structures and could provide some of the material constants. Unfortunately, the only constants available with any certainty were lattice parameters, however, to provide more fitting points to the

Material Constant	α-Neodymium	α-Iron
a (Å)	3.657[1]	2.8665[1]
b (Å)	3.657[1]	2.8665[1]
c (Å)	5.902[1]	2.8665[1]
α (°)	90[1]	90[1]
β (°)	90[1]	90[1]
γ (°)	120[1]	90[1]
E (eV)	-6.8[2]	-8.56[2]
B (GPa)	32.7[2]	170[e]
c_{11} (GPa)	54.8[3]	239.26[5]
c_{12} (GPa)	24.6[3]	135.78[5]
c_{44} (GPa)	15.0[3]	120.72[5]
P (Km/s)	2.33[4]	4.91[4]

Table 6: Material constants found in the literature for α-neodymium and α-Iron. Superscripts [1, 2, 3, 4, 5] represent citations [102, 103, 104, 105, 106]. An explanation of the meaning of each material constant can be found in Table 5 above

fitness function, it was estimated that both materials have a similar Young's modulus to $Nd_2Fe_{14}B$, and that their cohesive energies make Nd_2Fe_{17} the more stable of the two structures.

The expected cohesive energies were estimated by calculating the minimum cohesive energy necessary for $NdFe_{12}$ to have a formation energy of zero: -109.52eV. To ensure the structure had a negative formation energy, the desired cohesive energy was set below this at -111.3eV, a $\sim$1.6% decrease. To ensure the preferability of Nd_2Fe_{17} was maintained, the per atom cohesive energy was set 0.07eV lower, giving a the structure a desired cohesive energy of -248.1eV. All the material constants used and their weightings can be seen in Table 7. The weightings for the experimentally confirmed lattice parameters were highest, followed by a slightly lesser weighting for the two structures' assumed cohesive energies, the speculative estimation of Young's modulus was given the lowest weighting. The fitness function used for all potential fits is Equation 2.32 given in Section 2.1.2, which calculates the sum of all the weighted percentage differences.

Material Constant	Nd_2Fe_{17}	$NdFe_{12}$	Weighting
a (Å)	8.582[1]	8.52[2]	10
b (Å)	8.582[1]	8.52[2]	10
c (Å)	12.463[1]	4.80[2]	10
α (°)	90[1]	90[2]	10
β (°)	90[1]	90[2]	10
γ (°)	120[1]	90[2]	10
E (eV)	-248.1	-111.3	8
Y (GPa)	165[3]	165[3]	3

Table 7: Material constants found in the literature for Nd_2Fe_{17} and $NdFe_{12}$. Superscripts [1, 2, 3] represent citations [107, 49, 108]. An explanation of all material constants can be found in Table 5, apart from the final constant Y (GPa) which represents the Young's modulus.

4.2.2 Two Phase Solid-Liquid Coexistence

LAMMPS was used for all the simulations, the units style was metal, the choice of time step was 0.001ps, and the temperature and pressure damping constants were 100 time steps and 1,000 time steps respectively. All of the simulations used roughly 10,000 atoms, specifically: α-neodymium used 10,976, α-iron used 9,826, and $NdFe_{12}$ used 9,360. The same methodology was followed in all simulations, which can be seen in the diagram presented in Figure 37, the specifics of which are detailed below.

Firstly, the whole structure was raised to the desired temperature and pressure, and allowed to equilibrate in an NPT ensemble for 80,000 time steps (80ps). One half of the simulation was frozen and the other half instantly heated to 8000K in an NVT ensemble for 20,000 time steps (20ps). Springs were applied to the solid liquid interface regions. With the springs applied the frozen and heated part of the system came back into contact and evolved in an NPT ensemble at the desired temperature and pressure. Every 10,000 time steps, the spring constant value was reduced, sequentially taking the following values: 10, 9, 8, 7, 6, 5, 4, 3, 2, 1, 0.5, 0.3, 0.1, 0. In total the springs were in place for 130,000 time steps (130ps). Finally, once the springs were fully removed the system was left to evolve in an NPT ensemble at the desired temperature and pressure

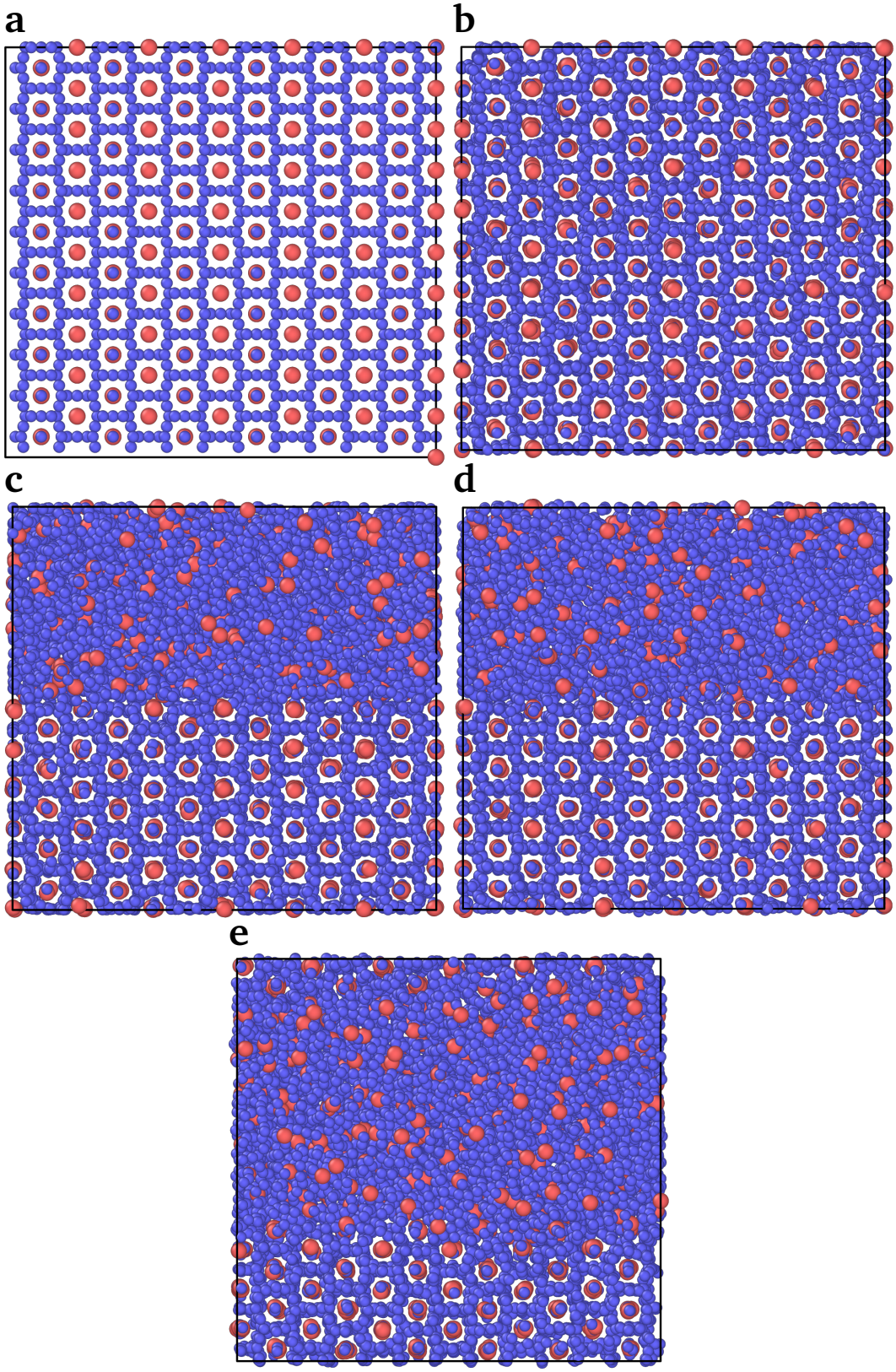

Figure 37: Visualisation of the simulation stages used in the methodology for $NdFe_{12}$, showing a) Initialisation , b) Equilibration of structure to desired pressure and temperature, c) Freezing of the lower half, and catastrophic melting of the upper half, d) Equilibration at the desired pressure and temperature with extra spring constants, and e) System evolution at the desired pressure and temperature - in this case, interface movement into the solid half of the system indicated $T > T_M$.

Material Constant	α-Neodymium (calc.)	α-Neodymium (exp.)	α-Iron (calc.)	α-Iron (exp.)
a (Å)	3.638	3.657[1]	2.8665[1]	2.875
b (Å)	3.638	3.657[1]	2.8665[1]	2.875
c (Å)	5.94	5.902[1]	2.8665[1]	2.875
α (°)	90	90[1]	90	90[1]
β (°)	90	90[1]	90	90[1]
γ (°)	120	120[1]	90	90[1]
E (eV)	-6.823	-6.8[2]	-8.56	-8.56[2]
B (GPa)	33.349	32.7[2]	156.77	170[5]
c_{11} (GPa)	55.038	54.8[3]	167.22	239.26[5]
c_{12} (GPa)	31.41	24.6[3]	151.53	135.78[5]
c_{44} (GPa)	13.614	15.0[3]	151.53	120.72[5]
P (Km/s)	2.66	2.33[4]	5.447	4.91[4]

Table 8: Comparison of the calculated and expected material constants for α-Neodymium and α-Iron. Superscripts [1, 2, 3, 4, 5] represent citations [102, 103, 104, 105, 106].

for 300,000 time steps (300ps).

To assess the interface's movement and establish if the temperature was above, at, or below T_M, each simulation was inspected visually in OVITO[109].

4.3 Method Validation

Potentials

The calculated material constants that were generated by the refit potentials are compared to their expected values in Table 8 and 9. Table 8 shows that the calculated constants with the greatest weighting, lattice parameters and cohesive energy, fit the expected constants very well. Further, it shows large discrepancies only occurred in the elastic constants and associated properties such as the Bulk modulus and longitudinal velocity. This validates the potentials and method, demonstrating both the Nd-Nd and the Fe-Fe potential's ability to reproduce realistic material constants.

Material Constant	Nd_2Fe_{17} (calc.)	Nd_2Fe_{17} (exp.)	$NdFe_{12}$ (calc.)	$NdFe_{12}$ (exp.)
a (Å)	8.597	8.582[1]	8.52	8.52[2]
b (Å)	8.597	8.582[1]	8.52	8.52[2]
c (Å)	12.5536	12.463[1]	4.85	4.80[2]
α (°)	90	90[1]	90	90[2]
β (°)	90	90[1]	90	90[2]
γ (°)	120	120[1]	90	90[2]
E (eV)	-246.4	-248.1	-111.5	-111.3
E (GPa)	227	165[3]	260	165[3]

Table 9: Comparison of the calculated and expected material constants for Nd_2Fe_{17} and $NdFe_{12}$. Superscripts [1, 2, 3] represent citations [107, 49, 108].

Similarly, Table 9 shows very little discrepancy between the calculated and expected constants for Nd_2Fe_{17} and $NdFe_{12}$ in the lattice parameters and cohesive energy, but demonstrates quite significant deviations in the Young's modulus. However, as the expected Young's modulus was chosen to be approximately similar to $Nd_2Fe_{14}B$, deviations from the expected value are neither surprising nor disqualifying. Bearing this in mind, the potential's ability to reproduce known constants from the literature, along with its correct energy preference order, validates its applicability to this study.

Simulation Methodology

To validate the melting simulation methodology it was tested using an Fe-Fe MEAM potential from Etesami et al.[110], which was specifically designed for capturing melting temperature. The methodology calculated the melting temperature to be 1820K$\pm$10K, similar to the 1807K calculated by Etesami et al.[110] and close to the actual melting temperature of 1811K at 1 Bar. This puts the methodology within $\sim$1% of the true melting temperature and validates its applicability to this study.

4.4 Results

Simulations were performed that searched for the melting temperature of the three structures α-Nd, α-Fe, and $NdFe_{12}$. The temperature searches started broad moving over a range of a few hundred kelvin in 50-100K steps, before narrowing down to ranges of 30-50 kelvin in 5-10K steps. The searches resulted in the following calculated melting temperatures at 1 Bar: α-Nd $\sim$1700K$\pm$10K, α-Fe $\sim$3000K$\pm$10K, and $NdFe_{12}$ $\sim$2040K$\pm$10K. Because the hot press sintering technique occurs at temperatures greater than 1 Bar, calculations were also performed that found $NdFe_{12}$'s melting temperature at increased pressures - the results can be seen in Figure 38.

Compared to the melting points given by Kittel[111], the calculated melting temperatures for α-Nd and α-Fe are over estimations by a factor of 1.32, and 1.66 respectively. It is therefore likely that the melting temperature of $NdFe_{12}$ is similarly overestimated. As can be seen from the potentials in Figure 36, the most influential interatomic interactions occur under 7Å, beyond which the energy from interactions is almost negligible. Using 7Å as a cut off point, the number and type of interatomic interactions for each atom in a 3x3x2 supercell of $NdFe_{12}$ were calculated. Within 7 Angstroms Fe-Fe interactions account for 90 times the number of Nd-Nd interactions, and 10 times the number of Nd-Fe interactions. As the temperature over estimation due to the Nd-Fe interaction is harder to quantify, and the Fe-Fe interactions are easily the most dominant, the 1.66 over estimation for α-Fe was used as a guide for the approximate over estimation of the $NdFe_{12}$ melting temperature. The re-scaled melting temperatures can be seen in Figure 38b, giving $NdFe_{12}$ a re-scaled melting point of 1230K$\pm$10K at 1 Bar.

4.5 Discussion

Although the simulations were not capable of accurately producing known single melt temperatures, the calculated melting temperature of 1230K compares well to the known annealing temperature for $NdFe_{11}Ti$ which Zheleznyi et al. give as 1373K[112]. As $NdFe_{11}Ti$ is a higher stability structure, it's expected that the melting point of $NdFe_{12}$

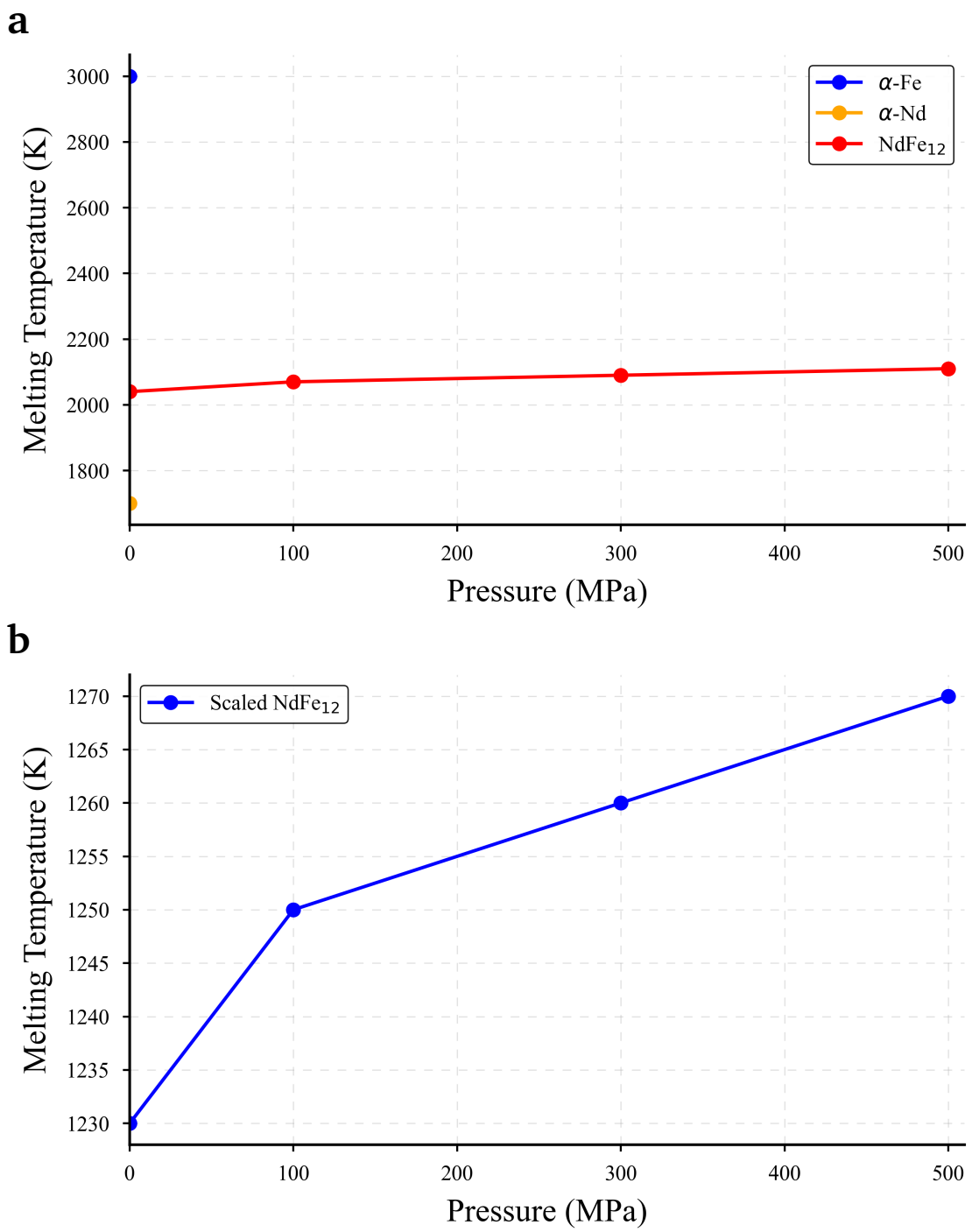

Figure 38: a) Unscaled melting temperatures for α-Fe, and α-Nd at 1 Bar, and $NdFe_{12}$ with pressure, b) Scaled melting temperatures for $NdFe_{12}$ with pressure.

is lower. The calculations suggest that $NdFe_{12}$ is kept below a maximum of 1250K for pressures below 100MPa during the hot press sintering process. As the goal of hot press sintering is to partially melt the material the recommended temperature should be 85-95% of the maximum melting temperature, or ~1060-1190K. Ultimately further and improved simulations along with experimental analysis will be required to understand the best manufacturing method for $NdFe_{12}$.

It's probable the inability of the simulations to reproduce single element melting temperatures has two main causes. Firstly, the amount of data points that were used to fit the potentials, and secondly the potential formalism itself. For the time being, the solid-liquid coexistence methodology is not considered a factor, as it was able to correctly simulate the melting temperature of iron when using the MEAM potential developed by Etesami et al.

To address the first point, future genetic algorithms should rely on a broader range of data points, including both ab initio and experimental results. This will require data being drawn from a broader array of structures, which will prevent the potential being over-fit to any single structure and, in the case of ab initio results, fit the potential to substantially more detailed data - for example, cohesive energy curves.

Examining the difference in accuracy of the MEAM and Morse potentials used here, it's clear that potential formalism is the most likely reason for the poor reproduction of melting temperature. However, this issue is harder to address, as currently there is no best potential formalism within the material simulation community, and potentials are typically changed to match both the material being simulated and the purpose of the simulation. Although potentials such as MEAM are generally considered to be accurate across a broad range of structures, there is significant effort directed towards machine learning potential development [113], and entirely new formalisms. The future of potential development lies in this direction, and future work should encompass one or more of these emerging models.

5 Modelling Grain Growth

5.1 Introduction

As alluded to in the previous chapter's discussion, material science is a developing field. There are tools that have been institutionally developed over the course of decades, for example LAMMPS[61] and GULP[83], relative newcomers for example pymatgen[114], and very recent additions such as the Atomistic Simulation Environment[115] released in 2017. The longevity of the older tools, and the frequency of new releases shows the lasting and increasing importance of computational material research for design and development.

The work in this final chapter has required the development of a new tool, which can offer general solutions to the types of problems answered in this chapter. This means the chapter discusses methodological development, as well as the fundamental research it aided.

This chapter's research question is the following: what drives the shape of grains in bulk solids, what drives their interface pairings, and how can knowledge of these effects be used to predict crystal structure and properties? Although there may be similarities across materials sharing the same lattice structure, answering each of these questions specifically for each material is crucial to understanding and utilising that material, particularly in the case of magnetic materials whose magnetic properties depend heavily on grain dynamics.

The idea for this tool stems from work on FePt $L1_0$ - Permalloy and CoPt $L1_0$ - Permalloy exchange springs magnets[116]. Attempting to understand imprinted domain structures in these materials led to an investigation into what effect their grain morphology and polycrystalline texture have on the properties of the exchange spring. The investigation began with a simple problem: how can Molecular Dynamics be used to calculate the preferential grain morphologies of crystal structures. The work in this chapter is centred around answering this question for a model material: FePt $L1_0$.

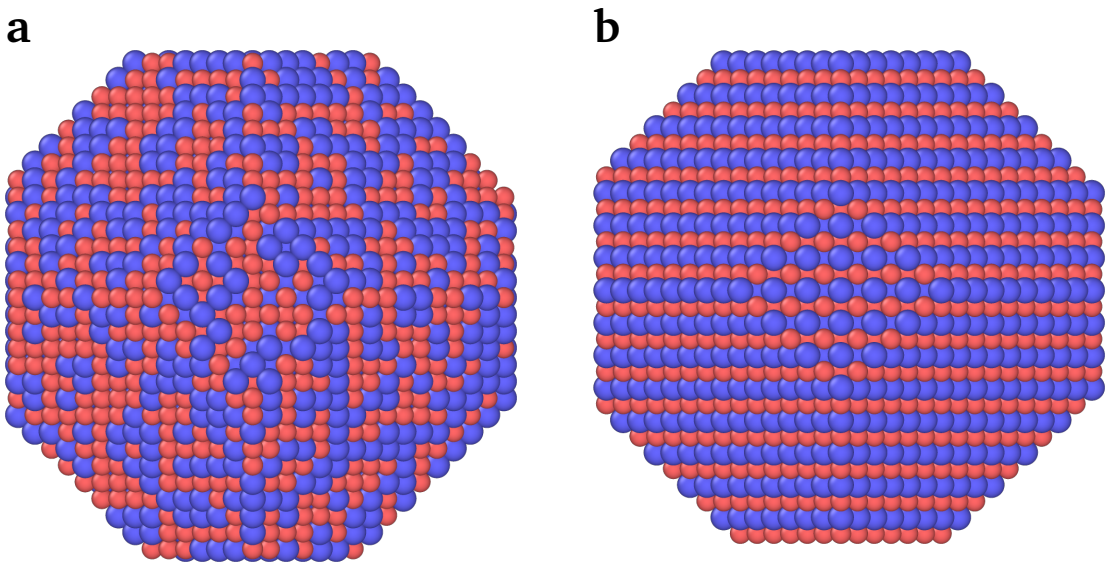

Figure 39: Ordered and disordered FePt grains, showing a) Disorderd FCC A1 FePt, and b) Ordered FCT $L1_0$ FePt.

There were two reasons for the choice of FePt $L1_0$. Firstly, it is a stable alloy in the iron-platinum system that has an extremely high magnetic anisotropy - making it a fantastic candidate for high density perpendicular magnetic recording. Secondly, previous work on exchange spring magnets meant the author already had knowledge of its crystal structure and pair potentials. The structure itself is formed when a randomised cubic (FCC), 50:50 iron and platinum atoms, is heated above a reordering temperature of 600°C[117] causing the iron and platinum atoms to form repeating monolayers in the c direction. This results in a shortening of the c lattice parameter, making it face centred tetragonal (FCT). The reordered crystal develops directionally dependent magnetic properties, giving it a preferential magnetisation direction in its shortened c axis. Figure 39 shows the disordered and ordered state for one such grain.

FePt $L1_0$ has a curie temperature of ∼650K[118], a coercivity of ∼5kOe[119], and most importantly for its applications in hard drive technology, a magnetic anisotropy of $K_u = 6.6 - 10\ MJ/m^3$. It's high anisotropy allows the material to have stable magnetic grains at single digit nanometre sizes (4-6nm), a necessary property for increasing the information density of magnetic hard drives.

Most magnetic materials at these grain sizes are beyond their super-paramagetic limit and thus are incredibly unstable, as random thermal fluctuations at room temperature

are capable of flipping their spin orientation and corrupting data.

Although the high anisotropy of FePt $L1_0$ precludes it from this specific problem, understanding the magnetic dynamics of such a large number of small grains is still a challenging problem, that is currently addressed by microstructurally aware micromagnetics[120] and atomistic modelling[121]. Progressing beyond or improving these methodologies requires new approaches that are capable of accurately capturing structural discontinuities such as surfaces and grain boundaries, because at such small sizes these comprise a far larger percentage of the structures volume. Without proper consideration of these defects, it is difficult to model the grains magnetic behaviour, as magnetic reversal is often nucleated from these discontinuities due to their reduced anisotropy. Understanding the mechanisms of this process will prove key to reliable manufacturing.

As mentioned, it is possible to investigate these effects using continuum model approaches such as micromagnetics, but as grain sizes decrease and surfaces begin to play more of a role a finer grained approach is required. Atomistic magnetic modelling[121] is considered a closer and more accurate approach, focusing magnetic spin and interactions on individual atoms. However, to be accurate, these models require accurate reproductions of underlying atomic structure, a gap the work in this chapter can fill for FePt $L1_0$ presently and any crystal structure in the future generally.

This chapter's method is based on the selection of various grain morphologies, which are used to produce compositionally identical grains. Matching the compostions allows their energetic preferability, and thus their probability, to be compared using Boltzmann factors. The resulting calculations allow for an energetic comparison of different morphologies. Repeating this process over a range of grain sizes gives an insight into the *shape anisotropy* of particular crystal structure as its grains increase in size.

The study resources are given first, with an added section on the methodology used for grain creation, followed by the details of the LAMMPS methodology used for simulating the grains. Methodology validation follows, with results and discussion at the end.

Parameter	Fe	Pt
E_c	4.29	5.77
R_e	2.867	3.92
B	1.08	1.80
A	0.56	0.90
$\beta^{(0)}$	4.15	4.92
$\beta^{(1)}$	1.0	2.2
$\beta^{(2)}$	1.0	6.0
$\beta^{(3)}$	1.0	2.2
$t^{(0)}$	1.0	1.0
$t^{(1)}$	2.6	3.94
$t^{(2)}$	1.8	-2.20
$t^{(3)}$	-7.2	3.84

Table 10: Fundamental MEAM potential parameters for iron and platinum. E_c is the reference structure cohesive energy, R_e is the reference structure equilibrium bond distance, B is the Bulk modulus, A is a model parameter that scales the screening functions, $\beta^{(l)}$ l=0-3 are scaling parameters controlling the form of the original EAM partial electron density functions: $\rho_i^{a(l)}$, and $t^{(l)}$ which scales the contribution of each of the MEAM partial electron densities: $\rho_i^{(l)}$ l=0-3.

5.2 Study Resources

We used Modified Embedded Atom Model (MEAM) potentials taken from a paper by Kim et al.[122]. The potential parameters are shown in Tables 10, and 11. The iron platinum reference structure used for Table 10 was $FePt_3$ of type $L1_2$. For a complete understanding of the MEAM potential please see [123, 124, 125], a brief description of the method, and its constants is given here. MEAM stands for Modified Embedded Atom Model and is a semi-empirical potential model based on the success of Density Functional Theory (DFT). The MEAM formalism treats is based on the EAM formalism which preceded it. Within the EAM, and hence MEAM, methodology, an atom's energy is calculated using the following Equation:

$$E_i = F_k(\rho_i) + \frac{1}{2}\sum_{(j\neq i)} \Phi_{ij}(r_{ij}) \tag{5.1}$$

where E_i is the energy of the ith atom, $F_k(\rho_i)$ is the embedding energy for an atom of type k when it is placed in site i with background electron density ρ_i, ρ_i is the

Parameter	Value
C_{min}(Fe-Fe-Fe)	0.36
C_{max}(Fe-Fe-Fe)	2.80
C_{min}(Pt-Pt-Pt)	1.53
C_{max}(Pt-Pt-Pt)	2.80
C_{min}(Pt-Fe-Fe)	0.36
C_{max}(Pt-Fe-Fe)	2.80
C_{min}(Fe-Pt-Pt)	1.53
C_{max}(Fe-Pt-Pt)	2.80
C_{min}(Fe-Fe-Pt)	0.844
C_{max}(Fe-Fe-Pt)	2.80
C_{min}(Pt-Fe-Pt)	0.844
C_{max}(Pt-Fe-Pt)	2.80
E_c(Fe, Pt)	5.86
R_e(Fe, Pt)	2.781

Table 11: The MEAM potential constants governing interactions between iron and platinum. The C_{min} and C_{max} constants are the maximum and minimum values for the screening functions when atoms are screened by an intervening atom, for example C_{min}(Pt-Fe-Pt) is the maximum screening function due to an iron atom screening the interaction of two platinum interactions. E_c(Fe, Pt) is the energy of the iron - platinum reference structure, and R_e(Fe, Pt) is the equlibirum bond distance of the iron - platinum reference structure.

summation of spherically averaged atomic electron density functions, Φ_{ij} is the pair interaction between atoms i and j, and r_{ij} is the magnitude of the distance between atoms i and j. Therefore, the energy of an atom is due to its interaction with the background electron density and its neighbour interactions through a pair potential. This formalism is termed semi-empirical as its atomic electron densities can be taken from ab initio calculations. The brilliance of this approach is that it allows the formalism to take into account neighbour coordination effects without much increase in computational cost, as the atomic electron densities are a proxy for neighbour coordination. The pair interaction Φ_{ij} can take many different forms and is the empirical part of the formalism that is tailored to match physical constants. As a minimum, it adds the strong repulsion required to prevent atoms getting unphysically close to one another[124].

The background electron density at site i, ρ_i, is calculated by summing the partial electron densities of atoms around the the site. The constants $\beta^{(l)}$, l=0-3, scale the partial electron densities, and $t^{(l)}$, l=0-3, weight the contribution of each of the partial

electron densities to the total atomic electron density. C_{min} and C_{max} are parameters for a screening function that scales the contribution of an atom j's electron density when the vector between the site i and the atom j is partially or fully crossed by another atom k. The screening constants are based on the atomic geometry of the atom, k, and scale the contribution differently depending on how fully the vector is crossed by atom k.

5.3 Methodology Specifics

5.3.1 Grain Creation

Grain Definition

To generalise the grain creation process, a Python module was created that can be used to define abstract grain morphologies. In this module, a grain morphology is defined as the following: a unitcell, a set of cuts, and a repeat ratio. A description of each of these follows:

Unit cell: Basis of the grain, defined by three lattice vectors $\boldsymbol{a}$, $\boldsymbol{b}$, $\boldsymbol{c}$ and a list of constituent atoms in fractional coordinates.

Cuts: Each cut is defined by a plane normal and a plane point, both given in fractional coordinates. For example the cut with normal [111] and plane point (0, 0, 1) would cut along the (111) plane that passes through the point given by the greatest extent of the grain in the $\boldsymbol{c}$ direction.

Repeat Ratio: The repeat ratio defines the ratio between unitcell repeats in the three available directions. For example a repeat ratio of [1, 2, 1] would repeat the unitcell two times in the $\boldsymbol{b}$ direction for every single repeat in the $\boldsymbol{a}$ and $\boldsymbol{c}$ directions.

Taken together, cuts and repeat ratio define a general morphology which can be arbitrarily scaled to any desirable size. To build a grain from this abstract definition an integer scaling factor is used that defines the final size. The scaling factor works in the following ways:

1. Multiplies the repeat ratio to get the final number of unitcell repeats in each direction. For example if the repeat ratio is [1, 2, 1] and you have a scaling factor of 10, the final repetitions in each direction are [10, 20, 10].

2. Multiplies the repeat ratio, which scales the the plane point of each cut. For example if a cut is defined by the plane normal [111] and the plane point (0, 0, 1) and the final number of unitcell repeats is [10, 20, 10] the plane point is scaled to (0, 0, 10).

The unitcell repeats are used to create a supercell of the underlying structure, and the redefined cuts shape the grain into the final morphology.

Composition Matching

For a simple grain that would be the end of the process, but to compare grain preferability by Boltzmann Factors the grains must have identical compositions. This means each grain must consist of the exact same number of atoms, with the exact same ratio of elements. This process requires two or more grain morphologies and starts with the user selection of a target number of atoms. Each grain morphology is used to create a grain using a scale factor that puts it as close as possible, but above, the target number of atoms. Grains in this state are termed "as built".

The ratio of elements in each of the as built grains is calculated and used to define an average composition, termed the best fit composition. For example, if the grains were FePt $L1_0$ the ratios may be 49:51, 49.5:50.5, and 51:49 (Fe:Pt), the average of these is 49.83:50.17, which is used to decide how many of each atom type should be in the grains. Continuing the example, for grains with 10,000 atoms total, this would equate to 4983 iron atoms, and 5017 platinum atoms, this is the best fit composition.

Once the best fit composition has been defined, atoms are progressively deleted from the surface of each of the as built grains in turn until they match the desired composition. Atom deletion has a physical basis and proceeds in rounds that remove atoms in the least energetically favourable positions. Least favourable equates to atoms that have

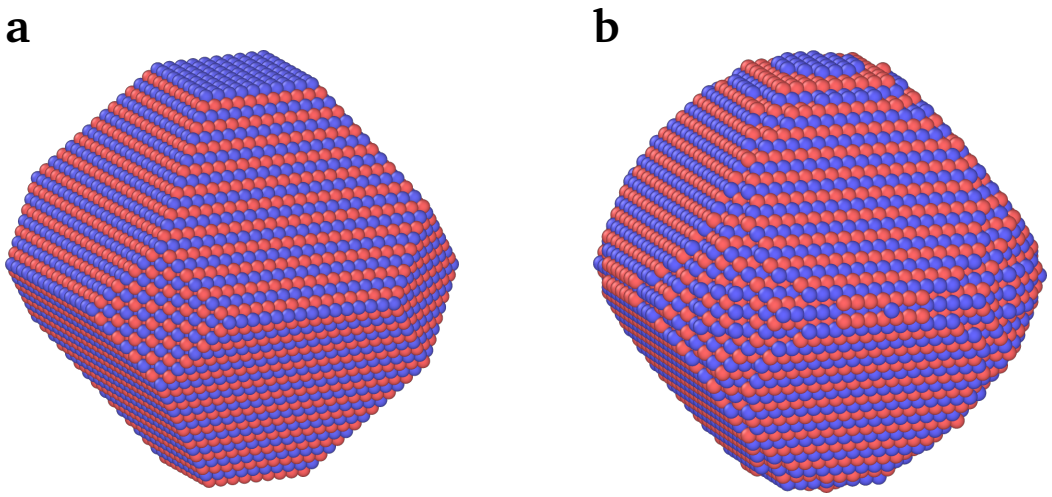

Figure 40: Comparison of a 20,000 atom Truncated Octahedron Minor in its a) As built, and b) Compositionally matched, states.

the lowest number of nearest neighbours and thus the smallest bonding energy. Corner atoms being the least favourable, followed by edge atoms, then general surface atoms, and finally the bulk.

An example of an as built and a compositionally matched final grain can be seen in Figure 40. As the figure shows the as built grain has clean surfaces with defined edges that are due to the cuts used to make it. In contrast the compositionally matched grain has far softer edges and although it maintains the same underlying morphology it is noticeably rounder. Grains created in this manner are physically realistic, as atoms with low binding energy are the first removed and last added.

FePt Grain Morphologies

To choose grain morphologies to test, the surface energies for $L1_0$ from a paper by Kim et al.[126] were used to decide which surfaces would be likely to dominate. The surface energies can be seen in Table 12.

$\{111\}$ surfaces have the lowest energy, whilst the remaining low index planes have roughly similar energies. This comes from the larger number of interplane bonds in the $\{111\}$ planes, which have 6 nearest neighbours instead of 4. From this Kim et al. indicate that the $\{111\}$ planes will predominantly feature on FePt $L1_0$ grains.

Plane	Surface Energy (erg/cm^2)
111	2198
101	2714
110	2650
100	2719
001	2740

Table 12: Surface Energies of low index FePt $L1_0$ planes, taken from Kim et al.[126].

Using this as a basis, all the grain morphologies were created using cuts along the $\{111\}$ planes to expose as much of this preferential surface as possible. As there is little difference between the remaining surface energies the $\{100\}$ and $\{001\}$ planes, which naturally accompany $\{111\}$ plane cuts, were allowed to comprise the remaining grain surfaces. This work looked at three types of grain created in this manner, which were named: Octahedron, Truncated Octahedron Minor, and Truncated Octahedron Major. Two further types of grain were included for comparison a Cuboid, and a Sphere. Creating two extreme grain morphologies served as checks on the model's behaviour, as a cuboid morphology should never be a preferential grain shape and a sphere should only become a preferential grain at sizes far above those simulated in this work - where volume to surface ratio effects dominate. At single to double digit nanometer sizes, energetic preferability should be dominated by surface effects, with volume to surface ratio playing a lesser role. The five grain types can be seen in Figure 41.

An FePt $L1_0$ unitcell was used for each grain with the following parameters: $a = b = 3.83$Å, $c = 3.711$Å, and $\alpha = \beta = \gamma = 90°$[127], where a, b, c are the lattice parameters, and α, β, γ are the angles between them. Every grain went through the initial repeat process described above to create a base supercell. To create the first three (none extreme) grain types the $\{111\}$ plane points were positioned at different distances from the supercell centre. Each grain used two plane points, one in the positive and one in the negative $\boldsymbol{a}$ direction, which represented the plane points for all the $\{111\}$ surface cuts. The points, P_1, and P_2 were chosen so that vectors to the points from the origin had the following property: $|\boldsymbol{P_1}| = |\boldsymbol{P_2}|$. This assured that the as built grains had a symmetrical structure. Figure 42 demonstrates how point placement affects the final

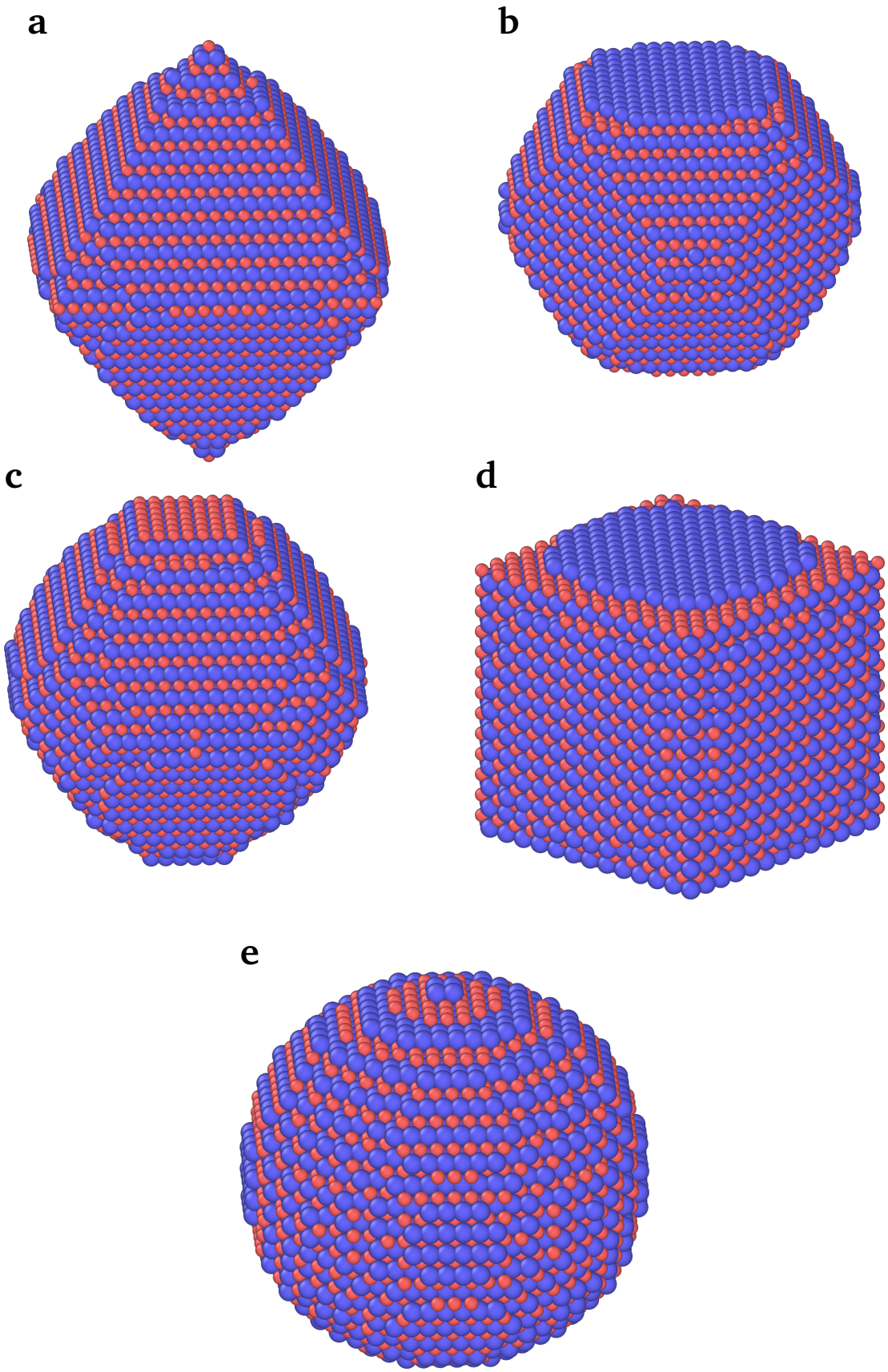

Figure 41: Compositionally matched grain morhpologies at the size of 10,000 atoms. Showing a) Octahedron, b) Truncated Octahedron Major, c) Truncated Octahedron Minor, d) Cuboid, and e) Sphere.

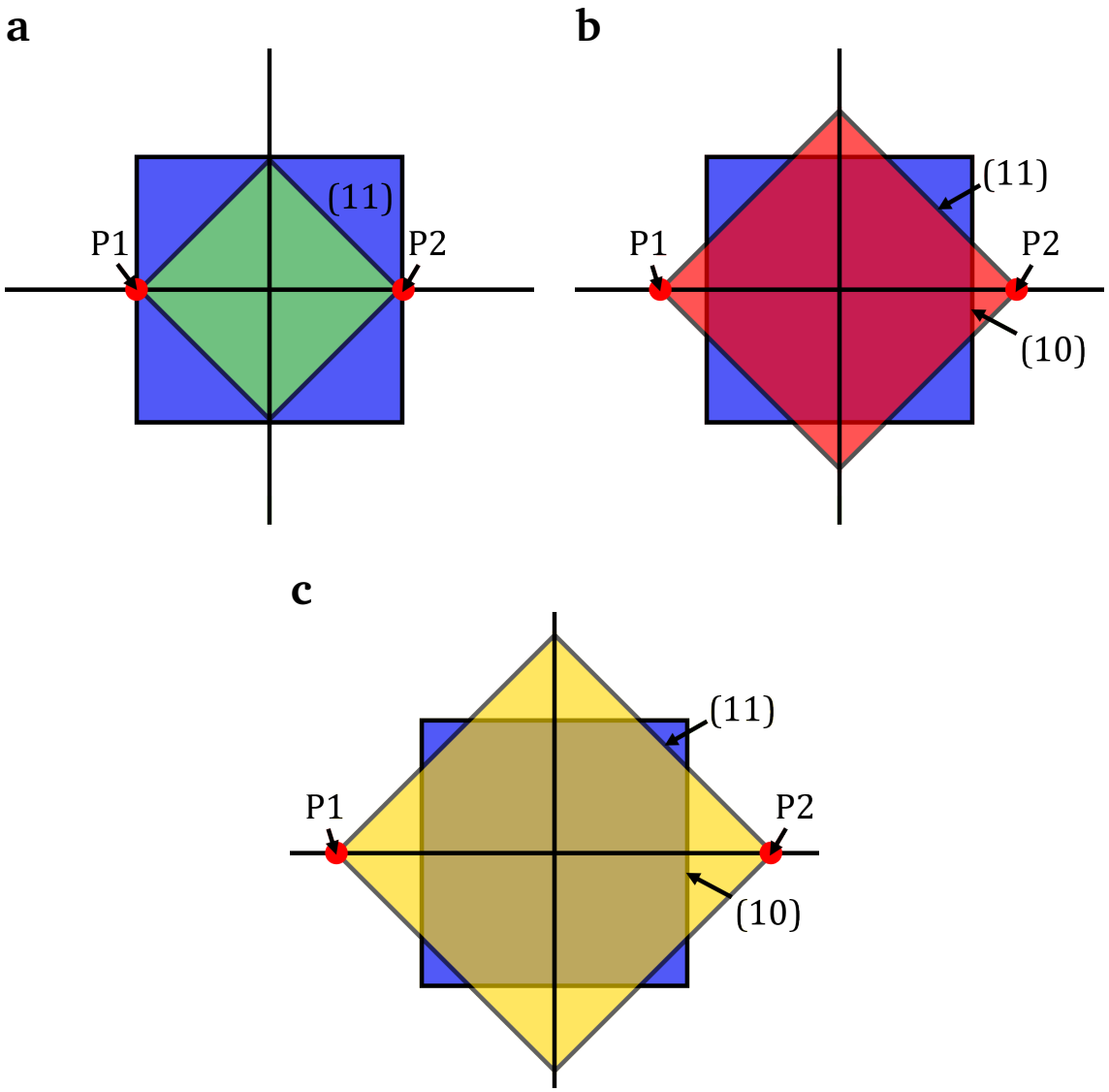

Figure 42: 2D example of how point placement affects grain morphology when cuts are made along the {11} plane set. The blue cube represents the original cubic supercell and the coloured diamonds represent the area left untouched by the {11} cuts. The final grain shape is given by the area of the blue cube that is covered by the coloured diamond. The points which define the placement of cuts are noted in each diagram. The figure shows: a) The 2D representation of the Octahedron shape, b) The 2D representation of the Truncated Octahedron Minor shape, and c) The 2D representation of the Truncated Octahedron Major shape.

shape of the as built grain for a set of simplified 2D cases. As can be seen in Figure 42, the area of the cube covered by the diamond creates a similar grain shape to the 3D cases when projected onto a 2D plane down one of the primary axes. The edges of the diamond passing through the plane points can be thought of as the {11} planes associated with that particular point. In 2D there are only two planes associated with each point, but for the 3D case each point has four {111} planes associated with it.

Plane	Expected Surface Energy (erg/cm^2)	Calculated Surface Energy (erg/cm^2)	Percentage Difference (%)
111	2198	2200	+0.09
101	2714	2685	-1.06
110	2650	2756	+4.00
100	2719	2449	-9.93
001	2740	2919	+6.53

Table 13: Surface Energies of low index FePt $L1_0$ planes, taken from Kim et al.[126], and the values calculated with the potentials used in this work.

5.3.2 Simulation Methodology

Final grain energies were gained by minimisation in LAMMPS, but in order to maximise the chances the minimisation algorithm reached a global not local minimum, the system underwent an initial equilibration phase in the isobaric-isothermal (NPT) ensemble. The NPT ensemble was set at 1K with a pressure of 0Pa and evolved the system over 15,000 time steps, with a time step length of 0.001ps this phase lasted 15ps. This was followed by minimisation, which occurred over a minimum of 10,000 time steps to ensure the system converged on a global energy minimum. Generally, convergence was reached much sooner.

5.4 Method Validation

Potentials

The accuracy of the potentials was validated by calculating the surface energies of the same planes as Kim et al.[126]. The results of this can be seen in Table 13. The potentials are in good agreement with the values reported by Kim et al. in the (111), (101) and (110) planes, however they differ more significantly in the (100) and (001) planes. Kim et al. do not give their surface calculation methods, so it's possible this discrepancy is partially due to a difference in the surface calculation procedure. The surface calculations performed in this work used two methodologies. The (001) and (100) plane calculations used periodic boundary conditions and a supercell that was

periodic across two of the lattice directions, with vacuum in the remaining direction. The vacuum stopped interaction between the two sides of the slab and thus created two surfaces. By comparing the energy of this structure to the expected energy in the bulk and dividing by two the surface energy for a single side was gained. Dividing this energy by the area of a side gave the surface energy of the slab.

For the remaining planes: (111), (101), and (110) supercells of $L1_0$ were created and rotated so that the desired plane's normal was in the cartesian z direction. The rotated cuboid had a slab cut out of it. Cutting a large slab ensured that the centre of the slab had the same energy as the crystal in bulk, and similarly that the surface above it was unaffected by the edge effects that arise from a lack of periodicity. Calculating the energy of this region only and comparing it to the bulk energy resulted in a surface energy for this region.

Although the discrepancy between the expected and calculated results for (100) and (001) raise questions of statistical significance, the overall trend of the surface energies is similar to that given by Kim et al. Therefore, whilst paying careful attention to what effect the (100) and (001) plane discrepancies might have, the potentials were deemed appropriate for the calculations.

Simulation Methodology

To gauge how long the initial equilibration phase should be for optimal energy convergence, tests were performed over a range of equilibration values. Figure 43 shows how the minimum energy changes for the Octahedron, the Truncated Octahedron Major, and the Truncated Octahedron Minor over a range of equilibration values. The figure shows how initial equilibration length affected the final minimised energy of the structure as a percentage of the minimum energy found across the range. For example, for the 1,000 atom Octahedron grain morphology the minimum energy is found at 10,000 time steps (Figure 43a), and thus at this point the graph shows a y axis value of 100%, all other energy values are given as a percentage of this value. The tests showed two things, firstly, that in all cases the difference in final energy due to equilibration times is min-

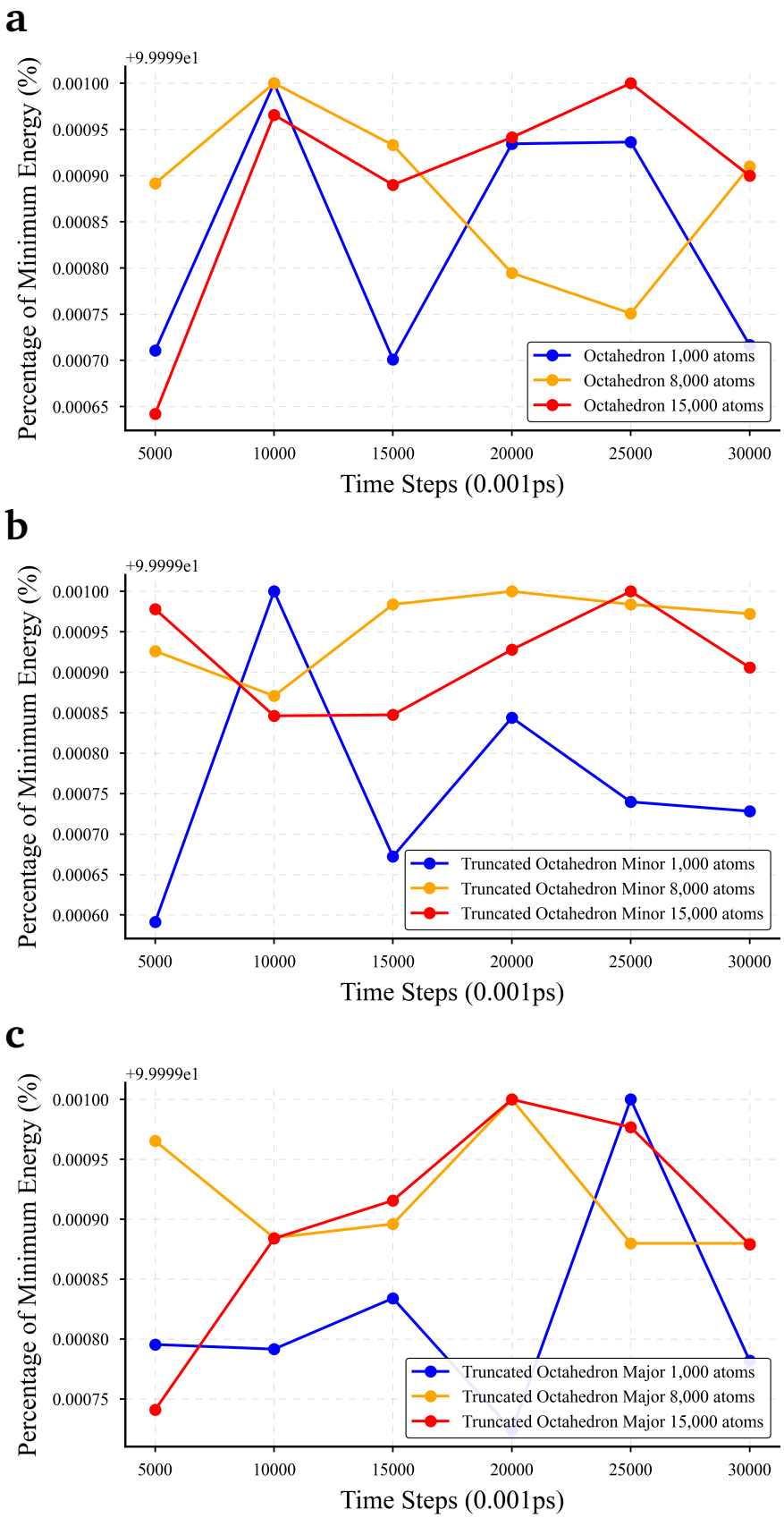

Figure 43: Percentage of minimum energy reached vs the number of initial NPT simulation time steps, for a) Octahedron, b) Truncated Octahedron Minor, and c) Truncated Octahedron Major at 1,000, 8,000, and 15,000 atoms. The value above the y-axis (=99.999) should be added to each y tick.

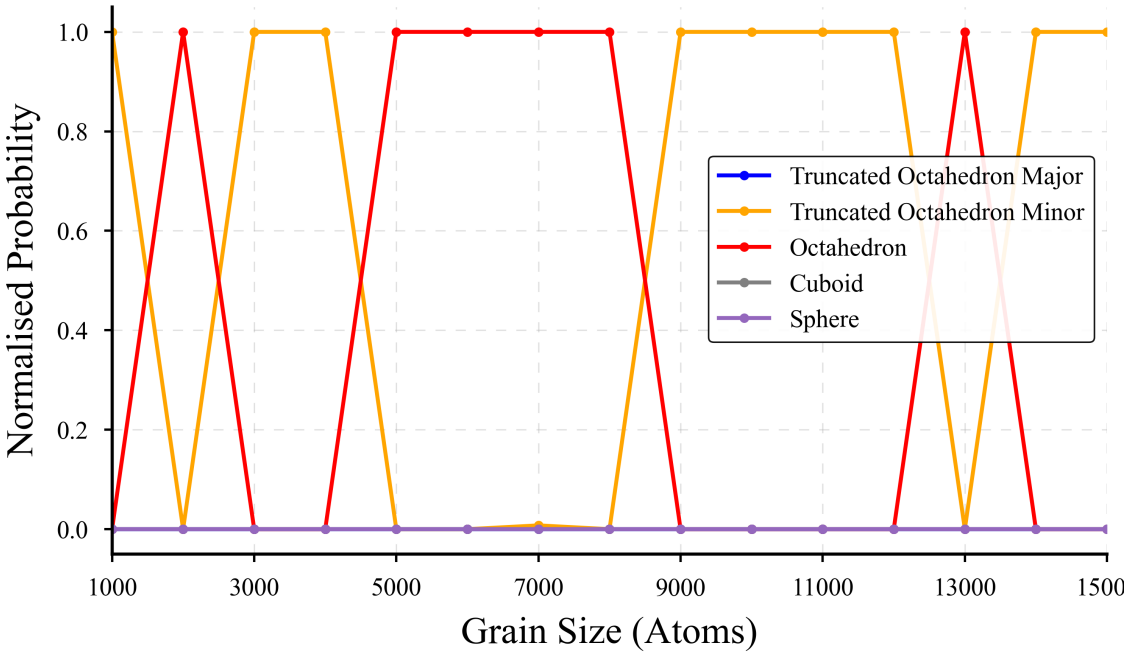

Figure 44: Normalised probabilities based on the structures' Boltzmann factor ratios over a range of 1,000 - 15,000 atoms.

imal, the maximum difference being 0.0004%. Secondly, that there is no trend across the investigated range, which was extended to 400,000 time steps for some structures - not shown in Figure 43. Therefore, 15,000 time steps was the chosen period for this initial phase as a middle value that was likely to provide reasonable minimised energies without large computational expense.

5.5 Results

A range of grain sizes were created for each morphology, ranging from 1,000 to 15,000 atoms in steps of 1,000, equating to grain diameter ranges of 3-9nm. As mentioned the grains were compositionally matched at every stage, which allowed their probabilities to be compared by their Boltzmann factors. Figure 44 shows the comparison between the grains as they increase in size. The figure shows that two of the structures, the Octahedron and the Truncated Octahedron Minor, have the highest probability. Visual inspection of their surfaces shows they have the highest percentage of $\{111\}$ surfaces, the lowest energy plane. Being compositionally identical the surface of these structures is the only thing which separates them from one another energetically. Therefore, prefer-

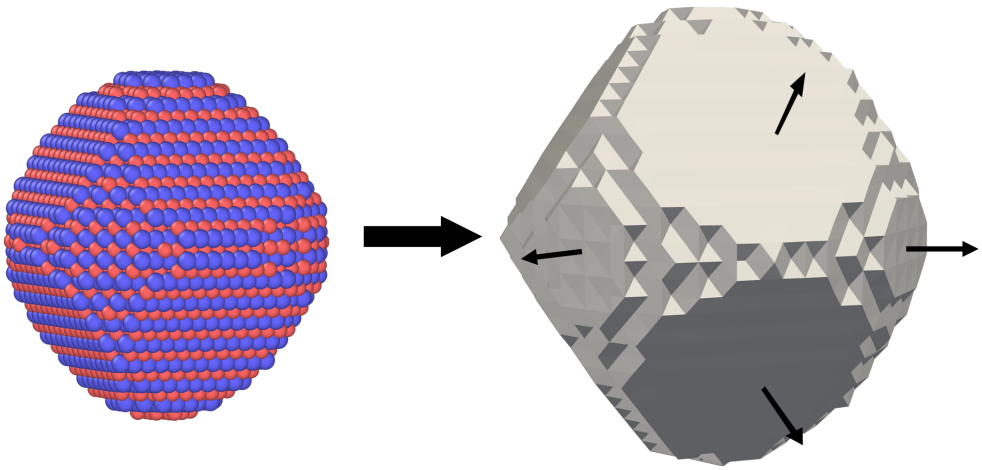

Figure 45: Left) Atomistic visualisation of an FePt L10 Truncated Octahedron Minor grain, Right) Surface of the grain extracted by PyVista, arrows out of the surfaces indicating the plane normals.

able grain morphology can be understood by analysing the differences in their surface structure.

The PyVista package[128], which is a wrapper around VTK[129], was used to build a mesh of the surface of each of the grains. Figure 45 shows this process for a Truncated Octahedron Minor. VTK's Delaunay triangulation function[130] was used to tetrahedralise the atomic point sets before extracting the surface from the resulting geometry. The surfaces are collections of 2D simplexes, each composed of three points. By finding the surface normal and the area of each of these simplexes, they were placed into group corresponding to the surface plane they represented. This gave a total area for each plane set that the structure was composed of. Multiplying the total area by the calculated surface energies above meant the surface energy of each of the grains could be calculated.

Figure 46 shows the surface energy of each grain across the investigated range normalised by the lowest surface energy of the grains at each atomic size.

This graph shows the expected trend, the Octahedron and the Truncated Octahedron Minor, in general, have significantly lower surface energy than the other structures. The Cuboid has by far the most energy at all points, as expected from its lack of $\{111\}$

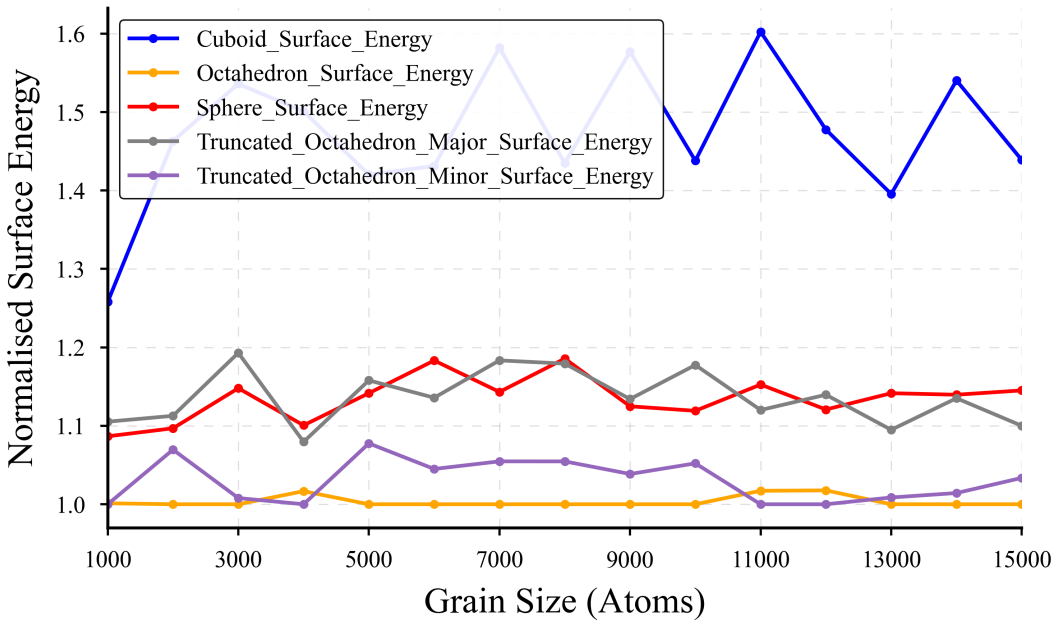

Figure 46: Normalised surface energies of the investigated grains, across the range 1,000-15,000 atoms. The normalisation is different at each atom size, with the normalising value being the grain with the lowest surface energy at each point.

surface planes, followed by the Sphere and the Truncated Octahedron Major which generally have a similar surface energy also. The similarity of the surface energies of the Sphere and the Truncated Octahedron Major is likely due to a difference in the total surface area of the structures as oppose to a similarity in plane surfaces.

5.6 Discussion

The vacuum calculations and subsequent surface analysis demonstrate that grain morphologies of FePt $L1_0$ at small sizes should be dominated by morphologies that incorporate the maximum amount of the $\{111\}$ plane surfaces. Therefore, this plane, and the corresponding grain morphologies it tends to create, should be investigated further to judge its effect on the structure's magnetic properties.

An issue with the methodology in its current formation is its inability to predict, from surface energy alone, which compositionally matched grain is the most preferential. Ideally the surface energy calculations should perfectly follow the preferability of the grains, however, comparison of Figures 44 and 46 will demonstrates this isn't the case,

despite the fact the only energetic difference between the grains in a vacuum should be their surface energies. This is likely due to the surface extraction method, which currently is unable to capture surface planes such as $\{101\}$ and $\{110\}$ accurately. This short coming results in an over-inflation of the surface area of structures with a larger amount of these planes. As the Truncated Octahedron Minor has a larger amount of these than the Octahedron, that is probably the dominating factor preventing the surface energy calculation following the pattern of preferential grain morphology shown in Figure 44.

Despite this shortcoming, with improvement, this methodology could be used generally to find the preferential grain morphologies of any crystal structure. In the future, it will be used to produce a baseline understanding of grain morphology that allows for the creation of accurate atomistic models of polycrystalline materials. This will involve investigating not just the structure of interest, but tertiary structures of a similar phase that often surround it - in the case of FePt $L1_0$ the FCC A1 structure. The end goal of this project is to reproduce accurate atomistic polycrystalline models which could be used as input to micromagnetics, or atomistic spin dynamics simulations.

6 Conclusions

6.1 Summary

The work undertaken in this thesis all drives at a singular goal, developing generally applicable methods for analysing magnetic crystal structures. The first results chapter focuses on one of the most interesting sets of materials at the world's present stage of magnetic material development: RT_{12} structures. The fundamental insight of the research is driven by a high throughput methodology which allows for investigation of the preferential position of substitutions in crystal structures. The result of this methodology was a large amount of high quality data, which could be anaylsed to explain physically why titanium substitutions are energetically unfavourable above a set percentage, which is governed by the symmetry of the crystal structure. This insight has led to a recent talk at the IOP York Magnetism conference and will be the subject of a future paper on the stability of the RT_{12} phases investigated in this work. Whilst an important result, of equal importance is the applicability of the methodology to any other crystal structure.

In the second results chapter on the melting point of $NdFe_{12}$, the most theoretically promising of the three structures, genetic algorithms were used to refit Morse potentials to material constants from the literature. Whilst this resulted in a decrease in the calculated melting temperatures, it was also a first step into the methodology of potential fitting. The work predicted an upper limit for the sintering temperature of $NdFe_{12}$ grains of 1250K, below 100Mpa. But perhaps more importantly, it led to an interest in potential morphologies beyond Morse and the methodologies required to make sure models represent reality - for example, the machine learning potentials presented by Mueller et al.[113].

The last two chapters lead up to the final results chapter, which focuses explicitly on the early stages of the development of a set of methodologies for predicting crystal grain morphology. The methodology showed that FePt $L1_0$ grains have a strong preference for $\{111\}$ surface planes, and will generally adopt morphologies that maximise this surface.

Analysis of the total surface area of each grain, across a range of sizes as a function of atomic number, showed that the order of morphological preference was tied to surface energy. The work suggests that 3-9nm FePt $L1_0$ grains will have morphologies close to an octrahedron or minorly truncated octahedron.

6.2 Future Work

6.2.1 Tool Development

Although Chapters 3 and 4 have resulted in several publications [1, 2, 3], it is the authors belief that the final chapter and the continued development of the materials science tool is where the future of this work lies. The plan for the tool is to tie together the methodologies used in this work, making common work flows in materials science as simple as writing a few lines of Python code.

Future work will look to incorporate generalised potential fitting methods, ab initio calculations, realistic polycrystalline structures, high throughput surface and interface calculations, and phase comparison models which predict the secondary and tertiary phases in polycrystalline materials. These added features will make it quick and easy to produce high quality models in minutes and are intended to provide a "as few clicks as possible" solution to a few of material science's trickiest research problems - e.g. physically accurate polycrystalline models, fast and general surface calculations, and fast and general interface calculations. The tool's goal is to provide useful abstraction to those who need it and powerful effective scripting to those who want it. The tool has recently been open-sourced and can be found on Github through the following link: https://github.com/Connor56/Grain_Modeller

References

[1] Connor Skelland et al. "Probability distribution of substituted titanium in RT 12 (R= Nd and Sm; T= Fe and Co) structures". In: *IEEE Transactions on Magnetics* 54.11 (2018), pp. 1–5.

[2] C Skelland et al. "The Effect of Interstitial Nitrogen Addition on the Structural Properties of Supercells of NdFe 12-x Ti x". In: *IEEE Transactions on Magnetics* 55.10 (2019), pp. 1–5.

[3] C Skelland et al. "Atomistic study on the pressure dependence of the melting point of NdFe12". In: *AIP Advances* 10.2 (2020), p. 025130.

[4] Department of Energy Climate Change. *The UK renewable energy strategy*. Her Majesties Government, 2009.

[5] Technology Research Association of Magnetic Materials for High-Efficiency Motors (MagHEM). *MagHEM collaboration website*. 2020. URL: `https://web.archive.org/web/20200331104145/http://maghem.jp/english/about.html` (visited on 03/31/2020).

[6] Bernard Dennis Cullity and Chad D Graham. *Introduction to magnetic materials*. John Wiley & Sons, 2009, p. 87.

[7] David Jiles. *Introduction to magnetism and magnetic materials*. Chapman and Hall, 1998, p. 89.

[8] Bernard Dennis Cullity and Chad D Graham. *Introduction to magnetic materials*. John Wiley & Sons, 2009, p. 116.

[9] Bernard Dennis Cullity and Chad D Graham. *Introduction to magnetic materials*. John Wiley & Sons, 2009, p. 151.

[10] Bernard Dennis Cullity and Chad D Graham. *Introduction to magnetic materials*. John Wiley & Sons, 2009, p. 175.

[11] James Alfred Ewing. "X. Experimental researches in magnetism". In: *Philosophical Transactions of the Royal Society of London* 176 (1885), pp. 523–640.

[12] John Hopkinson. "IV. Magnetism and recalescence". In: *Proceedings of the Royal Society of London* 48.292-295 (1891), pp. 442–446.

[13] George Frederick Charles Searle and Thomas George Bedford. "II. The measurement of magnetic hysteresis". In: *Philosophical Transactions of the Royal Society of London. Series A, Containing Papers of a Mathematical or Physical Character* 198.300-311 (1902), pp. 33–104.

[14] David Jiles. *Introduction to magnetism and magnetic materials*. Chapman and Hall, 1998, p. 97.

[15] David Jiles. *Introduction to magnetism and magnetic materials*. Chapman and Hall, 1998, p. 325.

[16] Bernard Dennis Cullity and Chad D Graham. *Introduction to magnetic materials*. John Wiley & Sons, 2009, p. 440.

[17] Kurt Hoselitz. *Ferromagnetic properties of metals and alloys*. Clarendon Press, 1952, pp. 257–262.

[18] George Krauss. "Deformation and fracture in martensitic carbon steels tempered at low temperatures". In: *Metallurgical and Materials Transactions B* 32.2 (2001), pp. 205–221.

[19] Kurt Hoselitz. *Ferromagnetic properties of metals and alloys*. Clarendon Press, 1952, p. 263.

[20] Kotaro Honda and Shozo Saito. "On KS magnet steel". In: *The Journal of the Institute of Electrical Engineers of Japan* 40.380 (1920), pp. 201–207.

[21] Kurt Hoselitz. *Ferromagnetic properties of metals and alloys*. Clarendon Press, 1952, p. 263.

[22] Keisuke Fujisaki. *Magnetic Material for Motor Drive Systems*. Springer, 2019, pp. 269–271.

[23] R. A. McCurrie. *The Structure and Properties of Ferromagnetic Materials*. Academic Press, 1994, pp. 203–211.

[24] Albert James Bradley and u A Taylor. "An X-ray analysis of the nickel-aluminium system". In: *Proceedings of the Royal Society of London. Series A-Mathematical and Physical Sciences* 159.896 (1937), pp. 56–72.

[25] CE Webb. "Recent developments in magnetic materials". In: *Journal of the Institution of Electrical Engineers* 82.495 (1938), pp. 303–324.

[26] R. A. McCurrie. *The Structure and Properties of Ferromagnetic Materials*. Academic Press, 1994, p. 204.

[27] DA Oliver and JW Shedden. "Cooling of permanent magnet alloys in a constant magnetic field". In: *Nature* 142.3587 (1938), pp. 209–209.

[28] R. A. McCurrie. *The Structure and Properties of Ferromagnetic Materials*. Academic Press, 1994, p. 210.

[29] R. A. McCurrie. *The Structure and Properties of Ferromagnetic Materials*. Academic Press, 1994, p. 207.

[30] Kurt Hoselitz. *Ferromagnetic properties of metals and alloys*. Clarendon Press, 1952, p. 271.

[31] JD Livingston. "The history of permanent-magnet materials". In: *JOM* 42.2 (1990), pp. 30–34.

[32] Norman N Greenwood and A Earnshaw. *Chemistry of the Elements 2nd Edition*. Butterworth-Heinemann, 1997, pp. 1079–1081.

[33] R. A. McCurrie. *The Structure and Properties of Ferromagnetic Materials*. Academic Press, 1994, p. 124.

[34] V DROINA and R Janus. "A new magnetic alloy with very large coercitive force". In: *Nature* 135.3401 (1935), pp. 36–37.

[35] W Mo Hubbard, E Adams, and JV Gilfrich. "Magnetic moments of alloys of gadolinium with some of the transition elements". In: *Journal of Applied Physics* 31.5 (1960), S368–S369.

[36] Karl Strnat et al. "A family of new cobalt-base permanent magnet materials". In: *Journal of Applied Physics* 38.3 (1967), pp. 1001–1002.

[37] MG Benz and DL Martin. "COBALT-SAMARIUM PERMANENT MAGNETS PREPARED BY LIQUID PHASE SINTERING". In: *Applied Physics Letters* 17.4 (1970), pp. 176–177.

[38] KHJ Buschow, AM Van Diepen, and HW De Wijn. "Crystal-field anisotropy of Sm3+ in SmCo5". In: *Solid State Communications* 15.5 (1974), pp. 903–906.

[39] Yoshio Tawara and Karl Strnat. "Rare earth-cobalt permanent magnets near the 2-17 composition". In: *IEEE Transactions on Magnetics* 12.6 (1976), pp. 954–958.

[40] Harufumi Senno and Yoshio Tawara. "Magnetic properties of Sm-Co-Fe-Cu alloys for permanent magnet materials". In: *Japanese Journal of Applied Physics* 14.10 (1975), p. 1619.

[41] KJ Strnat and AE Ray. "Evidence for new magnetic rare earth-cobalt phases". In: *AIP Conference Proceedings*. Vol. 24. 1. American Institute of Physics. 1975, pp. 680–681.

[42] Masato Sagawa et al. "New material for permanent magnets on a base of Nd and Fe". In: *Journal of Applied Physics* 55.6 (1984), pp. 2083–2087.

[43] Masato Sagawa et al. "Nd–Fe–B permanent magnet materials". In: *Japanese journal of applied physics* 26.6R (1987), p. 785.

[44] D Haskel et al. "Atomic origin of magnetocrystalline anisotropy in Nd 2 Fe 14 B". In: *Physical review letters* 95.21 (2005), p. 217207.

[45] Simon Bance et al. "Grain-size dependent demagnetizing factors in permanent magnets". In: *Journal of Applied Physics* 116.23 (2014), p. 233903.

[46] TG Woodcock et al. "Understanding the microstructure and coercivity of high performance NdFeB-based magnets". In: *Scripta Materialia* 67.6 (2012), pp. 536–541.

[47] DB De Mooij and KHJ Buschow. "Some novel ternary ThMn12-type compounds". In: *Journal of the Less common Metals* 136.2 (1988), pp. 207–215.

[48] Ying-chang Yang et al. "Magnetocrystalline anisotropies of RTiFe11N x compounds". In: *Applied physics letters* 58.18 (1991), pp. 2042–2044.

[49] Takashi Miyake et al. "First-principles study of magnetocrystalline anisotropy and magnetization in NdFe12, NdFe11Ti, and NdFe11TiN". In: *Journal of the Physical Society of Japan* 83.4 (2014), p. 043702.

[50] Y Hirayama et al. "NdFe12Nx hard-magnetic compound with high magnetization and anisotropy field". In: *Scripta Materialia* 95 (2015), pp. 70–72.

[51] Y Hirayama et al. "Intrinsic hard magnetic properties of Sm (Fe1- xCox) 12 compound with the ThMn12 structure". In: *Scripta Materialia* 138 (2017), pp. 62–65.

[52] Nicholas Metropolis and Stanislaw Ulam. "The monte carlo method". In: *Journal of the American statistical association* 44.247 (1949), pp. 335–341.

[53] E Fermi, J Pasta, and S Ulam. *Report LA-1940. Studies of nonlinear problems. I.* Tech. rep. I. Tech. rep., Los Alamos Scientific Laboratory, 1955.

[54] Berni J Alder and Thomas Everett Wainwright. "Studies in molecular dynamics. I. General method". In: *The Journal of Chemical Physics* 31.2 (1959), pp. 459–466.

[55] Aneesur Rahman. "Correlations in the motion of atoms in liquid argon". In: *Physical review* 136.2A (1964), A405.

[56] Llewellyn H Thomas. "The calculation of atomic fields". In: *Mathematical proceedings of the Cambridge philosophical society*. Vol. 23. 5. Cambridge University Press. 1927, pp. 542–548.

[57] Pierre Hohenberg and Walter Kohn. "Inhomogeneous electron gas". In: *Physical review* 136.3B (1964), B864.

[58] Mel Levy. "Universal variational functionals of electron densities, first-order density matrices, and natural spin-orbitals and solution of the v-representability problem". In: *Proceedings of the National Academy of Sciences* 76.12 (1979), pp. 6062–6065.

[59] Richard Car and Mark Parrinello. "Unified approach for molecular dynamics and density-functional theory". In: *Physical review letters* 55.22 (1985), p. 2471.

[60] Andrew Motte Isaac Newton. *Newton's Principia the Mathematical Principles of Natural Philosophy*. David Adee, 1729, p. 393.

[61] Steve Plimpton. "Fast parallel algorithms for short-range molecular dynamics". In: *Journal of computational physics* 117.1 (1995), pp. 1–19.

[62] Dennis C Rapaport. *The art of molecular dynamics simulation*. Cambridge university press, 2004.

[63] Daan Frenkel and Berend Smit. *Understanding molecular simulation: from algorithms to applications*. Vol. 1. Elsevier, 2001.

[64] Li Mubin and Plimpton. *Extending and Modifying LAMMPS Writing Your Own Source Code: A pragmatic guide to extending LAMMPS as per custom simulation requirements*. Vol. 1. Packt, 2021.

[65] Daan Frenkel and Berend Smit. *Understanding molecular simulation: from algorithms to applications*. Vol. 1. Elsevier, 2001, pp. 63–64.

[66] P. Giannozzi. *Introduction to the calculation of phonons and of vibrational spectra*. Cambridge. Sept. 23, 2009. URL: https://www.tcm.phy.cam.ac.uk/~jry20/gipaw/tutorial_vib.pdf (visited on 07/01/2022).

[67] Stephen J Blundell and Katherine M Blundell. *Concepts in thermal physics*. Oup Oxford, 2009, p. 37.

[68] John Edward Jones. "On the determination of molecular fields.—I. From the variation of the viscosity of a gas with temperature". In: *Proceedings of the Royal Society of London. Series A, Containing Papers of a Mathematical and Physical Character* 106.738 (1924), pp. 441–462.

[69] Philip M Morse. "Diatomic molecules according to the wave mechanics. II. Vibrational levels". In: *Physical review* 34.1 (1929), p. 57.

[70] Dennis C Rapaport. *The art of molecular dynamics simulation*. Cambridge university press, 2004, pp. 11–13.

[71] Daan Frenkel and Berend Smit. *Understanding molecular simulation: from algorithms to applications*. Vol. 1. Elsevier, 2001, p. 32.

[72] Dennis C Rapaport. *The art of molecular dynamics simulation*. Cambridge university press, 2004, p. 17.

[73] Dennis C Rapaport. *The art of molecular dynamics simulation*. Cambridge university press, 2004, p. 17.

[74] Daan Frenkel and Berend Smit. *Understanding molecular simulation: from algorithms to applications*. Vol. 1. Elsevier, 2001, pp. 69–71.

[75] Hans C Andersen. "Molecular dynamics simulations at constant pressure and/or temperature". In: *The Journal of chemical physics* 72.4 (1980), pp. 2384–2393.

[76] Shuichi Nosé. "A unified formulation of the constant temperature molecular dynamics methods". In: *The Journal of chemical physics* 81.1 (1984), pp. 511–519.

[77] Jos Thijssen. *Computational physics*. Cambridge university press, 2007, pp. 226–227.

[78] John Henry Holland et al. *Adaptation in natural and artificial systems: an introductory analysis with applications to biology, control, and artificial intelligence*. MIT press, 1992.

[79] Darrell Whitley. "A genetic algorithm tutorial". In: *Statistics and computing* 4.2 (1994), pp. 65–85.

[80] Yong Zhang and Edward J Maginn. "A comparison of methods for melting point calculation using molecular dynamics simulations". In: *The Journal of chemical physics* 136.14 (2012), p. 144116.

[81] James R Morris et al. "Melting line of aluminum from simulations of coexisting phases". In: *Physical Review B* 49.5 (1994), p. 3109.

[82] James R Morris and Xueyu Song. "The melting lines of model systems calculated from coexistence simulations". In: *The Journal of chemical physics* 116.21 (2002), pp. 9352–9358.

[83] Julian D Gale and Andrew L Rohl. "The general utility lattice program (GULP)". In: *Molecular Simulation* 29.5 (2003), pp. 291–341.

[84] JD Gale. "GULP manual Version 5.2". In: *GULP manual* (2019).

[85] David F Shanno. "Conditioning of quasi-Newton methods for function minimization". In: *Mathematics of computation* 24.111 (1970), pp. 647–656.

[86] Amparo Gil, Javier Segura, and Nico M Temme. *Numerical methods for special functions*. SIAM, 2007, p. 193.

[87] Roger Fletcher and Michael JD Powell. "A rapidly convergent descent method for minimization". In: *The computer journal* 6.2 (1963), pp. 163–168.

[88] Nocedal Jorge and J Wright Stephen. *Numerical optimization*. Spinger, 2006, p. 31.

[89] Stephen J Blundell and Katherine M Blundell. *Concepts in thermal physics*. Oup Oxford, 2009, p. 39.

[90] Hamed Rahimi et al. "The role of dysprosium on the structural and magnetic properties of (Nd1- xDyx) 2Fe14B nanoparticles". In: *Journal of Magnetism and Magnetic Materials* 424 (2017), pp. 199–206.

[91] Sander Hoenderdaal et al. "Can a dysprosium shortage threaten green energy technologies?" In: *Energy* 49 (2013), pp. 344–355.

[92] F.R. De Boer et al. "Magnetic properties of a series of novel ternary intermetallics (RFe10V2)". In: *Journal of the Less Common Metals* 135.2 (1987), pp. 199–204. ISSN: 0022-5088. DOI: https://doi.org/10.1016/0022-5088(87)90481-4. URL: https://www.sciencedirect.com/science/article/pii/0022508887904814.

[93] Nan-xian Chen. "Modified Möbius inverse formula and its applications in physics". In: *Physical review letters* 64.11 (1990), p. 1193.

[94] WQ Wang et al. "Structural and magnetic properties of RCo12-xTix (R= Y and Sm) and YFe12-xTix compounds". In: *Journal of Physics D: Applied Physics* 34.3 (2001), p. 307.

[95] KHJ Buschow. "New developments in hard magnetic materials". In: *Reports on Progress in Physics* 54.9 (1991), p. 1123.

[96] I Dirba et al. "Thermal decomposition of ThMn12-type phase and its optimum stabilizing elements in SmFe12-based alloys". In: *Journal of Alloys and Compounds* 813 (2020), p. 152224.

[97] David Brown, Bao-Min Ma, and Zhongmin Chen. "Developments in the processing and properties of NdFeb-type permanent magnets". In: *Journal of magnetism and magnetic materials* 248.3 (2002), pp. 432–440.

[98] XH Zhang et al. "Effect of process on the magnetic and mechanical properties of Nd–Fe–B bonded magnets". In: *Materials & Design* 30.4 (2009), pp. 1386–1390.

[99] Simon R Phillpot, Sidney Yip, and Dieter Wolf. "How do crystals melt? Computer simulations demonstrate the interplay between thermodynamics and kinetics during the melting process". In: *Computers in physics* 3.6 (1989), pp. 20–31.

[100] Jan Solca et al. "Melting curves for neon calculated from pure theory". In: *The Journal of chemical physics* 108.10 (1998), pp. 4107–4111.

[101] 9_H Balamane, T Halicioglu, and WA Tiller. "Comparative study of silicon empirical interatomic potentials". In: *Physical Review B* 46.4 (1992), p. 2250.

[102] Ralph Walter Graystone Wyckoff and Ralph WG Wyckoff. *Crystal structures*. Vol. 1. Interscience publishers New York, 1963.

[103] Charles Kittel, Paul McEuen, and Paul McEuen. *Introduction to solid state physics*. Vol. 8. Wiley New York, 2005.

[104] Desmond Tromans. "Elastic anisotropy of HCP metal crystals and polycrystals". In: *Int. J. Res. Rev. Appl. Sci* 6.4 (2011), pp. 462–483.

[105] Gregory V Samsonov. *Handbook of the Physicochemical Properties of the Elements*. Springer Science & Business Media, 2012.

[106] John J Adams et al. "Elastic constants of monocrystal iron from 3 to 500 K". In: *Journal of applied physics* 100.11 (2006), p. 113530.

[107] Pablo Alvarez et al. "Nanocrystalline Nd2Fe17 synthesized by high-energy ball milling: crystal structure, microstructure and magnetic properties". In: *Journal of Physics: Condensed Matter* 22.21 (2010), p. 216005.

[108] P Vedrine et al. "Mechanical characteristics of NdFeB magnets at low temperature". In: *Cryogenics* 31.1 (1991), pp. 51–53.

[109] Alexander Stukowski. "Visualization and analysis of atomistic simulation data with OVITO–the Open Visualization Tool". In: *Modelling and Simulation in Materials Science and Engineering* 18.1 (2009), p. 015012.

[110] S Alireza Etesami and Ebrahim Asadi. "Molecular dynamics for near melting temperatures simulations of metals using modified embedded-atom method". In: *Journal of Physics and Chemistry of Solids* 112 (2018), pp. 61–72.

[111] Charles Kittel, Paul McEuen, and Paul McEuen. *Introduction to solid state physics*. Vol. 8. Wiley New York, 2005, p. 51.

[112] MV Zheleznyi et al. "Structure and magnetic hysteresis Properties of NdFe11 Ti based alloys and their nitrides after different methods of obtaining". In: *Journal of Physics: Conference Series*. Vol. 1238. 1. IOP Publishing. 2019, p. 012006.

[113] Tim Mueller, Alberto Hernandez, and Chuhong Wang. "Machine learning for interatomic potential models". In: *The Journal of chemical physics* 152.5 (2020), p. 050902.

[114] Shyue Ping Ong et al. "Python Materials Genomics (pymatgen): A robust, open-source python library for materials analysis". In: *Computational Materials Science* 68 (2013), pp. 314–319.

[115] Ask Hjorth Larsen et al. "The atomic simulation environment—a Python library for working with atoms". In: *Journal of Physics: Condensed Matter* 29.27 (2017), p. 273002.

[116] Maciej Dabrowski et al. "Optically and microwave-induced magnetization precession in [Co/Pt]/NiFe exchange springs". In: *ACS Applied Materials & Interfaces* 12.46 (2020), pp. 52116–52124.

[117] YK Takahashi et al. "Size effect on the ordering of FePt granular films". In: *Journal of Applied Physics* 93.10 (2003), pp. 7166–7168.

[118] Kwanghyo Son et al. "Superior magnetic performance in FePt L10 nanomaterials". In: *Small* 15.34 (2019), p. 1902353.

[119] M Watanabe et al. "Microstructure and magnetic properties of FePt–Al–O granular thin films". In: *Applied Physics Letters* 76.26 (2000), pp. 3971–3973.

[120] Johann Fischbacher et al. "Micromagnetics of rare-earth efficient permanent magnets". In: *Journal of Physics D: Applied Physics* 51.19 (2018), p. 193002.

[121] Richard FL Evans et al. "Atomistic spin model simulations of magnetic nanomaterials". In: *Journal of Physics: Condensed Matter* 26.10 (2014), p. 103202.

[122] Jaesong Kim, Yangmo Koo, and Byeong-Joo Lee. "Modified embedded-atom method interatomic potential for the Fe–Pt alloy system". In: *Journal of materials research* 21.1 (2006), pp. 199–208.

[123] MI Baskes, JS Nelson, and AF Wright. "Semiempirical modified embedded-atom potentials for silicon and germanium". In: *Physical Review B* 40.9 (1989), p. 6085.

[124] Michael I Baskes. "Modified embedded-atom potentials for cubic materials and impurities". In: *Physical review B* 46.5 (1992), p. 2727.

[125] Murray S Daw, Stephen M Foiles, and Michael I Baskes. "The embedded-atom method: a review of theory and applications". In: *Materials Science Reports* 9.7-8 (1993), pp. 251–310.

[126] Jae-Song Kim et al. "The origin of (001) texture evolution in FePt thin films on amorphous substrates". In: *Journal of applied physics* 99.5 (2006), p. 053906.

[127] J-U Thiele et al. "Perpendicular magnetic anisotropy and magnetic domain structure in sputtered epitaxial FePt (001) L1 0 films". In: *Journal of applied physics* 84.10 (1998), pp. 5686–5692.

[128] C Sullivan and Alexander Kaszynski. "PyVista: 3D plotting and mesh analysis through a streamlined interface for the Visualization Toolkit (VTK)". In: *Journal of Open Source Software* 4.37 (2019), p. 1450.

[129] Bill Lorensen Will Schroeder Ken Martin. *The Visualization Toolkit (Edition 4.1)*. Kitware, 2018.

[130] Kitware. *VTK Delaunay Documentation reference*. URL: https://vtk.org/doc/nightly/html/classvtkDelaunay3D.html.